A Novel Continuous and Efficient Approach for In-Plane Thick-Muscle Wrapping on a Surface

Preface

List of publications

The present thesis was developed as a research associate at the Institute of Mechanics and Robotics ("Lehrstuhl für Mechanik und Robotik") at the University of Duisburg-Essen. Many of the contributions and concepts presented in this work have been previously published in the following conference publications and proceedings:

- **K. Müller** and A. Kecskemethy. Planar wrapping of "thick" muscle paths with non-constant cross section – comparison of analytical versus numerical methods. *89th Annual Meeting of the International Association of Applied Mathematics and Mechanics*, Munich, Germany, March 19-23, 2018.

- **K. Müller** and A. Kecskemethy. A continuous and computationally efficient method for wrapping a "thick" strand over a surface – The planar single-surface case. In *Proceedings of the Advances in Mechanism and Machine Science.* IFToMM WC 2019. Mechanisms and Machine Science, vol 73. Springer, Cham, 2019.

- **K. Müller** and A. Kecskemethy. A new approach for continuous wrapping of a thick strand on a surface – The planar case with constant length and free ends. In *Advances in Robot Kinematics 2020.* ARK 2020. Springer Proceedings in Advanced Robotics, vol 15. Springer, Cham, 2021.

- **K. Müller** and A. Kecskemethy. Planar wrapping and stretching of a thick strand on a surface by continuous integration. *ECCOMAS Thematic Conference on Multibody Dynamics*, Budapest, Hungary, December 12-15, 2021. *(in press)*

Acknowledgments

Without some people who accompanied me on this exciting, scientific journey, its completion would not have been possible.

First and foremost, I would like to thank Prof. Andrés Kecskeméthy for giving me the opportunity in the first place and entrusting me with this challenging topic, as well as for his patience, the many constructive conversations in which vast amounts of yellow sheets were covered with formulas, and especially for having accompanied me all the

IV

way to the end. It was an enriching time that has left its mark on me and that I will never forget.

I would also like to thank Prof. Vincenzo Parenti-Castelli, who agreed to review my thesis after I presented at the IFToMM World Congress 2019 and still kept his word two years later, and Prof. Bettar Ould el Moctar, who spontaneously volunteered to be the third examiner. Many thanks for the interest, careful consideration of my work, and valuable comments.

It has been a great pleasure to have been surrounded by such wonderful colleagues throughout my time at the university. Each of them has contributed to making this time a unique journey; in addition to professional discourse, friendships have grown that I am convinced will outlast these days. I would like to express a special thanks to Alina Stepken and Mehdi Ghiassi for their valuable and precise proofreading advice.

Finally, I would like to thank my partner and family, from who I have always received unconditional support.

Danksagung

Ohne einige Menschen, die mich auf dieser spannenden, wissenschaftlichen Reise begleitet haben, wäre ihre Fertigstellung nicht möglich gewesen.

Zuallererst möchte ich mich daher bei Prof. Andrés Kecskeméthy bedanken, dafür, dass er mir überhaupt die Gelegenheit bot und mir dieses herausfordernde Thema anvertraute, sowie für seine Geduld, die vielen konstruktiven Gespräche, bei denen Unmengen an gelben Blättern beschrieben wurden, und ganz besonders dafür, diesen Weg bis zum Ende mit mir gegangen zu sein. Es war eine lehrreiche Zeit, die mich geprägt hat und die ich nie vergessen werde.

Außerdem gilt mein Dank Prof. Vincenzo Parenti-Castelli, der sich nach meinem Vortrag beim IFToMM World Congress 2019 bereiterklärte, meine Arbeit zu begutachten, und auch zwei Jahre später noch zu seinem Wort stand, sowie Prof. Bettar Ould el Moctar, der sich spontan als dritter Gutachter zur Verfügung stellte. Herzlichen Dank für das Interesse, die sorgfältige Auseinandersetzung mit meiner Arbeit und die wertvollen Anmerkungen.

Es war mir eine große Freude, während meiner gesamten Lehrstuhlzeit von so wunderbaren Kollegen umgeben gewesen zu sein. Jeder von ihnen hat dazu beigetragen,

Kurzfassung

Im Rahmen der biomechanischen Forschung spielt die Simulation des menschlichen Bewegungsapparates eine zentrale Rolle für das Verständnis der menschlichen Bewegung oder der Belastungen bei spezifischen Tätigkeiten. Wichtig ist hierfür die korrekte Darstellung der Muskeln, wobei eine Balance zwischen hoher Genauigkeit und Recheneffizienz gefunden werden muss. Ein gängiger Ansatz ist daher das Darstellen der Muskeln als dünne, masselose Linien und die Festlegung ihres Pfades durch das Wickeln über definierte Flächen. In Fällen, in denen die Muskeldicke nicht zu vernachlässigen ist und während der Kontraktion sogar noch variiert, geraten diese Methoden an ihre Grenzen, da ein aufwändiges Platzieren und Verschieben der Wickeloberflächen notwendig wird.

Hier setzt diese Arbeit an: Ziel ist, eine neue, kontinuierliche Methode zu entwickeln, um dicke, konvexe Muskeln, deren Radius entlang ihrer Mittellinie definiert ist, reibungsfrei über glatte und konvexe Oberflächen zu legen und dabei die Lage der Mittellinie automatisch zu bestimmen. Die Endpunkte des Muskels sollen dabei frei beweglich sein und Dehnung sowie damit verbundene Querkontraktion des Muskels und Änderung seiner äußeren Erscheinungsform ebenfalls berücksichtigt werden.

Ausgehend von einer Diskretisierung des dicken Muskels als Perlenschnur wird die kontinuierliche Berechnung der gewickelten Mittellinie als Grenzwert für eine unendliche Anzahl von Perlen abgeleitet. Zunächst ohne Längsdehnung wird das Verschieben des Muskels entlang der Oberfläche untersucht und die Geschwindigkeitsübertragung von einem zum anderen Ende hergeleitet. Anschließend werden die Bedingung der konstanten Länge aufgehoben und die Auswirkungen der Längsdehnung und Querkontraktion mit Hilfe der Störungsrechnung untersucht, wobei eins der freien Muskelenden vorerst fixiert wird. Die Kombination dieser Ansätze ermöglicht schließlich das gewünschte Wickeln, Verschieben und Dehnen eines dicken Muskels auf einer glatten Oberfläche. So entsteht ein aus zwei verschachtelten Integrationen bestehender Algorithmus: Die äußere bezieht sich auf die Erfüllung der Bindungsgleichungen an den Übergängen vom gewickelten Segment zu den unverformten freien Enden; die innere sorgt für die dafür benötigten, entlang des gewickelten Segments übertragenen Größen, nämlich der Länge der Mittellinie, der Geschwindigkeitsübertragung und des Einflusses der Dehnung.

Die Methode wird im Vergleich zu einer Perlenketten-Diskretisierung sowie zu Iterationen auf Positionsebene validiert. Dabei erweist sie sich als äußerst recheneffizient und genau. Zuletzt wird das Verfahren erfolgreich auf den musculus deltoideus als biomechanisches Beispiel des in die Frontalebene projizierten Schultergelenks angewendet.

Abstract

In the context of biomechanical research, the simulation of the human musculoskeletal system plays a central role in understanding human motion or physical stress during specific movements. The correct representation of the muscles is important in this context, whereby a balance between high accuracy and computational efficiency has to be found. A common approach within muscle-actuated simulations is, therefore, to model the muscles as thin, massless lines and define their path by wrapping them over defined obstacle surfaces. These methods reach their limits in cases where the muscle thickness is not negligible and may even vary during contraction. Here, a laborious placement and displacement of the wrapping surfaces becomes necessary.

This problem is addressed in this thesis: The objective is to develop a novel, continuous approach for placing thick, convex muscles, with the radius defined along their centerline, frictionlessly over smooth and convex surfaces and having the location of the centerline automatically determined. The endpoints of the muscle are supposed to move freely and stretching as well as associated lateral contraction of the muscle and change in its outer appearance are also to be taken into account.

For this purpose, starting from a discretization of the thick muscle as a string of spherical beads, the continuous computation of the position of the wrapped centerline is derived as limit for an infinite number of beads. Not considering the elongation at first, the muscle sliding along a surface is regarded and the velocity transmission from one end to the other is derived. Then the condition of constant centerline length is omitted and the effects of longitudinal elongation and lateral contraction of the muscle are examined using perturbation theory, with one of the muscle's free ends initially held fixed. The combination of these approaches through superposition finally allows the desired wrapping, sliding and stretching of a thick muscle on a smooth surface. This leads to an algorithm consisting of two nested integrations: The outer integration concerns the satisfaction of the constraint equations at the segment transitions between wrapped segment and undeformed free end straight line segments, while the inner integration provides the required quantities along the wrapped segment, i.e., the centerline length, the velocity transmission, and the influence of strain.

The method is validated against an implementation of a bead chain discretization as well as position-level iterations. It proves to be highly efficient in terms of computation with high accuracy. Finally, it is successfully applied to the musculus deltoideus in the biomechanical example of a shoulder joint projected onto the coronal plane.

Contents

1 Introduction

1.1 Motivation

Modeling strands like muscles or ligaments is required in many biomechanical applications that deal with the analysis of the human musculoskeletal system in order to deepen the understanding of movement and physical loads during certain activities. In relation to the task at hand, it is necessary to weigh up between high accuracy and complexity combined with high modeling and computing effort on one side and a highly reduced model with the shortest possible computation time at the expense of accuracy on the other side. In musculoskeletal simulations, it is commonly necessary to calculate the muscle forces or the joint loads. Here, the muscle models involved usually require the length of the muscle as well as the change in length as input variables, and a key issue is to determine them quickly and reliably. Thus, it is standard practice to model muscles as thin massless lines, where the exact placement of these lines in the moving system poses a problem and is usually only solved approximately defining their path using via points (as the simplest variant) or – more advanced – by wrapping them over specifically defined obstacle-surfaces to obtain smooth muscle paths. Careful placement of the wrapping obstacles is necessary to guide them close to the actual centerline of the anatomical muscle where the line of action of the muscle forces is assumed to be. This becomes even more difficult if the shape of the muscle changes during the movement. Furthermore, the muscle diameter may be non-negligible and may be combined, in particular, with a non-constant cross-section thickness, as exemplarily demonstrated in Fig. 1.1 for the musculus deltoideus, which is located between clavicula and humerus wrapping over the shoulder joint and which is responsible for the abduction of the upper arm.
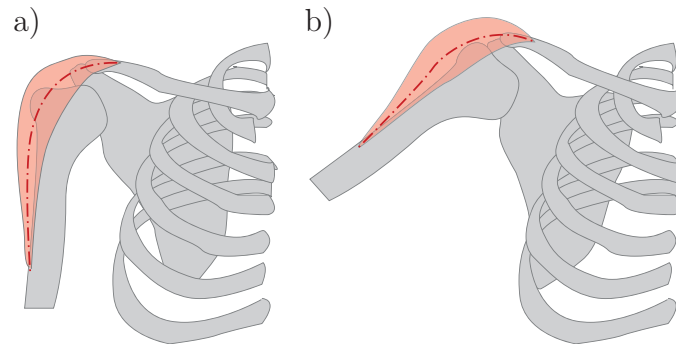
Figure 1.1: Example: Musculus deltoideus pars acromialis for abduction

Discrete methods, modeling the strand, for example, as a chain of spherical beads, provide a general and powerful workaround having the advantage of a fast derivation. The disadvantage is, however, that their implementation is mostly complex, involving multiple contact detection and bookkeeping about it, which in turn can be associated with very high computation times. Also, in musculoskeletal simulation models, discrete approaches may lead to jerky, unrealistic forces and moment arms due to their discontinuity when coupled to dynamic muscle models, which affect the resulting body and joint loads.

1.2   State of the art

Taken literally, the term "biomechanics" designates "the study of the structure and function of biological systems by means of the methods of mechanics."[26, p. 189] Two main objectives are pursued here: On the one hand, the modeling of a given physiological system is one of the best ways to understand it [88, p. 403]. On the other hand, computer modeling and simulation allow to estimate quantities like muscle forces or joint loads where in vivo measurements are painful or impossible [75, p. 1948].

According to the areas of activities, the field of biomechanics may be subdivided into orthopedic biomechanics, sports biomechanics, forensic biomechanics, human factors, ergonomics etc. However, they all have in common that, pursuant to the definition, mechanical knowledge is used and applied to biological systems to study specific issues, such as gait and motion analysis, the connection between mechanical stress and orthopedic disorders, rehabilitation after injuries, the design of workplaces, or analysis and optimization of athletic movement techniques [65, p. 1].

In most of these fields focusing on humans or animals, modeling and simulation of the musculoskeletal system are fundamental. It is composed of a passive and an active part. The passive part is also called the skeletal system and consists of the bones, ligaments and joints. Hereby, bones and ligaments are load-transmitting elements and responsible for the statics of the musculoskeletal system. Joints are special arrangements of bones and ligaments that allow certain movements. [65, p. 2][71, p. 54-59]

The active part of the musculoskeletal system is the so-called muscular system containing around 220 separate, striated skeletal muscles [71, p. 54]. They are connected to the bones through tendons and can actively change their length and thereby exert forces on the passive musculoskeletal system. In doing so, they produce not only move-

ment but are also able to maintain posture (postural muscles) and ensure the statics of the entire body. Since muscles can only actively shorten but can not lengthen, each joint requires more than one muscle to enable possible movements. This means that the active muscle does not only move the joint but it does also lengthen the muscle, which is responsible for the counter-movement. [65, p. 3][71, p. 54-59]

Thus, the muscles play a central role in moving the musculoskeletal system, and for modeling and simulating such a system, adequate modeling of the muscles is essential. The relationship between the shortening of a muscle and the resulting muscle force that is actually applied to the joints and creating the movement is defined in so-called muscle models.

1.2.1 Muscle models

There exists a variety of muscle models, ranging from simple torque generators to complex high-order nonlinear systems like the one presented by Hatze[28] in 1978 depending on more than 50 parameters to describe the motion of a single joint[88, p. 404]. In [88], Winters and Stark distinguish three types of muscle models:

- The first one is a simple second-order differential equation, which treats the muscle as a "black box"[88, p. 404] and tries to reproduce the input-output-relation by setting model parameters according to the task and the movement operating range.
- Muscle models of the second category are based on the muscle model introduced by A. V. Hill[32, 34] and thereby include a macroscopic view on the muscle.
- The third type of muscle models is based on the muscle model of Huxley[38], which gives an even more detailed, microscopic view of the muscle.

Most of the muscle models use the muscle length and the length change as input parameters. So do the models of Hill and Huxley, which are most commonly used.

Based on his earlier works [30, 31] on the relationship between the energy developed in an excited muscle and the shortening of the muscle where Hill already found out, that the relation between the force and the speed of shortening is an intrinsic property of the muscle itself without depending on interventions of the nervous system [23], Hill succeeds 1938 in giving the state equation for the speed of shortening under a constant

load (tension) F as

$$(F + a)(v + b) = (F_0 + a)b \qquad (1.1)$$

where v is the velocity of contraction, a is the coefficient of heat per muscle elongation, F_0 is the maximum isometric tension (or load) generated in the muscle, and $b \approx a\frac{v_0}{F_0}$ is a muscle constant [29].

Recapitulated, Hill's muscle model consists of three elements: the contractile element (CE) containing force-length and force-velocity relations, as well as two elastic elements – one in series (SEE) and one in parallel (PE) – like it is illustrated in Fig. 1.2. Inputs for the contractile element are the neural muscle stimulation or activation of the muscle, the muscle length and the contraction velocity. A one-dimensional force is the output. Additionally the constant, muscle-specific parameters have to be supplied. [42, 33, 91, 25, 24, 72]
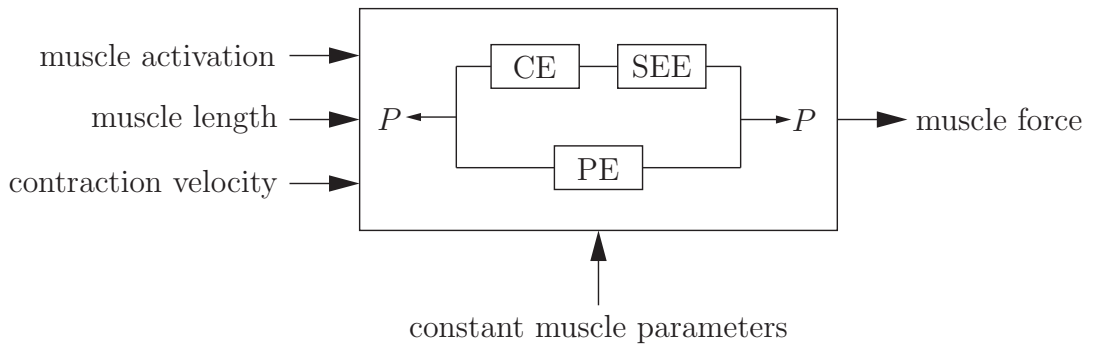
Figure 1.2: Hill-type muscle model (combined from [91, p. 367] and [69, p. 13])

Today, Hill's muscle model has become established and is still broadly used [25, 19, 72, 50, 48, 54, 24, 58, 83] due to its excellent tradeoff between high accuracy and low computational costs [88] as well as easy implementation[86]. Sometimes, it is slightly modified or extended, for example, by also considering history effects, recruitment patterns or high frequency oscillation damping[25, p. 1][27].

The Huxley-type muscle model is based on the "sliding filament theory", explaining the muscle contraction by muscle proteins that slide past each other generating movement and thereby connecting biochemistry to mechanics. This theory was discovered independently by two different research groups: Andrew F. Huxley and Rolf Niedergerke from the University of Cambridge [39] and Hugh Huxley and Jean Hanson from the Massachusetts Institute of Technology [40]. In [38], A. F. Huxley presented a mathematical model to describe the muscle's behavior on a microscopic level, which is able

to describe phenomena where Hill's model comes too short[88, p. 405][86]. Here, the chemical interactions between actin and myosin (motor proteins within the muscle), which are responsible for the muscle's contraction are considered in order to predict the mechanics and energetics of a muscle [86, p. 4827][90, p. 91]. T. L. Hill and his colleagues [35, 36] as well as Wood and Mann [89] also published valuable contributions to this topic. The mathematical description of the sliding filament theory results in a set of coupled first-order differential equations[90, p. 91][36, p. 285 f.].

Zahalak [90] presented a rational mathematical procedure, which is a compromise between the Huxley-based mechanistic models and the Hill-based phenomenological models [88, p. 406] and which, therefore, enabled numerical simulation due to being less complex [42, p. 59].

All of these models have in common that they have to be provided with muscle-specific parameters like the shortening heat, the increase of energy or the isometric tension in the case of Hill's muscle model as well as with quantities depending on the movement like the muscle's actual length and the length change.

The required muscle data is generated in two different ways: By the dissection of cadaver specimen, muscle volume, fiber length and physiologic cross-sectional areas can be detected [1, 8]. In this procedure, however, it is not possible to measure the muscle in vivo while performing various movements. This can be achieved though by using magnetic resonance imaging (MRI). In [84], for example, the position of the muscles' centerlines is measured via MRI for different configurations. In [37], MRI data is used to measure muscle volume and to identify muscle structures. The boundaries of the muscle are manually outlined and used to create three-dimensional polygonal surfaces. On the basis of these models, volume and length of each muscle of the upper limb were measured. Another aim in using MRI data can be the development of a 3D finite element model as it is done by Calvo et al. in [9] for the tibialis anterior of a rat.

FEM muscle models

Using the finite element method (FEM) or the finite volume method (FVM) is the most accurate and detailed way to model the geometry of the anatomical muscle. Here, the muscle is treated as a viscoelastic solid, and these methods are widely used in order to obtain highly accurate three-dimensional muscle models, which are also able to reproduce 3D deformations [82, 76, 66]. Through the combination with three-dimensional FEM or FVM models, it is possible to extend Hill's originally one-dimensional muscle

model to a 3D Hill-type muscle model [46, 41, 7, 52]. The high resolution of FEM and FVM models involves however a high complexity that causes difficult modeling and long computing times. Especially due to the high computational intensity, FEM and FVM models are used in simulations only for selected single muscles [82, p. 73]. In the field of computer graphics, where a realistic appearance is most important, the use of FEM/FVM models is very common. For simulations of movements where multiple muscles are involved like they are used for gait analysis, for example, they are highly unsuitable. Besides, FEM discretizations do not directly represent the fiber-like properties of muscles. These have to be implemented by additional functions [7].

Muscle models in computer graphics

However, muscles are not only modeled within biomechanical applications. Researchers in the field of computer graphics are also engaged in this subject, focusing on the external appearance in order to create realistic animations of living creatures. In [68], Scheepers et al. identify three anatomical structures having an influence on the surface form: the skeleton, the panniculus adiposus (or fat layer) and the musculature. So, visually realistic modeling of the musculature is one aspect to obtain natural-looking 3D character animations. This can be achieved by using deformed cylinders as muscle models, as applied by Wilhelms and Van Gelder[87] to build a complete model of a monkey. The muscles are deformed passively as the result of the joint motions with the objective to maintain the muscle volume approximately constant. Here, the focus lies on visual realism of the muscles instead of precision and calculation of the joint loads during certain movements. In [68], for example, points that define the muscles are adjusted visually to create the desired deformation. Pai[60] introduces a dynamic strand model based on Cosserat rods[3, 67] to model thin deformable objects and uses it to simulate strands of surgical sutures. These spline-based strand models can also be applied to represent tendons, muscles or the individual fascicles of each muscle, which is done, for example, to build forearm and hand models[61, 62, 80, 81]. In first attempts, the muscle is hereby modeled with its centerline being the axis of the Cosserat rod. Then it is improved by modeling it as a generalized cylinder with a cubic B-spline curve as centerline. The cross-sectional area is variable and scaled during the motion to take volume preservation into account. This is exemplarily applied to modeling a hand consisting of bones, joints and muscles. For a predefined movement, the deformations of the skin surface caused by the underlying muscles and tendons can then be realistically represented[80]. So, although thick muscles are indeed considered

here, the primary concern is to reproduce their outer contour as realistically as possible and not to provide the values needed in the muscle models to calculate muscle forces or joint loads.

Muscle models in musculoskeletal simulations

In multibody simulations, where the musculoskeletal system contains a large number of muscles, muscles are usually reduced to muscle paths modeled as thin massless lines that transmit the muscle forces and that are defined between origin and insertion. Origin and insertion is the medical term for the points where the muscle is attached to the skeletal structure. The simplest, fastest, but also the coarsest method is to model the muscle path as a straight line between origin and insertion[2, 58, 57, 47, 74]. In sensitivity analysis, however, it was found out that small changes in the moment arm with which the muscle force is applied to the joint[64, p. 1249f.][59] or in the parameters of muscle geometry[17, p. 671] have a large effect on the calculated muscle forces and joint loads[18, p. 1931]. This is the source of the effort to define the muscle paths as precisely as possible and ideally locate them along the midline of the anatomical muscle while keeping an eye on the computation time. The methods used to achieve this are diverse and have been constantly developed further. First improvements were made defining so-called via points through which the muscle path must pass and which are attached to the bone structure. Here, the muscle path consists of straight-line segments between the via points[15, 73, 56, 55]. Due to kinks at the via points and the fact that the number of via points can vary during the movement[15], nonsmooth curves are obtained for the muscle path, which can lead to undesired jumps when calculating the muscle forces.

An alternative to defining the bent muscle path by via points is to wrap it over the path constraining geometries. Here, two different types of wrapping approaches can be distinguished: First are the ones where the wrapping geometry is given as a surface discretization, for example, in the form of bone meshes[18] or slices[21]. These have the advantage that it is possible to wrap them over complex bone geometries, and that they are computationally efficient[69]. However, the disadvantage here is that the wrapping over surface edges causes a nonsmooth rate of length change of the muscle path and the associated discontinuities in the calculated muscle force[69]. In 2017, Zarifi and Stavness[92] present a new approach to the general wrapping methods that allows for wrapping the thin-line approximated muscle directly on bone geometries given by arbitrary meshes. Lloyd et al.[49] resume to this approach by proposing a

robust and fast method for wrapping thin, massless muscles frictionlessly on arbitrary surface meshes by discretizing the muscle into small straight-line segments. For the second kind of wrapping approach, smooth surfaces are used. In 1994, van der Helm [85] is one of the first to fit simple geometries like spheres, cylinders or ellipsoids into the bone geometry and to wrap the muscle path around them. As a restriction, origin, insertion and the center of the wrapping geometry have to lie in one plane[11, p. 1210]. Six years later, Garner and Pandy[22] present the idea of the so-called obstacle-set method. They assume that the muscle force acts along the centerline of the muscle, which can be idealized as an elastic band that moves frictionlessly over neighboring anatomical structures that constrain the muscle path. To model these constraints, they introduce the use of simple rigid bodies like spheres and cylinders on which the curved part of the muscle path is wrapped. The whole muscle path is represented by a series of straight line and curved line segments that are connected by via points. There exist two types of via points: those that are fixed on the bone reference frame, and those that are fixed on the wrapping geometries. Kinks at the transition of a straight-line to a curved-line segment are possible. Audenaert and Audenaert[4] and Marsden et al.[51] consider the whole muscle path between origin and insertion and look for the globally shortest muscle path, using geodesic wrapping on the smooth wrapping surfaces, which are again spheres and cylinders. Here, the curved-line and the adjacent straight-line segments are connected smoothly. The solution to this problem is found as the result of an optimization problem. In 2016, Scholz et al.[70] present an analytical solution to this problem that uses natural geodesic variations to formulate an explicit path-error Jacobian, which makes the algorithm computationally very efficient. The presented muscle wrapping approach is formulated independently of the surface representation that can be explicit or implicit and allows the use of complex wrapping surfaces that match the anatomical structures more accurately than spheres and cylinders.

Thus, muscle wrapping has become standard in the context of creating musculoskeletal simulations, as evidenced by the fact that it is already implemented in popular simulation software such as SIMM (Software for Interactive Musculoskeletal Modeling)[14], OpenSim[13] and Anybody Modeling System[12] for simple wrapping geometries. While these wrapping algorithms are already very sophisticated, they still face the challenge of placing the wrapping surfaces correctly. When the obstacle geometries are fitted to the bone geometries, the resulting wrapped path corresponds to the line of contact rather than the centerline of the muscle. However, the latter is generally assumed to be the line of action of the muscle force. If one wants the wrapped path to be closer to the anatomical midline of the muscle, the wrapping surface must be lifted accordingly.

However, during the movement the problem might arise that the wrapping surfaces need to be displaced continuously to approximate the centroid line of the muscle when the shape of the anatomical muscle changes due to contraction. This is not possible by this approach.

To overcome these difficulties, a discrete approach to wrap thick strands was introduced in [20]: Franci and Parenti-Castelli present an elastic fiber model where the volume of the fiber is represented by a chain of contacting spheres or "beads". The accompanying fiber contact model allows the detection of contact between the fiber and the body surface as well as the contact of the fibers with each other. The model is exemplarily used to model a ligament in the ankle joint, but the basic idea of representing a volumetric fiber by a chain of spheres can be applied to generic situations. A muscle modeled as a bead chain can be directly wrapped over the bone geometry while its centerline is automatically lifted to its approximated position. While this approach is very general and powerful, it has the disadvantage of being computationally expensive due to the extensive contact detections and record-keeping about it. Furthermore, it is discontinuous as a result of the discretization. Especially the last point becomes a serious disadvantage when the method is applied for modeling muscles to compute the resulting muscle forces. This was the starting point of this thesis.

1.3 Objective and basic assumptions

The aim of this thesis is to develop a novel, continuous and computationally efficient method to wrap and slide muscles with variable thickness over smooth surfaces. The thickness of the muscle is thereby described mathematically along its centerline, and wrapping of this thick muscle over the surface leads to a centerline muscle path that is automatically computed according to the local thickness and the surface curvature. To this end, smooth differential equations are derived as the limit of infinitesimally close beads. Due to the complex differential geometric relationships involved in the derivation, the approach is presented here for the planar case. The spatial case can be derived based on these models in later work.

The approach is based on the assumptions that

(1) muscle strands are perfectly slack (thus, no bending moments occur),
(2) the cross-sections remain planar and undeformed after flexion,
(3) there are no friction effects between muscle and surface,

(4) the variation of the muscle's cross-section is convex, and

(5) the arbitrary wrapping surface is also smooth and convex.

In addition, in Chapter **3** and Chapter **4**, the muscle's centerline is assumed to be constant. In the last two chapters (Chapter **5** and Chapter **6**) this constant length condition is finally omitted to cover elongation with compressible cross-sections.

1.4   Overview

The work is organized as follows: In Chapter **2**, some mathematical fundamentals from differential geometry as well as perturbation theory are briefly introduced, which will be referred to in the later chapters of the method derivation.

Chapter **3** defines mathematically what is meant by a "thick muscle" in the context of this thesis, and a bead chain, inscribed into the muscle's contour, is introduced as a discrete approximation. From this, the continuous approach for a thick, conical muscle segment wrapping over a given arc length of a convex surface is derived as the limit of infinitesimally close beads at position level. Subsequently, the velocity transmission (from one endpoint of the wrapped muscle segment in contact with the surface to the other) is also deduced first from bead to bead and then continuously for an infinite number of beads. The length of the muscle's centerline is assumed to be constant.

In Chapter **4**, the condition that the centerline length is constant is still valid and the approach is extended for the case of varying muscle thickness (non-constant conicity) and free muscle ends that are not in contact with the surface and can perform prescribed motions. Here, two different effects can occur in the area of the wrapped muscle segment: The first is pure wrapping or unwrapping at the transition to the free end segments, the second is a displacement of the muscle in the contact area. The terms "wrap" and "pull" are introduced to distinguish these components. Constraint equations in the longitudinal and transverse directions are formulated on velocity level for the two transitions from the wrapped segment to the free end segments. Finally, the continuous method is validated by comparison with a bead chain discretization of the muscle strand.

In Chapter **5**, the constant-length condition is omitted, and the method is extended to cover elongation with compressible cross-sections. Starting from the simplest case of a cone-shaped muscle on a circular surface, the method is generalized to the case of a convexly curved muscle on a convex surface.

In Chapter **6**, the approaches developed in Chapter **4** and Chapter **5** are combined with the goal of enabling stretching and sliding of a thick muscle with two free ends. Again, the derivation is first presented for the case of a cone-shaped muscle wrapping over a circle and is generalized from there. Hereby, the changes resulting from displacement and those associated with stretch are considered separately and transferred from one end of the muscle to the other.

Chapter **7** concludes this thesis by briefly summarizing and discussing the major findings achieved by this work. This also includes an outline for possible future directions.

2 Mathematical Foundations

2.1 Differential geometry

In this chapter a brief insight into fundamental differential geometric properties of curves is given, which provides a basis for Chapter **3**. The focus lies on planar curves, and it is based on the literature on differential geometry of Strubecker [77, 78], Struik [79], Klingenberg [44, 45], do Carmo [10], Pressley [63] and Bär [5].

2.1.1 Parametric description of curves

A parametrized curve c in $\mathbb{R}^n$ is an indefinitely often differentiable map $c : I \mapsto \mathbb{R}^n$ and $c(I)$ is called the image of the curve. The interval $I \subseteq \mathbb{R}$ is the parameter domain and the elements u of I are called parameters. The curve c is said to be regular if $d\,c(u)/du \neq 0$ for all u. [45, p. 8]

Another approach to define a spacial curve is to interpret it as the path of a point in motion [79, p. 1][63, p. 2]. The rectangular coordinates (x, y, z) of the point can be expressed as functions of a parameter u inside a certain interval $I \subset \mathbb{R}$

$$x = x(u), \quad y = y(u), \quad z = z(u) \tag{2.1}$$

with $u \in I$.

Often u is thought of as time, but this is not necessary, because the parametrization of a given curve is not unique. For example, the parametrization $c(u)$ of a parabola given as the level curve $y = x^2$ has to satisfy $c_2(u) = \{c_1(u)\}^2$ and could, for instance, be $c(u) = (u, u^2)$, but it also could be $c(u) = (u^2, u^4)$ or infinitely many others [63, p. 2 f.]. Equivalent parametrizations of a curve can be transformed into each other by parameter transformation [45, p. 8]. The change of variables can be performed by a substitution $u = f(v)$ without changing the curve itself [79, p. 1].

2.1.2 Arc length

One parametrization, which stands out against the others, is the parametrization by arc length. The arc length is the length of a curve, and for a curve c starting at a point

$c(u_0)$ it can be computed by the function $s(u)$ given by

$$s(u) = \int_{u_0}^{u} \left\| \frac{d\,c(\bar{u})}{d\bar{u}} \right\| d\bar{u} \quad . \tag{2.2}$$

A curve is said to be parametrized by arc length if $\|d\,c(u)/du\| = 1$ [45, p. 9].

According to the approach of considering $c(u)$ as the path of a moving point, $\|d\,c(u)/du\|$ is the speed of the point, which is the same as the rate of change of distance along the curve [63, p. 11]. Hence, one can speak of a curve that is parametrized by arc length as a unit-speed curve, because $d\,c(u)/du$ is a unit vector for all $u \in I$.

2.1.3 Tangent, normal and curvature

The first derivative of a parametrized curve is also called the tangent vector

$$\underline{t}(s) = \frac{d\,c(s)}{ds} = c'(s) \quad , \qquad \text{with } (\ldots)' = \frac{d}{ds} \quad , \tag{2.3}$$

of c at the point $c(s)$. When $c(s)$ is a unit-speed curve $\underline{t}(s)$ is a unit vector.

Plane curves

As shown in Fig. 2.1, for a plane curve the normal field can be easily defined by rotating the tangent vectors counterclockwise by $\pi/2$ as

$$\underline{n}(s) := \begin{bmatrix} 0 & -1 \\ 1 & 0 \end{bmatrix} \underline{t}(s) \quad . \tag{2.4}$$

Because the curve is unit-speed, it holds

$$\underline{t}(s) \cdot \underline{t}(s) = 1 \quad . \tag{2.5}$$
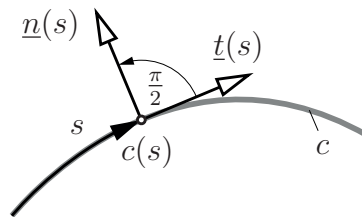
Figure 2.1: Tangent and normal to curve c (modified according to [5, p. 40])

Differentiation of this equation with respect to s yields

$$\Leftrightarrow 2\underline{t}'(s) \cdot \underline{t}(s) = 0 \quad , \tag{2.6}$$

which implies that the tangent $\underline{t}$ and $\underline{t}'$ are orthogonal to each other. Consequently, $\underline{t}'(s)$ is a multiple of $\underline{n}(s)$,

$$\underline{t}'(s) = \chi_s(s)\,\underline{n}(s) \quad . \tag{2.7}$$

The function $\chi_s : I \mapsto \mathbb{R}$ is called signed curvature of c. The signed curvature is a measurement, which indicates the divergence of the curve from a straight line ($\chi_s = 0$) [5, p. 41]. In other words, it can be interpreted as the rate at which the tangent vector rotates [63, p. 38]. For $\chi_s < 0$ the tangent rotates clockwise for a curve that is curved to the right, for $\chi_s > 0$ the tangent rotates counterclockwise and the curve is curved to the left (see Fig. 2.2).

A curve with a constant curvature $\chi_s = \text{const} \neq 0$ is a circle with the radius $r = \frac{1}{\|\chi_s\|}$.

Space curves

A requirement to define the signed curvature of planar curves is the definition of the normal described above. For the spatial case, the normal field cannot be defined as easily because there exists an infinite number of vectors, which are orthogonal to the
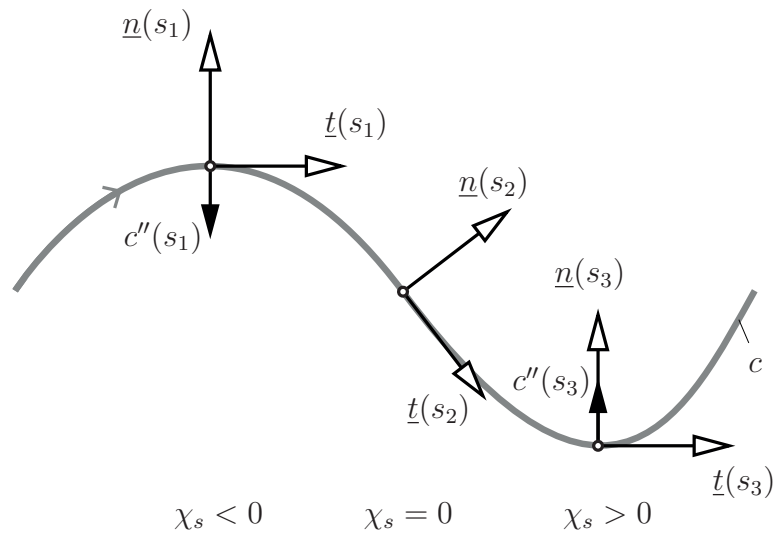
Figure 2.2: Changing curvature χ_s along the curve c (modified according to [5, p. 41][63, p. 35][45, p. 16])

curve's tangent. Here, one has to renounce the sign and compute the curvature χ by

$$\chi(s) := \|c''(s)\| . \tag{2.8}$$

For a three-dimensional curve one also speaks of the so called Frenet-Serret frame, which consists of the three orthonormal unit-vectors: the tangent vector $\underline{t}$, the normal vector $\underline{n}$ and the binormal vector $\underline{b}$ [63, p. 46 ff.][5, p. 65 ff.], that can be computed by

$$\underline{t} := c' \ , \tag{2.9}$$

$$\underline{n} := \frac{1}{\chi}\underline{t}' \quad , \text{ with } \quad \chi = \|\underline{t}'\| \quad , \text{ and} \tag{2.10}$$

$$\underline{b} := \underline{t} \times \underline{n} \ . \tag{2.11}$$

Since this work is restricted to planar curves, the spatial relationships are given here only for completeness and to deepen the understanding.

2.1.4 Osculating circle and evolute

The reciprocal of the curvature is called curvature radius

$$\rho(s) = \frac{1}{\|\chi\|} \quad . \tag{2.12}$$

It is the radius of the circle, which is the closest quadratic approximation to the curve, termed the osculating circle. It is defined as "the circle passing through three consecutive points of the curve"[79, p. 14] and illustrated in Fig. 2.3. The center of the osculating circle $M(s)$ is also called the center of curvature and lies on a straight line in the direction of the normal $\underline{n}(s)$ through the contact point $c(s)$.

The set of all centers of curvature of a curve c is called the evolute of c [5, p. 64] [77, p. 64]. Initially the evolute of a curve was described by Christaan Huygens as the envelope of the curve's normals, meaning that the tangents of the evolute are identical to the normals of the curve [77, p. 65]. Fig. 2.4 illustrates the evolute (red) of an ellipsoidal curve (gray) with four exemplary points $c(s_i)$ on the curve and the corresponding centers of the osculating circle $M(s_i)$ on the evolute. The connection of the center of curvature $M(s_i)$ and the related point $c(s_i)$ on the curve, illustrated for $i = 1, 2, 3, 4$, is tangential to the evolute and normal to the curve, having the length $\rho(s_i)$, which corresponds to the curvature radius. For s_1, also the osculating circle with radius $\rho(s_1)$ is pictured.

Struik sums it up and formulates a relationship between the arc length of the evolute and the difference of the radii of curvature, which is used in Chapter **3**: "The tangent of the locus of [c] of the centers of the osculating circles of a plane curve has the direction of the principal normal of the curve; its arc length between two of its points is equal to the difference of the radii of curvature of the curve at these points." [79, p. 42]
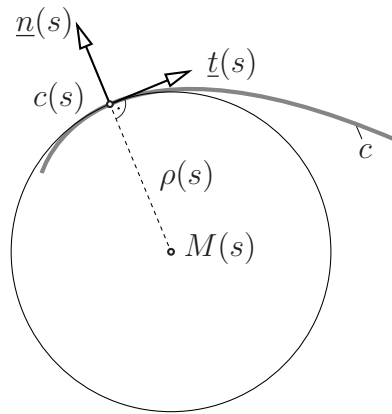
Figure 2.3: Osculating circle
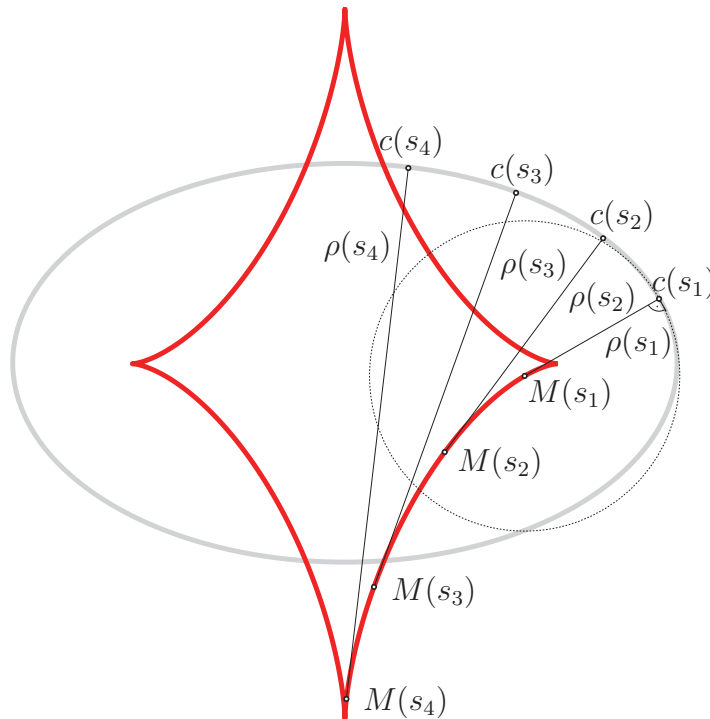
Figure 2.4: Evolute of an ellipse with osculating circle at s_1

2.2 Perturbation theory

Preliminarily to Chapter **5**, a brief introduction to first-order perturbation theory is given here based on the literature of Bellmann [6] and Kato [43]. Perturbation theory is an approach to solve a physical problem where the exact solution is not known and it is based on a series expansion. The main idea is to decompose the problem into a solvable and a perturbative part, approximating the exact solution y by the perturbative expansion

$$y = y_0 + \epsilon^1\, y_1 + \epsilon^2\, y_2 + ... \tag{2.13}$$

with y_0 being the unperturbed solution and $y_1, y_2, ...$ representing the first-order, second-order, ... perturbative corrections for $0 < \epsilon \ll 1$. Thus,

$$y \approx y_0 + \epsilon^1\, y_1 \tag{2.14}$$

is called first-order perturbative solution and obtained by truncating the higher-order terms.

Hence, given a first-order differential equation

$$\dot{y} = f(t, y, \epsilon) \quad , \tag{2.15}$$

the first-order perturbative approximation

$$y(t) = y_0(t) + \epsilon\, y_1(t) \tag{2.16}$$

is inserted into Eq. (2.15), leading to

$$
\begin{aligned}
\dot{y}_0 + \epsilon\, \dot{y}_1 &= f(t, y_0 + \epsilon\, y_1, \epsilon) \\
&= f_0(t, y_0) + \epsilon\, \left.\frac{\partial f}{\partial y}\right|_{\epsilon=\text{const}} y_1 + \epsilon\, \left.\frac{\partial f}{\partial \epsilon}\right|_{y=\text{const}} \quad .
\end{aligned} \tag{2.17}
$$

By equating coefficients, two independent differential equations are obtained

$$\dot{y}_0 = f_0(t, y_0) \tag{2.18}$$

$$\dot{y}_1 = \left.\frac{\partial f}{\partial y}\right|_{\epsilon=\text{const}} y_1 + \left.\frac{\partial f}{\partial \epsilon}\right|_{y=\text{const}} \tag{2.19}$$

that need to be solved simultaneously.

3 Thick muscle wrapping with constant conicity and constant length

This chapter lays the foundation for the continuous approach to wrapping thick muscles developed in this thesis. Therefore, the chapter starts with the mathematical definition of a "thick muscle" and presents a chain of beads with finite number of beads fitted into the muscle contour as a discretization. To begin with, only the part of a conical muscle wrapped around a convex surface is considered here and the continuous solution is derived as the limit case of a string of an infinite number of beads. This is done both at the position level and at the velocity level when the velocity transmission along the surface from one muscle end to the other is determined. In addition to the assumptions mentioned at the beginning, a constant muscle centerline length is assumed here.

3.1 Thick muscle model

To model a "thick muscle", it is assumed that its thickness can be defined for every point on its centerline. Therefore, it can be described by a function $b(s)$, where b is the half-thickness of the muscle's cross-section and s gives the position along the muscle's centerline. The length of the centerline is supposed to be constant and does not change when the muscle undergoes deformations due to being wrapped over obstacle surfaces.

Inspired by [20], this muscle can be discretized by a chain of N spherical "beads", which are inscribed into the muscle geometry and which are pairwise connected by massless threads of constant length $\Delta\bar{s}$ between their centers. In Fig. 3.1 this is shown for $N = 6$ and a muscle having the form of a cone with the constant cone half-angle α.
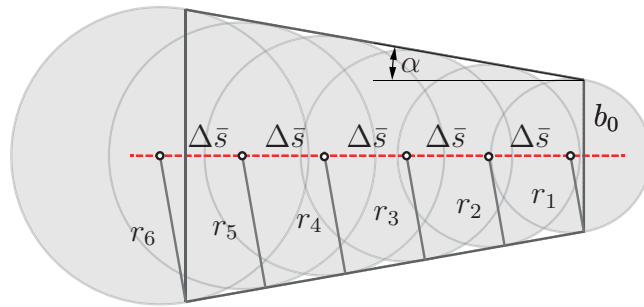
Figure 3.1: Chain of six spherical beads inscribed in a conical thick muscle
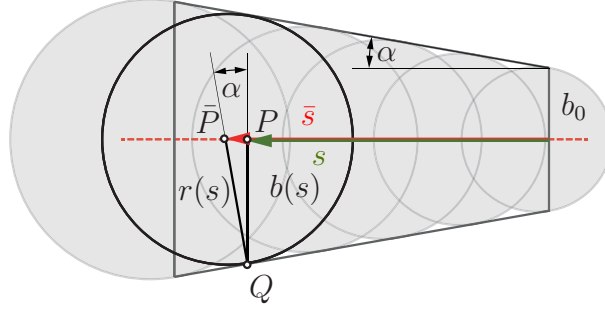
Figure 3.2: Relationship between bead radius $r(s)$ and muscle's half-thickness $b(s)$

Like illustrated in Fig. 3.2, the relationship between the radius of the inscribed bead touching the cone in point Q and the corresponding half-thickness $b(s)$ of the strand in this point is given by

$$r(s) = \frac{b(s)}{\cos\alpha} \quad . \tag{3.1}$$

It is obvious that the center $\bar{P}$ of this inscribed bead does not lie in point P given by s. Therefore, the variable $\bar{s}$ is introduced, giving the positions of the inscribed beads.

For a cone with half-thickness

$$b(s) = b_0 + s\tan\alpha \quad , \tag{3.2}$$

the relationship between s and $\bar{s}$ can be computed straightforwardly by

$$\bar{s} = s + b(s)\tan\alpha = b_0\tan\alpha + \frac{s}{\cos^2(\alpha)} \quad . \tag{3.3}$$

Like visualized in Fig. 3.3, the muscle must not necessarily have the form of a cone. Instead the strand's cross-section can be described by any function $b(s)$. The half-angle α then becomes variable and depends on s as

$$\tan(\alpha(s)) = \frac{d}{ds}b(s) \quad . \tag{3.4}$$

In this case, fitting the beads into the strand needs some additional computation compared to the cone where α is constant. Letting the distance $\Delta\bar{s}$ between the bead centers be constant, the position $\underline{r}_{\bar{P}}$ of a single bead on the strand's centerline is defined by given $\bar{s}$. The bead radius $r(\bar{s})$ and the corresponding centerline length $s(\bar{s})$ are then determined by solving the two-dimensional root function

$$\underline{F} = \underline{r}_{\bar{P}}(\bar{s}) + \underline{e}_n \cdot r(\bar{s}) - \underline{r}_Q(b(s)) = 0 \tag{3.5}$$

using Newton iterations, where $\underline{e}_n$ is the normal vector to the surface curve at contact point Q.
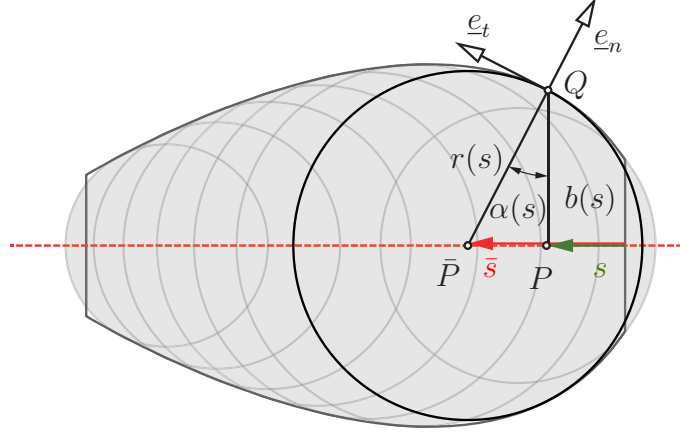
Figure 3.3: Chain of eight spherical beads inscribed in a thick muscle with non-constant conicity ($\alpha(s) \neq$ const)

3.2 Position analysis

3.2.1 Discrete wrapping by a chain of spherical beads

To obtain muscle paths, so-called wrapping obstacles have to be defined, representing bones, chords or ligaments, which limit and guide the muscles' movements. In a three-dimensional environment these wrapping obstacles are three-dimensional surfaces. Here, with the restriction to the two-dimensional case, a wrapping obstacle is a two-dimensional, continuous curve lying in a plane. For easier understanding and to simplify the later transferability to the three-dimensional case, these curves are nevertheless referred to as "surfaces" in the context of this work. Between origin and insertion, the thick muscle, which is modeled like described in Section **3.1**, wraps over the wrapping obstacle.

Let σ describe a natural coordinate along the wrapping surface curve. For illustration purposes, this curve is regarded as an ellipse with semi-major and semi-minor axes a_1, a_2 (Fig. 3.4). Also, the bead radius is assumed to correspond to that of an inscribing circle of a cone with constant cone half-angle α, i.e. $r_i = r_1 + \tan\alpha\,\bar{s}_i$, with $\bar{s}_i = (i-1)\,\Delta\bar{s}$ for $i = 2, \ldots, N$ with N being the total number of beads.

The radius vector $\underline{r}_{\bar{P}i}$ to the center of a bead "i" is given by

$$\underline{r}_{\bar{P}i}(\sigma_i) = \underline{x}_Q(\sigma_i) + r_i\,\underline{e}_n(\sigma_i) \qquad (3.6)$$

where $\underline{x}_Q$ is the radius vector to the contact point of the surface curve and $\underline{e}_n$ is the normal vector to the surface curve at this point.
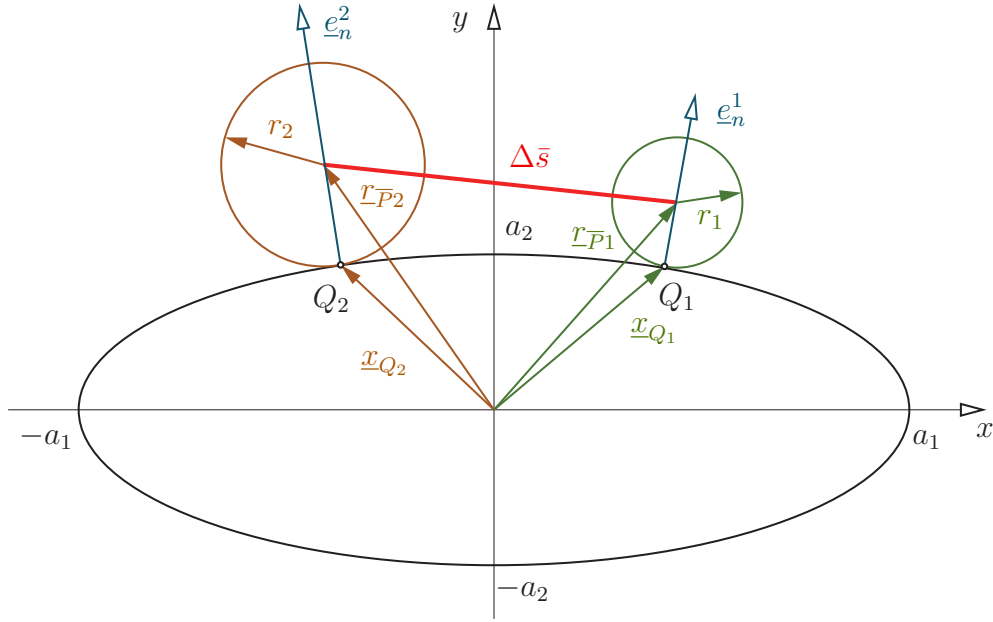
Figure 3.4: Sequence of two beads on an ellipse

For two consecutive beads, the constant-distance condition yields the root function

$$F(\sigma_i) = \left[\, \underline{r}_{\overline{P}i}(\sigma_i) - \underline{r}_{\overline{P}i-1}(\sigma_{i-1})\,\right]^2 - \Delta\bar{s}^2 = 0 \quad , \quad i = 2,\ldots,N \quad , \tag{3.7}$$

which can be solved successively for $\sigma_i, i = 2,\ldots,N$ starting at a given initial point $\underline{r}_{\overline{P}1}(\sigma_1) = \underline{x}_Q(\sigma_1) + r_1\,\underline{e}_n(\sigma_1)$ by Newton iterations using the scalar "Jacobians"

$$J_i(\sigma_i) = \frac{\mathrm{d}}{\mathrm{d}\sigma}F(\sigma_i) = 2\left[\,\underline{r}_{\overline{P}i}(\sigma_i) - \underline{r}_{\overline{P}i-1}(\sigma_{i-1})\,\right]\cdot\frac{\mathrm{d}}{\mathrm{d}\sigma}\,\underline{r}_{\overline{P}i}(\sigma_i) \tag{3.8}$$

where

$$\frac{\mathrm{d}}{\mathrm{d}\sigma}\,\underline{r}_{\overline{P}i}(\sigma_i) = \frac{\mathrm{d}}{\mathrm{d}\sigma}\,\underline{x}_Q(\sigma_i) + r_i\,\frac{\mathrm{d}}{\mathrm{d}\sigma}\,\underline{e}_n(\sigma_i) \quad . \tag{3.9}$$

For the example of a contact ellipse, it holds

$$\underline{x}_Q = \begin{bmatrix} a_1\cos(\sigma) \\ a_2\sin(\sigma) \end{bmatrix} \quad , \qquad \underline{e}_n(\sigma) = \frac{1}{\lambda}\begin{bmatrix} a_2\cos(\sigma) \\ a_1\sin(\sigma) \end{bmatrix} \quad \text{and} \tag{3.10}$$

$$\frac{\mathrm{d}}{\mathrm{d}\sigma}\,\underline{x}_Q = \begin{bmatrix} -a_1\sin(\sigma) \\ a_2\cos(\sigma) \end{bmatrix} \quad , \qquad \frac{\mathrm{d}}{\mathrm{d}\sigma}\,\underline{e}_n(\sigma) = \frac{1}{\rho}\begin{bmatrix} -a_2\sin(\sigma) \\ a_1\cos(\sigma) \end{bmatrix} \tag{3.11}$$

with σ as surface coordinate, ρ equal to the curvature radius (see Eq. (3.24) further below) and $\lambda = \sqrt{a_1^2\sin^2\sigma + a_2^2\cos^2\sigma}$.

3.2.2   Continuous wrapping as limit case

The continuous wrapping curve can be seen as the limit case of an infinite number of beads with an infinitesimally small distance $\Delta \bar{s}$ to their neighboring beads. Regarding two consecutive beads "i" and "$i+1$" (see Fig. 3.5), according to Huygens, the centers of curvature M_i and M_{i+1} lie on the evolute of the surface curve and thus on the surface normals $\underline{e}_n^i$ and $\underline{e}_n^{i+1}$. For the limit case of $\Delta \bar{s} \to 0$, M_i lies on the line connecting M_{i+1} and $\bar{P}_i$ and the distance between the centers of curvature is $\Delta \rho_i = \rho_{i+1} - \rho_i$.

In this case, the triangle $\bar{P}_i M_{i+1} \bar{P}_{i+1}$ can be used to determine the angle ψ_i^+ between the line connecting the bead centers "i" and "i+1" and the surface normal $\underline{e}_n^i$ at bead "i". Applying the law of cosines yields

$$\lim_{\Delta \bar{s} \to 0} \left\{ (\rho_{i+1} + r_{i+1})^2 = \Delta \bar{s}^2 + (\rho_i + \Delta \rho_i + r_i)^2 - 2\Delta \bar{s}(\rho_i + \Delta \rho_i + r_i)\cos\psi_i^+ \right\} \quad . \quad (3.12)$$
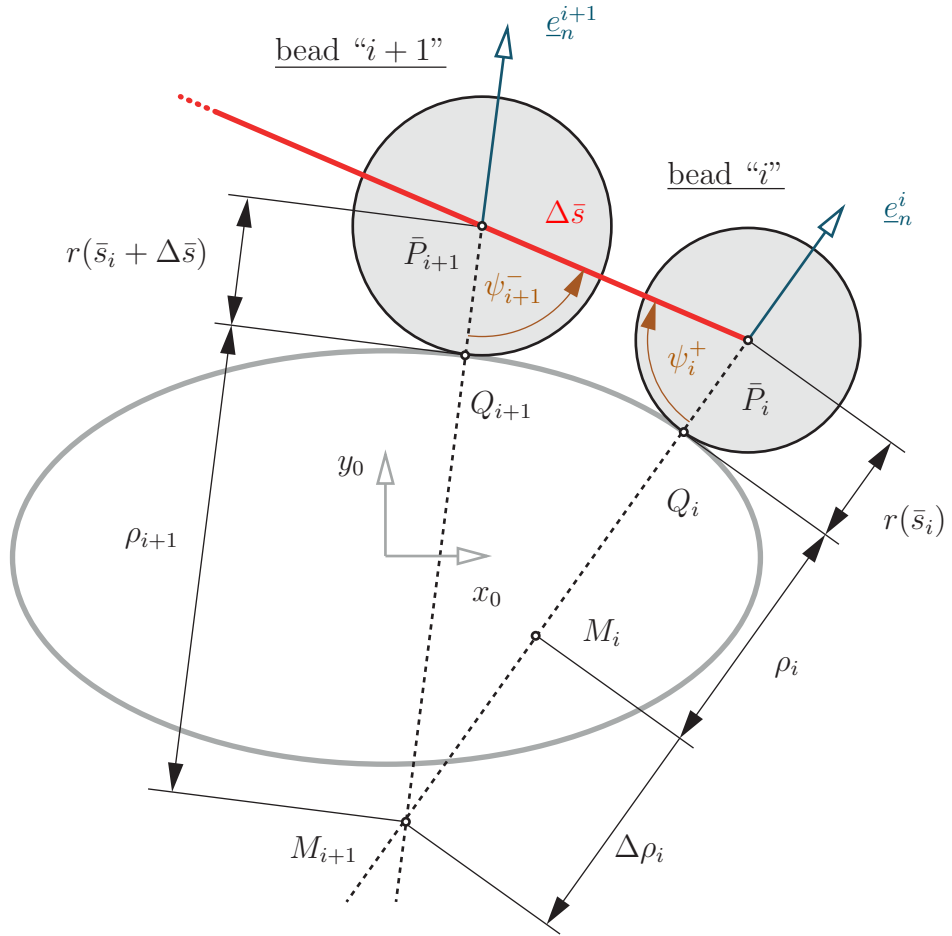
Figure 3.5: Thread angle at bead "i"

Inserting $r_{i+1} = r_i + \Delta \bar{s} \sin \alpha$, the equation can be converted to

$$\lim_{\Delta \bar{s} \to 0} \left\{ \cos \psi_i^+ = \cos \left(90° + \alpha \right) + \Delta \bar{s} \frac{\cos^2 \alpha}{2 \left(\rho_{i+1} + r_i \right)} \right\} \qquad (3.13)$$

$$\Rightarrow \lim_{\Delta \bar{s} \to 0} \psi_i^+ = 90° + \alpha . \qquad (3.14)$$

Analogously, for the angle ψ_{i+1}^- it holds

$$\lim_{\Delta \bar{s} \to 0} \psi_{i+1}^- = 90° - \alpha . \qquad (3.15)$$

Also, the angle at the last bead "N" between the free line and the surface normal vector for the case that the last bead is just touching the surface converges to this value for the limit case of $\Delta \bar{s} \to 0$

$$\psi_N^+ \to 90° + \alpha . \qquad (3.16)$$

An enveloping cone with the actual cone half-angle $\alpha(s) = \arctan \left(\mathrm{d}b / \mathrm{d}s \right)$ can be constructed for every bead in contact. Thus, the cone can be seen as the natural geometry of the continuous strand (Fig. 3.6). For constant cone half-angle α, the half-width b of the cross-section is given in terms of the continuous cone centerline
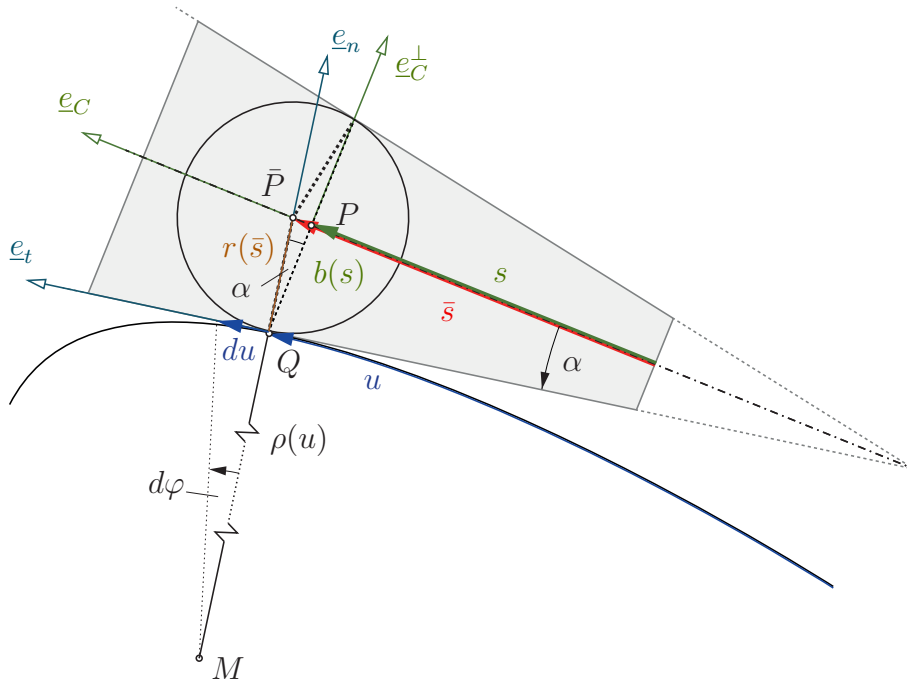
Figure 3.6: Envellopping cone at bead in contact as natural strand geometry

path length s as $b(s) = r(\bar{s})\cos\alpha$. The path length s thus "lags" behind the sum $\bar{s} = (i-1) \cdot \Delta\bar{s}$ of bead-pair threads as

$$s = \bar{s} - \sin\alpha\, r(\bar{s}) = \bar{s} - \sin\alpha\,\bar{s}\,\sin\alpha = \cos^2\alpha\,\bar{s} \ . \tag{3.17}$$

For general cross-sections $b(s)$ and in the limit $\Delta\bar{s} \to \mathrm{d}\bar{s}$, this leads to the infinitesimal relationship

$$\mathrm{d}s = \cos^2\alpha\,\mathrm{d}\bar{s} \ . \tag{3.18}$$

According to the constant-length assumption of the strand centerline, the increase $\mathrm{d}s$ of the length of the wrapped centerline must correspond to the projection of the infinitesimal displacement $\mathrm{d}\underline{r}_P$ of the center point P of the cone center on the free line, i. e.

$$\mathrm{d}s = \mathrm{d}\underline{r}_P \cdot \underline{e}_C \ , \tag{3.19}$$

where $\underline{e}_C$ is the normal vector to the cone front-end cross-section. The infinitesimal increment $\mathrm{d}\underline{r}_P$ of the center point P of the cone front cross-section when moving by $\mathrm{d}s$ on the centerline is hereby given by

$$\mathrm{d}\underline{r}_P = \rho\,\mathrm{d}\varphi\,\underline{e}_t + b(s)\,\mathrm{d}\varphi\,\underline{e}_C + \frac{\mathrm{d}b(s)}{\mathrm{d}s}\,\mathrm{d}s\,\underline{e}_C^{\perp} \tag{3.20}$$

where $\underline{e}_t$ is the tangent vector to the surface curve at contact point Q, ρ is the curvature radius of the wrapping surface curve at this point, $\underline{e}_C^{\perp}$ is the unit vector in direction of the cone cross-section and $\mathrm{d}\varphi$ is the infinitesimal rotation about the curvature center of the wrapping surface given by

$$\mathrm{d}\varphi = \frac{1}{\rho(\sigma)}\left\|\frac{\mathrm{d}}{\mathrm{d}\sigma}\underline{x}_Q(\sigma)\right\|\,\mathrm{d}\sigma \ . \tag{3.21}$$

The three components of the infinitesimal displacement $\mathrm{d}\underline{r}_P$ are shown in Fig. 3.7 a) for a constant cone half-angle α where the red arrow "1" designates the displacement by $\rho\,\mathrm{d}\varphi$ in direction of the surface tangent $\underline{e}_t$, the green arrow "2" represents the displacement in direction of $\underline{e}_C$ caused by the change of inclination due to the rotation by $\mathrm{d}\varphi$ about the instant center of rotation M (that is equivalent to the center of curvature) and the third component (marked by the blue arrow "3") is the displacement in direction of $\underline{e}_C^{\perp}$ provoked by the change of the cross-section $\mathrm{d}b(s)$. Vector addition of the three infinitesimal components results in the total infinitesimal displacement $\mathrm{d}\underline{r}_P$, like shown in Fig. 3.7 b).
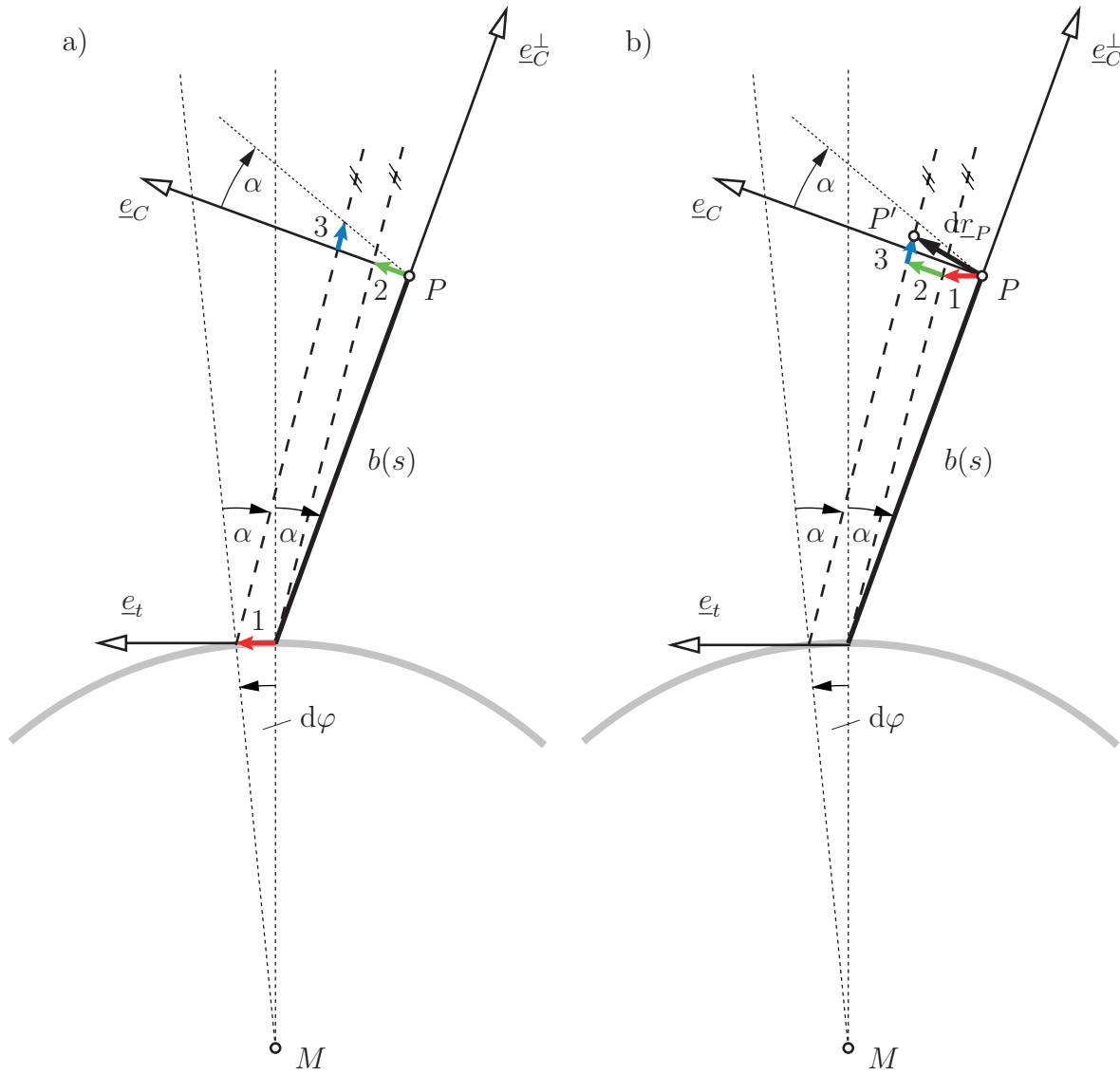
Figure 3.7: Three components of the infinitesimal displacement of point P for constant cone half-angle α a) single displacements at their origin of generation b) total displacement $\mathrm{d}\underline{r}_P$ as vector addition polygon

Inserting Eq. (3.20) into Eq. (3.19) leads to

$$\mathrm{d}s = [\,\rho(\sigma)\cos\alpha + b(s)\,]\,\mathrm{d}\varphi \quad. \tag{3.22}$$

A brief overview of the scalar products of the unit vectors $\underline{e}_C, \underline{e}_C^{\perp}, \underline{e}_t$ and $\underline{e}_n$ is given in appendix A. Combining Eq. (3.22) with Eq. (3.21) renders the ordinary differential equation for determination of $s(\sigma)$

$$\frac{\mathrm{d}s}{\mathrm{d}\sigma} = \frac{1}{\rho(\sigma)}\left\|\frac{\mathrm{d}}{\mathrm{d}\sigma}\underline{x}_Q(\sigma)\right\| [\,\rho(\sigma)\cos\alpha(s) + b(s)\,] = f(s,\sigma) \quad. \tag{3.23}$$

For the example of the ellipse with the semiaxis lengths a_1 and a_2, $\rho(\sigma)$ and $\mathrm{d}\varphi$ are given by

$$\rho(\sigma) = \frac{\sqrt{a_1^2\sin^2\sigma + a_2^2\cos^2\sigma}^{\,3}}{a_1\,a_2} \quad\text{and} \tag{3.24}$$

$$\mathrm{d}\varphi = \frac{a_1\,a_2}{a_1^2\sin^2\sigma + a_2^2\cos^2\sigma}\,\mathrm{d}\sigma \tag{3.25}$$

leading to the ODE

$$\frac{\mathrm{d}s}{\mathrm{d}\sigma} = a_1 a_2\,\frac{\rho(\sigma)\cos\alpha(s) + b(s)}{a_1^2\sin^2\sigma + a_2^2\cos^2\sigma} = f(s,\sigma) \quad. \tag{3.26}$$

After solving Eq. (3.23) rendering $s(\sigma)$, the radius vector $\underline{r}_P(s)$ to the centerline of the continuous strand can be computed as

$$\underline{r}_P(s) = \underline{x}_Q(\sigma) + b(s)\,[\,\cos\alpha(s)\,\underline{e}_n(\sigma) - \sin\alpha(s)\,\underline{e}_t(\sigma)\,] \quad. \tag{3.27}$$

3.2.3 Comparison of bead and continuous method

The presented continuous solution was compared to the discrete bead model for different cases. The first example presented here is the contact of a conical strand with constant half-angle $\alpha = $ const on a circular wrapping surface curve with constant curvature radius $\rho = R = $ const. Fig. 3.8 visually shows the accordance between the red centerline of the bead method and the green centerline of the analytical method. Using the relationship between s and $\bar{s}$ given in Eq. (3.17) the red and the green centerline can easily be converted into each other for the limit case of $\Delta\bar{s} \to 0$.

Additionally, the relationships between significant variables are exemplarily investigated for this example and the limit case of $\Delta\bar{s} \to 0$. In case of a circular wrapping surface curve, the natural surface coordinate $\sigma(s)$ and the angle $\varphi(s)$ around the center of curvature M, which is constantly the center of the circle here, are identical (see Fig. 3.9).
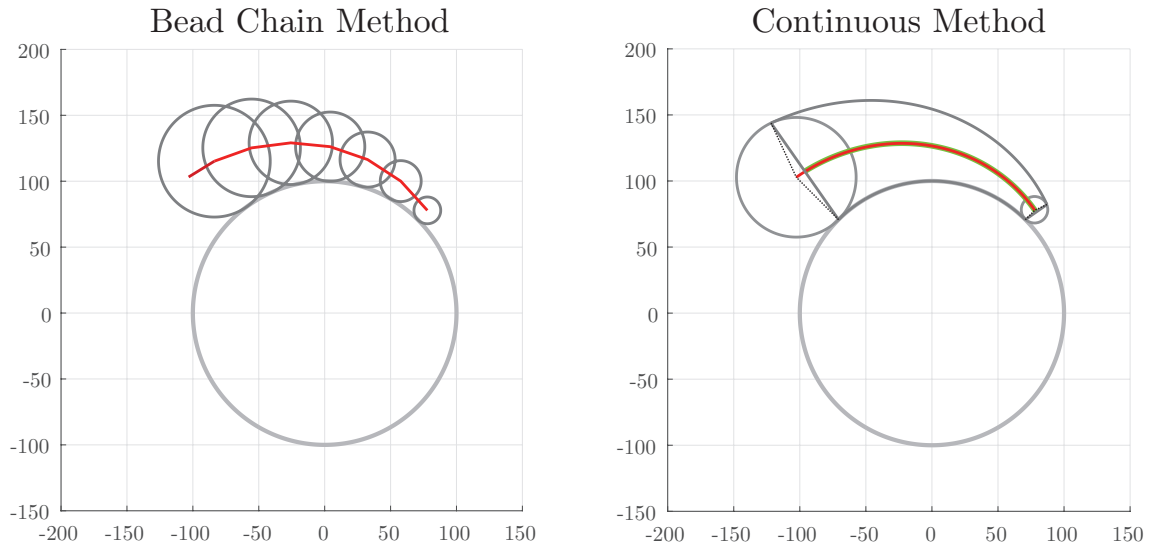
Figure 3.8: Comparison of the discrete bead chain method to the continuously wrapped cone with fitted inscribed beads at both ends for $a_1 = a_2 = R, \alpha = \text{const}$
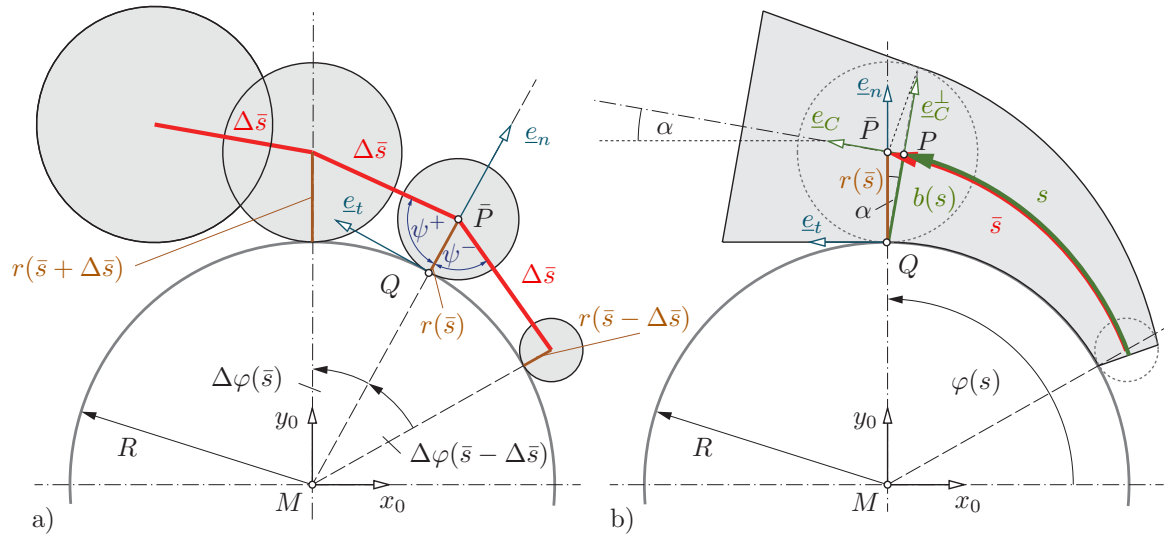
Figure 3.9: Comparison of the bead and the continuous method for a conical muscle with a constant half-angle α wrapping on a circle with constant curvature radius $\rho = R = \text{const}$ a) bead chain method for a finite number of N beads b) continuous solution and bead chain method for an infinite number of beads

Relationship between s and φ

Let the half-width b of the cross-section be defined by

$$b(s) = \tan\alpha\, s \tag{3.28}$$

and the curvature radius of the surface curve be constantly $\rho = R$. Inserting this into Eq. (3.22) leads to

$$\mathrm{d}s = (R\cos\alpha + \tan\alpha\, s)\mathrm{d}\varphi \quad . \tag{3.29}$$

Separating and integrating this equation yields the relationship between s and φ for the initial values $s_0 = \varphi_0 = 0$ as

$$\int_{s_0}^{s} \frac{1}{R\cos\alpha + \tan\alpha\tilde{s}}\,\mathrm{d}\tilde{s} = \int_{\varphi_0}^{\varphi}\mathrm{d}\tilde{\varphi} \tag{3.30}$$

$$\Rightarrow s(\varphi) = \frac{R\cos^2\alpha}{\sin\alpha}\left(e^{\tan\alpha\,\varphi} - 1\right) \quad . \tag{3.31}$$

As was to be expected, for a cone wrapping on a circle, the curve of its midline s depending on φ has the form of a logarithmic spiral.

Increment angle $\Delta\varphi(\bar{s})$

Looking at the bead chain method with a finite number of beads (left part of Fig. 3.9), the increment angle $\Delta\varphi(\bar{s})$ changes from step to step for $\Delta\bar{s}$ having a constant length. For the triangle $\bar{P}(\bar{s})M\bar{P}(\bar{s}+\Delta\bar{s})$, the law of cosines can be applied, leading to

$$\Delta\bar{s}^2 = [R + r(\bar{s}+\Delta\bar{s})]^2 + [R + r(\bar{s})]^2 - 2\,[R + r(\bar{s}+\Delta\bar{s})]\,[R + r(\bar{s})]\cos\left(\Delta\varphi(\bar{s})\right) \quad . \tag{3.32}$$

For small increments $\Delta\bar{s} = \mathrm{d}\bar{s}$ and $\Delta\varphi = \mathrm{d}\varphi$, the cosines can be approximated by $\cos\left(\mathrm{d}\varphi(\bar{s})\right) \approx 1 - \mathrm{d}\varphi^2/2$. Given $r(\bar{s}+\mathrm{d}\bar{s}) = r(\bar{s}) + \mathrm{d}r$ and $\mathrm{d}r = \sin\alpha\,\mathrm{d}\bar{s}$, it follows

$$\mathrm{d}\bar{s}^2 = \sin^2\alpha\,\mathrm{d}\bar{s}^2 + [R + r(\bar{s})]^2\,\mathrm{d}\varphi^2 + [R + r(\bar{s})]\sin\alpha\,\mathrm{d}\bar{s}\,\mathrm{d}\varphi^2 \quad . \tag{3.33}$$

Neglecting the last higher order term and inserting $r(\bar{s}) = \sin\alpha\,\bar{s}$ yields the relationship

$$\mathrm{d}\varphi = \frac{\cos\alpha}{R + \sin\alpha\,\bar{s}}\mathrm{d}\bar{s} \quad . \tag{3.34}$$

Relationship between $\bar{s}$ and φ

Integrating Eq. (3.34) provides the relationship between $\Delta\varphi$ and $\bar{s}$

$$\int_{\bar{s}_0}^{\bar{s}} \frac{\cos\alpha}{R + \sin\alpha\,\tilde{s}}\,\mathrm{d}\tilde{s} = \int_{\varphi_0}^{\varphi} \mathrm{d}\tilde{\varphi} \quad . \tag{3.35}$$

For the initial values $\varphi_0 = \bar{s}_0 = 0$, one obtains

$$\bar{s}(\varphi) = \frac{R}{\sin\alpha}\left(e^{\tan\alpha\,\varphi} - 1\right) \quad . \tag{3.36}$$

Using Eq. (3.17), Eq. (3.31) can also be transformed into Eq. (3.36), which is a proof for the consistence of the equations.

Comparison for ρ and α not constant

The example presented before of a cone wrapping on a circle is a special case where α and ρ are constant. The derived continuous solution, however, is more generally applicable. This is exemplarily shown in Fig. 3.10 a) for a cone wrapping on an ellipse, thus here the radius of curvature ρ is not constant and in b) for a muscle with a non-constant variation of its cross-section wrapping on a circle. The green line shows the continuous midline path and the red line represents the discrete "bead" centerline. In both cases, the continuous method converges to the discrete method for $\Delta\bar{s} \to 0$. Clearly, the start and end of the continuous path correspond to the centers of the chord length of the inscribed circles at the start and end, respectively, showing the general applicability of the method as limit case $\Delta\bar{s} \to 0$ of the bead chain method.
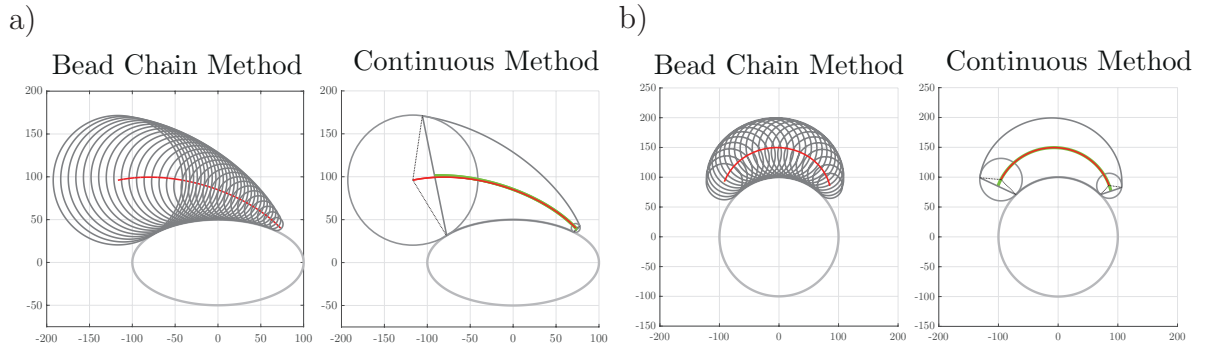
Figure 3.10: Comparison of the discrete bead chain method to the continuously wrapped cone with fitted inscribed beads at both ends for a) $\rho \neq \mathrm{const}, \alpha = \mathrm{const}$ b) $\rho = \mathrm{const}, \alpha \neq \mathrm{const}$

3.2.4   Kink between wrapped centerline free segment line

Interestingly, the tangent to the wrapped centerline of the continuous muscle strand at the end of the wrapped segment marked in green in Fig. 3.11 is not parallel to the free, straight centerline of the unwrapped segment (marked in red) but displays a "kink". The resulting angle between the tangent to the centerline and the normal to the front cross-section of the continuous strand is called β and can be determined by

$$\tan \beta = \frac{\mathrm{d}\underline{r}_P \cdot \underline{e}_C^{\perp}}{\mathrm{d}\underline{r}_P \cdot \underline{e}_C} \quad . \tag{3.37}$$

While the projection of $\mathrm{d}\underline{r}_P$ to the normal to the cross-section $\underline{e}_C$ was already computed in Eq. (3.22), projecting $\mathrm{d}\underline{r}_P$ to the cone cross-section direction $\underline{e}_C^{\perp}$ leads to

$$\mathrm{d}\underline{r}_P \cdot \underline{e}_C^{\perp} = b \, \tan\alpha \, \mathrm{d}\varphi \quad . \tag{3.38}$$
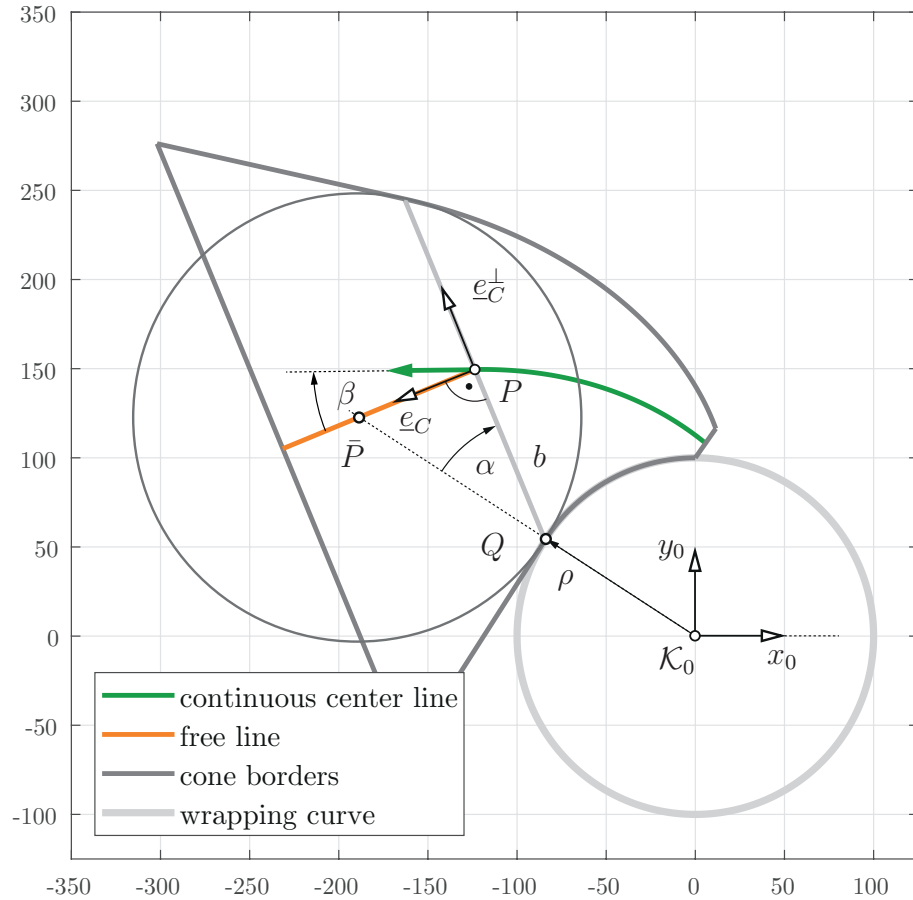
Figure 3.11: "Kink" between tangent to wrapped centerline and free line, illustrated for the example of a cone wrapping on a circle

Inserting both in (3.37), gives for the angle β between the tangent to the centerline and the normal to the front cross-section of the continuous strand

$$\tan\beta = \frac{b(s)\,\tan\alpha}{\rho(\sigma)\,\cos\alpha + b(s)} \quad . \tag{3.39}$$

However, this seemingly paradoxical behavior is consistent for the limit $\Delta\bar{s} \to 0$ for the inscribed circle at point Q, where the free line is equal to the external thread at the last bead, which is tilted by α with respect to the surface tangent (Fig. 3.11).

For the special case of a cone wrapping on a circle, the question whether for a growing length of the wrapped strand $s \to \infty$ the kink angle β will grow infinitesimal large or whether it converges to an upper limit was investigated. For this case, it holds $b(s) = b_0 + \tan\alpha\, s$ and $\rho(\sigma) = R = \text{const}$, thus, Eq. (3.39) becomes

$$\tan\beta = \frac{\tan\alpha\, b_0 + \tan^2\alpha\, s}{R\cos\alpha + b_0 + \tan\alpha\, s} \quad . \tag{3.40}$$

So, for a cone wrapping on a circle and the limit case of $s \to \infty$,

$$\lim_{s\to\infty}\tan(\beta) = \tan(\alpha) \tag{3.41}$$

$$\Rightarrow \lim_{s\to\infty}\beta = \alpha \tag{3.42}$$

the kink angle β converges to the cone half-angle α.

3.3 Velocity analysis

To derive the velocity transmission along the surface of a thick, wrapped muscle strand, the propagation of infinitesimal displacements is examined, i.e., the transmission of an infinitesimal displacement du_0 at the start of the wrapping segment to the corresponding infinitesimal displacement du_E at its end. For simplicity reasons, these are expressed in terms of velocities which correspond to the infinitesimal displacements divided by dt resulting in $\dot{u}_0$ and $\dot{u}_E$, where the dot notation is used to indicate the time derivative. The quotient of these velocities yields the "Jacobian" from start to end of a wrapped muscle.

3.3.1 Discrete bead chain approach

For the discrete bead method, there are two possibilities of achieving this:
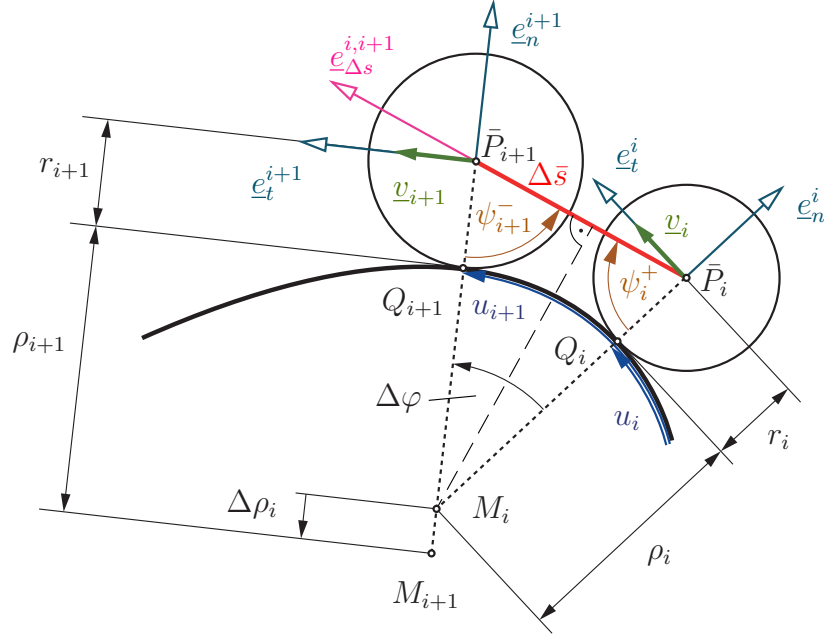
Figure 3.12: Velocity transmission between two neighbouring beads (curvature centers for $\Delta \bar{s} \to 0$)

(A) by shifting the start by a small increment and re-computing the bead chain, and
(B) by propagating the midpoint velocities pair by pair considering the condition of constant thread length between two adjacent midpoints.

Method A is straightforward. For method B, the propagation results from

$$\underline{v}_{i+1} \cdot \underline{e}_{\Delta s}^{i,i+1} = \underline{v}_i \cdot \underline{e}_{\Delta s}^{i,i+1} \quad \text{with} \quad \underline{e}_{\Delta s}^{i,i+1} = \frac{\underline{r}_{\bar{P}i+1} - \underline{r}_{\bar{P}i}}{\| \underline{r}_{\bar{P}i+1} - \underline{r}_{\bar{P}i} \|} \quad ; \quad i = 1, \dots, N-1 \qquad (3.43)$$

as can be seen in Fig. 3.12. Since $\underline{v}_i = v_i \, \underline{e}_t^i$ with scalar v_i, this leads to

$$v_{i+1} = \frac{\underline{e}_t^i \cdot \underline{e}_{\Delta s}^{i,i+1}}{\underline{e}_t^{i+1} \cdot \underline{e}_{\Delta s}^{i,i+1}} \, v_i = \frac{\sin \psi_i^+}{\sin \psi_{i+1}^-} \, v_i \quad ; \quad i = 1, \dots, N-1 \qquad (3.44)$$

with angle ψ_i^- between the surface normal at bead "i" and the "predecessor" thread $\underline{e}_{\Delta s}^{i-1,i}$ (Fig. 3.12). For comparison purposes, the velocity at the bead midpoint is transformed to the velocity $\dot{u}_i$ at the contact surface by the scaling factor $\rho/(\rho + r)$, leading to the final velocity propagation formula

$$\dot{u}_{i+1} = \frac{\sin \psi_i^+}{\sin \psi_{i+1}^-} \frac{\rho_i (\rho_{i+1} + r_{i+1})}{\rho_{i+1} (\rho_i + r_i)} \, \dot{u}_i \quad ; \quad i = 1, \dots, N-1 \quad , \qquad (3.45)$$

which can be solved recursively starting from a given velocity $\dot{u}_1$.

3.3.2   Continuous approach

In the continuous case, the centers of curvature lie on the evolute of the surface curve, as it was derived by Huygens and described in Section **2.1.4**. Thus two infinitesimally neighboring centers of curvature M_i, M_{i+1} are separated by the difference $\Delta\rho_i$ of curvature radii between them, as illustrated in Fig. 3.12. In the limit $\Delta\bar{s} \to 0$, it hence follows

$$(\rho_i + r_i)\sin(\psi_i^+) = (\rho_{i+1} + r_{i+1} - \Delta\rho_i)\sin(\psi_{i+1}^-) \ . \tag{3.46}$$

Inserting this into the velocity transmission equation Eq. (3.45) provides for the velocity transmission from $\dot{u}_i$ to $\dot{u}_{i+1}$ for two neighboring beads

$$\frac{1}{\rho_i}\left(\rho_{i+1} + r_{i+1} - \Delta\rho_i\right)\sin(\psi_{i+1}^-)\,\dot{u}_i = \frac{1}{\rho_{i+1}}\left(\rho_{i+1} + r_{i+1}\right)\sin(\psi_{i+1}^-)\,\dot{u}_{i+1} \tag{3.47}$$

from where one obtains by setting $\rho_{i+1} = \rho_i + \Delta\rho_i$ and neglecting higher order terms in $\Delta\rho$,

$$\frac{\dot{u}_{i+1}}{\dot{u}_i} = \frac{\rho_{i+1}}{\rho_i}\left(1 - \frac{\Delta\rho_i}{\rho_{i+1} + r_{i+1}}\right)$$

$$\approx \left(1 + \frac{\Delta\rho_i}{\rho_i}\right)\left(1 - \frac{\Delta\rho_i}{\rho_i + r_i}\right)$$

$$\approx 1 + \frac{r_i}{\rho_i\left(\rho_i + r_i\right)}\Delta\rho_i \ . \tag{3.48}$$

By concatenating the pairwise velocity transmission for all $N-1$ beads with $i = 2,\ldots,N$ after given bead "1" it follows

$$\frac{\dot{u}_N}{\dot{u}_1} = \left[1 + \eta_1\,\Delta\rho_1\right]\left[1 + \eta_2\,\Delta\rho_2\right]\ldots\left[1 + \eta_{N-1}\,\Delta\rho_{N-1}\right] \tag{3.49}$$

for the velocity transmission between the first and the last beat with

$$\eta_i = \frac{r_i}{\rho_i\left(\rho_i + r_i\right)} \ . \tag{3.50}$$

Multiplicated, the summands can be grouped together by the following summations

$$\frac{\dot{u}_N}{\dot{u}_1} = 1 + \sum_{i=1}^{N-1}\eta_i\,\Delta\rho_i + \sum_{i_1=1}^{N-1}\sum_{i_2=i_1+1}^{N-1}\eta_{i_1}\eta_{i_2}\,\Delta\rho_{i_1}\Delta\rho_{i_2}$$

$$+ \sum_{i_1=1}^{N-1}\sum_{i_2=i_1+1}^{N-1}\sum_{i_3=i_2+1}^{N-1}\eta_{i_1}\eta_{i_2}\eta_{i_3}\,\Delta\rho_{i_1}\Delta\rho_{i_2}\Delta\rho_{i_3}$$

$$+ \ \ldots \ . \tag{3.51}$$

For small $\Delta\rho_i$ the velocity transmission can be approximated by the Taylor series for the exponential function $\exp\left(\sum_{i=1}^{N-1}\eta_i\,\Delta\rho_i\right)$ centered at zero. The complete proof is given in appendix B. Thus, according to this, the total geometric sequence can be rewritten as

$$
\lim_{\Delta\rho_i\to 0}\left(1+\eta_1\,\Delta\rho_1\right)\left(1+\eta_2\,\Delta\rho_2\right)\ldots\left(1+\eta_{N-1}\,\Delta\rho_{N-1}\right)
$$

$$
=\lim_{\Delta\rho_i\to 0}1+\left[\sum_{i=1}^{N-1}\eta_i\,\Delta\rho_i\right]^1+\frac{1}{2}\left[\sum_{i=1}^{N-1}\eta_i\,\Delta\rho_i\right]^2+\frac{1}{3!}\left[\sum_{i=1}^{N-1}\eta_i\,\Delta\rho_i\right]^3
$$

$$
+\ldots+\frac{1}{k!}\left[\sum_{i=1}^{N-1}\eta_i\,\Delta\rho_i\right]^k+\ldots+\frac{1}{(N-1)!}\left[\sum_{i=1}^{N-1}\eta_i\,\Delta\rho_i\right]^{N-1}
$$

$$
=\lim_{\Delta\rho_i\to 0}\exp\left(\sum_{i=1}^{N-1}\eta_i\,\Delta\rho_i\right)\tag{3.52}
$$

For the limit $\Delta\bar{s}\to 0$. it follows $\Delta\rho\to\mathrm{d}\rho$ and $\mathrm{d}\rho=\mathrm{d}\rho/\mathrm{d}\sigma\,\mathrm{d}\sigma$, giving for the quotient of the velocities $\dot{u}_E,\dot{u}_0$ at the end and the start of the wrapped segment, respectively, the continuous solution

$$
\frac{\dot{u}_E}{\dot{u}_0}=\exp\left(\int_{\sigma_0}^{\sigma_E}\frac{r(s(\sigma))}{\rho(\sigma)\left[\,\rho(\sigma)+r(s(\sigma))\,\right]}\cdot\frac{\mathrm{d}\rho}{\mathrm{d}\sigma}\,\mathrm{d}\sigma\right)\tag{3.53}
$$

where $s(\sigma)$ is determined by the ODE Eq. (3.26) and $r(s)=b(s)/\cos\alpha(s)$. Denoting the exponent in Eq. (3.53) by $\kappa(\sigma)$, the quotient of output to input velocity can be described by

$$
\frac{\dot{u}_E}{\dot{u}_0}=e^{\kappa(\sigma_E)}\tag{3.54}
$$

where $\kappa(\sigma)$ results from numerical integration of the two coupled ODEs

$$
\frac{d\kappa}{d\sigma}=\frac{r(s)}{\rho(\sigma)\left[\,\rho(\sigma)+r(s)\,\right]}\cdot\frac{\mathrm{d}\rho}{\mathrm{d}\sigma}\quad,\tag{3.55}
$$

$$
\frac{\mathrm{d}s}{\mathrm{d}\sigma}=\frac{1}{\rho(\sigma)}\left\|\frac{\mathrm{d}}{\mathrm{d}\sigma}\underline{x}_Q(\sigma)\right\|\left[\,\rho(\sigma)\cos\alpha(s)+b(s)\,\right]\quad.\tag{3.56}
$$

For the example of the ellipse, one obtains for instance

$$
\frac{d\kappa}{d\sigma}=\frac{r(s)}{\rho(\sigma)\left[\,\rho(\sigma)+r(s)\,\right]}\cdot\frac{\mathrm{d}\rho}{\mathrm{d}\sigma}\quad,\tag{3.57}
$$

$$
\frac{\mathrm{d}s}{\mathrm{d}\sigma}=a_1\,a_2\,\frac{\rho(\sigma)\cos\alpha(s)+b(s)}{a_1^2\sin^2\sigma+a_2^2\cos^2\sigma}\quad,\tag{3.58}
$$

with

$$
\frac{d\rho}{d\sigma}=\frac{3}{2}\,(\,a_1^2-a_2^2\,)\,\sin\sigma\cos\sigma\,\sqrt{\frac{\cos^2\sigma}{a_1^2}+\frac{\sin^2\sigma}{a_2^2}}\quad.\tag{3.59}
$$

Note that if one stores the function $s(\sigma)$ after solving the ODE Eq. (3.23) (e. g. by table lookup and interpolation), one can dispense of the second ODE Eq. (3.56) and only integrate the first one Eq. (3.55). However, in the present case simply the two coupled ODEs were integrated using a standard ODE integrator such as Matlab ode45, which rendered good results even for low accuracy (RELTOL=ABSTOL=10^{-1}).

3.3.3   Case examples

To illustrate Eq. (3.53) and deepen the understanding, it is examined for three different case examples shown in Fig. 3.13: An infinitesimal thin line, a muscle strand with constant thickness and a cone wrapped on a circle.

a) Case 1: Infinitesimally thin line

b) Case 2: Constant thickness

c) Case 3: Cone wrapped on circle
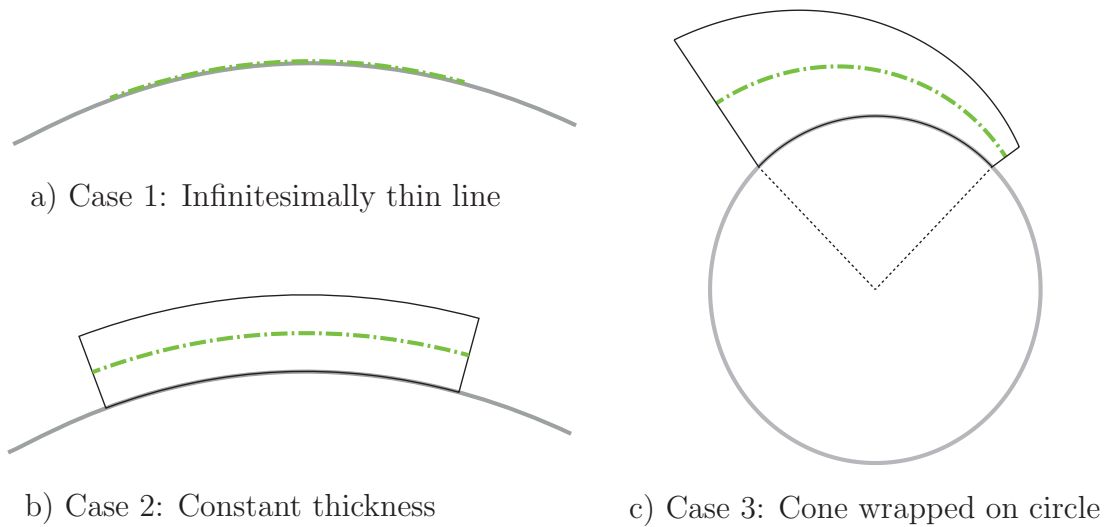
Figure 3.13: Three case examples for illustration of the velocity transmission

Case example 1: Infinitesimally thin line

In the case of an infinitesimally thin line, the strands cross-section is zero, so it holds $r = 0$ and, hence, for the velocity transmission

$$\frac{\dot{u}_E}{\dot{u}_0} = e^0 = 1 \quad , \tag{3.60}$$

meaning that the velocity is the same at both ends, which is the expected result for a thin line.

Case example 2: Strand with constant thickness

For a strand with a constant thickness b it holds $r = b = \text{const}$. Hence, for the velocity transmission from start to end, it applies

$$\frac{\dot{u}_E}{\dot{u}_0} = \exp\left(\int_{\sigma_0}^{\sigma_E} \frac{r}{\rho(\sigma)\,[\,\rho(\sigma)+r\,]}\,\rho'\,\mathrm{d}\sigma\right) \quad . \tag{3.61}$$

The substitution $\mathrm{d}\rho = \rho'\,\mathrm{d}\sigma$ yields

$$\frac{\dot{u}_E}{\dot{u}_0} = \exp\left(\int_{\rho_0}^{\rho_E} \frac{r}{\rho\,[\,\rho+r\,]}\,\mathrm{d}\rho\right) = \frac{(\rho_0+r)\,\rho_E}{\rho_0\,(\rho_E+r)} \quad . \tag{3.62}$$

To verify this result, the velocity transmission from start to end of the strand is derived in an alternative way. For $r = b = \text{const}$, it holds $\alpha = 0$ and the points $\bar{P}_i$ and P_i are identical and lie on the surface normal. Therefore, the velocity transmission can also be derived by using the instantaneous centers of rotation, which are identical to the centers of curvature (see Fig. 3.14). According to the assumption that the length of the centerline is constant, it holds

$$v_E = v_0 \tag{3.63}$$

for these velocities. To relate them to the velocities of the contact points Q_0 and Q_E at the surface, the instantaneous center of rotation is used and one obtains

$$v_0 = \dot{u}_0\frac{\rho_0+r}{\rho_0} \quad \text{and} \tag{3.64}$$

$$v_E = \dot{u}_E\frac{\rho_E+r}{\rho_E} \quad . \tag{3.65}$$
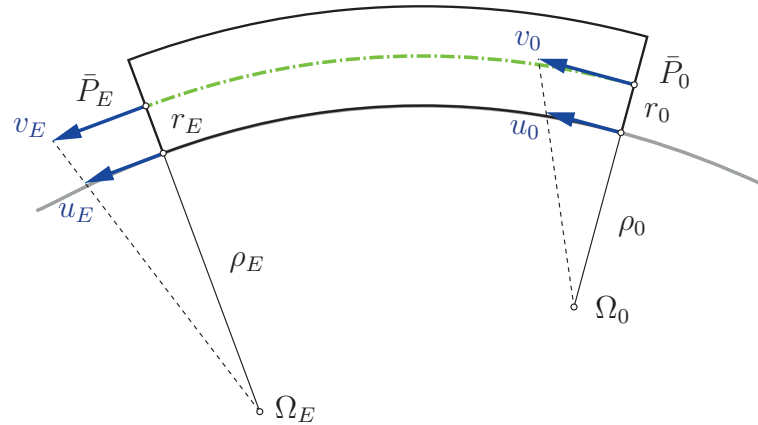
Figure 3.14: Instantaneous centers of rotation Ω_0 and Ω_E at both ends of a wrapped strand with constant cross-section

The velocity transmission $\dot{u}_E/\dot{u}_0$ is obtained by equating the right-hand sides of these equations yielding

$$\frac{\dot{u}_E}{\dot{u}_0} = \frac{(\rho_0 + r)\,\rho_E}{\rho_0\,(\rho_E + r)} \quad, \tag{3.66}$$

which is the same as derived above in Eq. (3.62).

Case example 3: Cone wrapped on circle

The third considered case example, shown in Fig. 3.13 c), is a cone with constant half-angle $\alpha = $ const wrapped on a circle with constant radius $\rho = R = $ const. Thus, it holds

$$\rho' = 0 \quad, \tag{3.67}$$

which leads to the velocity transmission

$$\frac{\dot{u}_E}{\dot{u}_0} = \exp\left(\int_{\sigma_0}^{\sigma_E} \frac{r(s(\sigma))}{R\,[\,R + r(s(\sigma))\,]} \cdot 0 \,\mathrm{d}\sigma\right) = 1 \quad. \tag{3.68}$$

This, too, corresponds to the expected result because both endpoints of the wrapped cone in contact with the circular surface move on the same circular path and the arc length between both points remains constant (the circle could rotate underneath the cone without changing its wrapped geometry).

3.3.4 Numerical comparison

The discrete and continuous approaches were compared for an ellipse ($a_1 = 100, a_2 = 50$) as contact curve and a total of $90°$ of polar angle starting at the vertical apex, as illustrated in Fig. 3.15. Hereby, for the discrete approach, both methods were applied, i.e. (a) by shifting the initial bead by a small amount ($\Delta\sigma = 0.0001$) ("Bead A") and (b) by the pairwise transmission of the velocities ("Bead B").

The results of the velocity transmission $\dot{u}_0/\dot{u}_E$ are shown in Table 3.1 for the continuous method and the discrete method for different numbers of beads and discrete transmission methods. For the bead method, the combinations of the number of beads N and the distance between the beads $\Delta\bar{s}$ were chosen to cover approximately the same elliptical arc described above. The results for the continuous method were obtained for the same startpoint and endpoint of the corresponding bead chain. For finer

Comparison between Bead Chain Method and Continuous Method
for b0 = 5, alpha = 20°, a$_1$ = 100, a$_2$ = 50
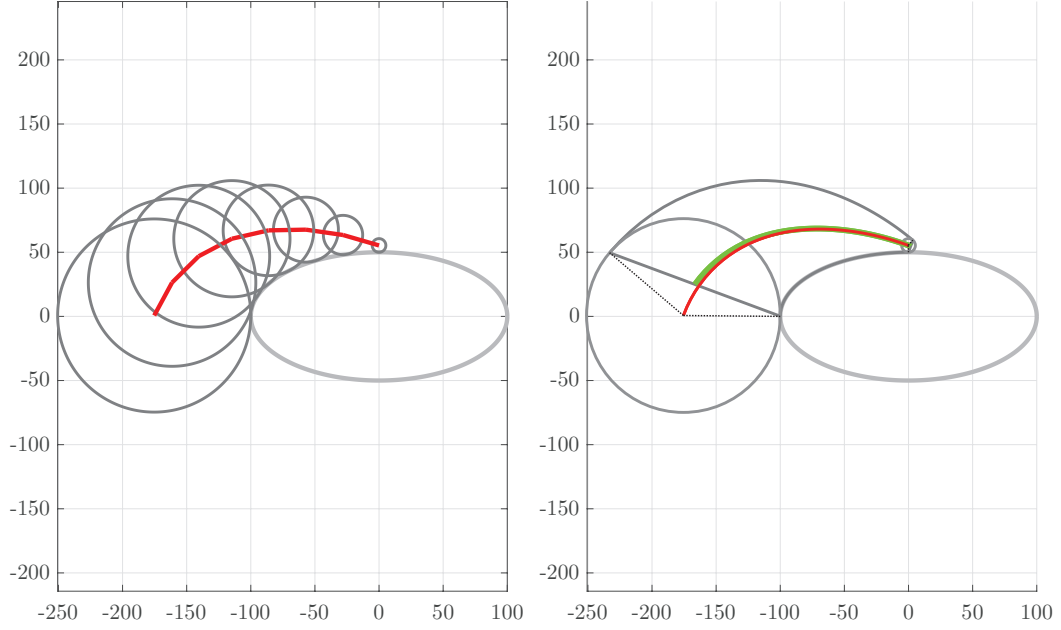
Figure 3.15: Test example for velocity transmission

Table 3.1: Comparison of velocity transmission $\dot{u}_E/\dot{u}_0$ from start to end

N	$\Delta\bar{s}$	Velocity Transmission $\dot{u}_E/\dot{u}_0$			CPU d/c	
		Bead A	Bead B	continuous	Bead A	Bead B
8	29.231	0.45413	0.45413	0.45108	2.42	16.65
16	13.67694	0.45174	0.45174	0.45108	3.20	17.65
32	6.62157	0.45124	0.45123	0.45108	5.20	18.82
64	3.258655	0.45112	0.45112	0.45108	11.12	21.36
128	1.616548	0.45109	0.45109	0.45108	24.44	26.88
256	0.80511	0.45109	0.45108	0.45108	54.83	36.29

discretizations both computations of the bead method converge to the result of the continuous approach proving the consistency of the latter.

In Table 3.1, the relative computation time as factor discrete/continuous ("CPU d/c") is given for different numbers of beads, which was computed in Matlab using a Newton tolerance 10^{-6} and ode45 with relative tolerance 10^{-6} and absolute tolerance 10^{-3}. Clearly, the continuous method is more efficient than the discrete method by a factor of 2.4 to 55 depending on the number of beads and the chosen discrete transmission method.

4 Wrapping and sliding with variable conicity and constant length

In the last chapter, an approach was presented for wrapping a thick, conical muscle (with the cone half-angle α being constant) over an arbitrary convex surface on a given arc length. This approach is now being extended for variable conicity ($\alpha \neq$ const) as well as to include free endpoints O and I (inspired by the muscle's origin and insertion points) that can move freely except for the constraint that the length ℓ of the muscle's centerline remains constant. Accordingly, such a thick muscle consists of a wrapped segment (between the points A and B, see Fig. 4.1) in the middle, which is in contact with the surface and two free, straight ends on both sides. Let s denote the centerline path length. The length of the centerline is measured separately for each segment: Hereby, s_A is the length of the straight connection from point O to point A, s_{AB} is the length of the centerline of the wrapped strand segment between the points A and B, and s_{BI} is the length of the straight line segment between the points B and I. Let the position of point O be a function of time t. Then all quantities of the wrapped strand will be functions of two independent variables: the surface coordinate σ indicating the location and progress along the strand at the time t, and the time t denoting the change at a location σ when time t changes. The velocity of the free endpoint I can be split into two components: The component $v_I^{\parallel}$ in the direction $\underline{e}_{CB}$ of the free, straight centerline that is normal to the muscle's cross-section in B and the component $v_I^{\perp}$ perpendicular to the first one in the direction of $\underline{e}_{CB}^{\perp}$. The same applies to $v_O^{\parallel}$ and $v_O^{\perp}$ at the other end of the strand. For endpoints moving only in the perpendicular direction, the strand is not sliding but just wrapping on and off the surface.

Let P be an arbitrary point on the wrapped centerline of the muscle between A and B. Then Q_P describes the corresponding contact point between strand and surface whose arc coordinate is given by u_P. Based on the description of the ellipse from the previous chapter, a corresponding natural surface coordinate σ_P can also be used here to describe the position $\underline{x}_{QP}$ of Q_P. Again, $\mathrm{d}\varphi_P$ is an infinitesimal rotation increment of the surface normal when progressing on the surface by an infinitesimal arc increment $\mathrm{d}u$ while ρ_P is the radius of curvature. In the following, the basic relationships between these parameters will be clarified and terms for them will be introduced.

For the surface path increment, it holds

$$\mathrm{d}u_P = \left\| \frac{\partial \underline{x}_{QP}}{\partial \sigma} \right\| \mathrm{d}\sigma_P \ \widehat{=} \ \mathrm{J}_{u\sigma}\big|_P \, \mathrm{d}\sigma_P \tag{4.1}$$
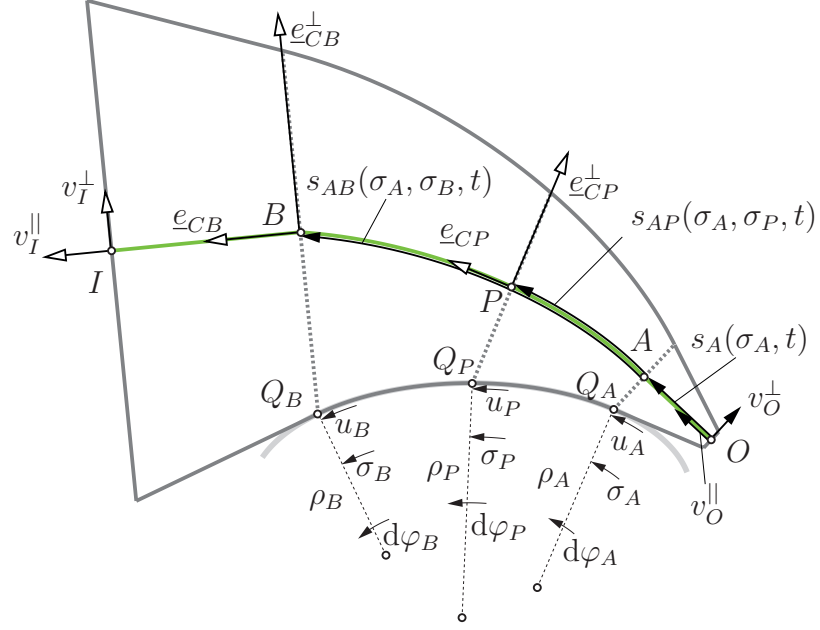
Figure 4.1: Free ends: Thick muscle wraps over surface between origin and insertion

and with it, the rotation increment of the surface normal can be expressed by

$$\mathrm{d}\varphi_P = \frac{\mathrm{d}u_P}{\rho_P} \;\; \widehat{=} \;\; \mathrm{J}_{\varphi\sigma}\big|_P \, \mathrm{d}\sigma_P \tag{4.2}$$

where $\mathrm{J}_{\varphi\sigma}\big|_P$ and $\mathrm{J}_{u\sigma}\big|_P$ denote the surface Jacobians evaluated at point Q_P.

During the motion of the endpoints O and I, the shape of the muscle changes: The middle segment can either wrap further on the surface (or respectively further wrap off the surface) without any sliding (as in the scenario where the endpoints move only in the perpendicular directions $v_O^\perp$ or $v_I^\perp$) or the strand can only slide on the surface with the contact points Q_A and Q_B (or equivalently σ_A and σ_B) remaining fixed.

As the strand can slide on the surface, the centerline path length s_P at point P is a function of the wrapping surface coordinate σ_P at a fixed time, and the change of strand location for fixed surface coordinate σ_A is a function of time (termed "pulling" according to increasing the value of s_A). An infinitesimal change $\mathrm{d}s_P$ of P is thus composed of two independent increments, denoted in shortcut as "wrap" and "pull":

$$\mathrm{d}s_P = \frac{\partial s}{\partial \sigma}\bigg|_{t=\mathrm{const}} \mathrm{d}\sigma_P + \frac{\partial s}{\partial t}\bigg|_{\sigma_P=\mathrm{const}} \mathrm{d}t \;\; \widehat{=} \;\; \mathrm{d}s^{\mathrm{wrap}} + \mathrm{d}s^{\mathrm{pull}} \;\; . \tag{4.3}$$

The same dependency holds for increments of half-angle α_P and half-thickness b_P:

$$\mathrm{d}\alpha_P = \left.\frac{\partial\alpha}{\partial\sigma}\right|_{t=\mathrm{const}} \mathrm{d}\sigma_P + \left.\frac{\partial\alpha}{\partial t}\right|_{\sigma_P=\mathrm{const}} \mathrm{d}t \;\; \widehat{=} \;\; \mathrm{d}\alpha^{\mathrm{wrap}} + \mathrm{d}\alpha^{\mathrm{pull}} \quad, \tag{4.4}$$

$$\mathrm{d}b_P = \left.\frac{\partial b}{\partial\sigma}\right|_{t=\mathrm{const}} \mathrm{d}\sigma_P + \left.\frac{\partial b}{\partial t}\right|_{\sigma_P=\mathrm{const}} \mathrm{d}t \;\; \widehat{=} \;\; \mathrm{d}b^{\mathrm{wrap}} + \mathrm{d}b^{\mathrm{pull}} \quad. \tag{4.5}$$

Using the chain rule, these can be led back to the path coordinate variations $\mathrm{d}s^{wrap}$ and $\mathrm{d}s^{pull}$ as

$$\mathrm{d}\alpha^{wrap} = \left.\frac{\partial\alpha}{\partial\sigma}\right|_{t=\mathrm{const}} \mathrm{d}\sigma_P = \left.\frac{\partial\alpha}{\partial s}\cdot\frac{\partial s}{\partial\sigma}\right|_{t=\mathrm{const}} \mathrm{d}\sigma_P \;\; \widehat{=} \;\; \mathrm{J}_{\alpha s}\,\mathrm{d}s^{wrap} \quad, \tag{4.6}$$

$$\mathrm{d}\alpha^{pull} = \left.\frac{\partial\alpha}{\partial t}\right|_{\sigma=\mathrm{const}} \mathrm{d}t = \left.\frac{\partial\alpha}{\partial s}\cdot\frac{\partial s}{\partial t}\right|_{\sigma=\mathrm{const}} \mathrm{d}t \;\; \widehat{=} \;\; \mathrm{J}_{\alpha s}\,\mathrm{d}s^{pull} \quad, \tag{4.7}$$

$$\mathrm{d}b^{wrap} = \left.\frac{\partial b}{\partial\sigma}\right|_{t=\mathrm{const}} \mathrm{d}\sigma_P = \left.\frac{\partial b}{\partial s}\cdot\frac{\partial s}{\partial\sigma}\right|_{t=\mathrm{const}} \mathrm{d}\sigma_P \;\; \widehat{=} \;\; \mathrm{J}_{bs}\,\mathrm{d}s^{wrap} \quad\text{and} \tag{4.8}$$

$$\mathrm{d}b^{pull} = \left.\frac{\partial b}{\partial t}\right|_{\sigma=\mathrm{const}} \mathrm{d}t = \left.\frac{\partial b}{\partial s}\cdot\frac{\partial s}{\partial t}\right|_{\sigma=\mathrm{const}} \mathrm{d}t \;\; \widehat{=} \;\; \mathrm{J}_{bs}\,\mathrm{d}s^{pull} \tag{4.9}$$

where J_{bs} and $\mathrm{J}_{\alpha s}$ are the Jacobians with respect to s as

$$\mathrm{J}_{bs} = \frac{\partial b}{\partial s} = \tan\alpha \qquad\text{and} \tag{4.10}$$

$$\mathrm{J}_{\alpha s} = \frac{\partial\alpha}{\partial s} = \frac{\partial^2 b}{\partial s^2}\frac{1}{1+\mathrm{J}_{bs}^2} \quad. \tag{4.11}$$

4.1   Kinematical equation for the infinitesimal increment of P

The increment $\mathrm{d}\underline{r}_P$ of point P can be described by the (linear) sum of the increment at the surface, the rotation of the segment $\overline{Q_P P}$, and the increment of the length of the segment $\overline{Q_P P}$ as

$$\mathrm{d}\underline{r}_P = \rho_P\,\underline{e}_{tP}\,\mathrm{d}\varphi_P + b_P\,(\mathrm{d}\varphi_P - \mathrm{d}\alpha_P)\,\underline{e}_{CP} + \mathrm{d}b_P\,\underline{e}_{CP}^{\perp} \tag{4.12}$$

like described in detail in Chapter **3.2.2** (see Eq. (3.20)) except for the extension that the variable conicity has to be considered in the second term that concerns the inclination of muscle's cross-section, with $\mathrm{d}\alpha_P$ acting in the opposite direction of $\mathrm{d}\varphi_P$ like illustrated in Fig. 4.2 for $\rho = \mathrm{const}$ and, thus, shortening the green arrow "2" in Fig. 3.7.
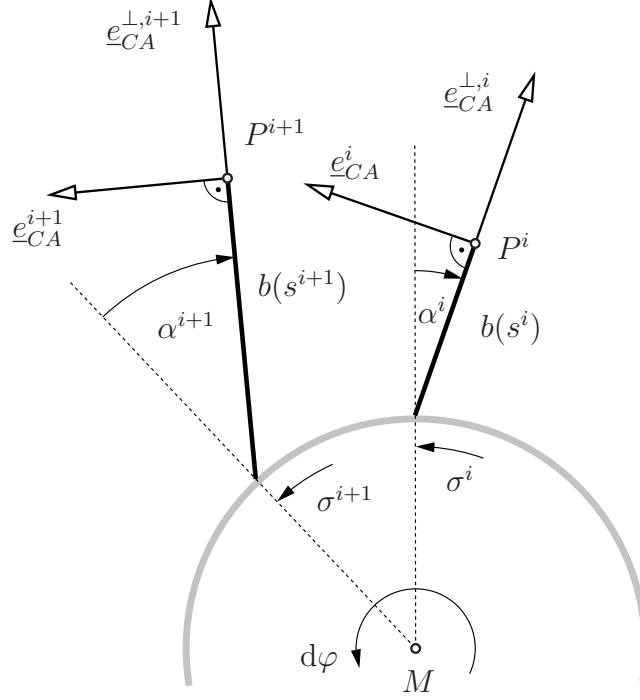
Figure 4.2: Change of the inclination of the cross-section due to $\mathrm{d}\alpha_P$ and $\mathrm{d}\varphi_P$

Inserting Eq. (4.2), Eq. (4.4) and Eq. (4.5) yields

$$
\begin{aligned}
\mathrm{d}\underline{r}_P = {} & \rho_P\, \underline{e}_{tP}\, \mathrm{J}_{\varphi\sigma}\big|_P\, \mathrm{d}\sigma_P \\
& + b_P\, \left[\mathrm{J}_{\varphi\sigma}\big|_P\, \mathrm{d}\sigma_P - \left(\mathrm{d}\alpha_P^{wrap} + \mathrm{d}\alpha_P^{pull} \right) \right]\, \underline{e}_{CP} \\
& + \left(\mathrm{d}b_P^{wrap} + \mathrm{d}b_P^{pull} \right)\, \underline{e}_{CP}^{\perp} \quad ,
\end{aligned}
\tag{4.13}
$$

which together with Eq. (4.6), Eq. (4.7), Eq. (4.8) and Eq. (4.9) leads to

$$
\begin{aligned}
\mathrm{d}\underline{r}_P = {} & \rho_P\, \underline{e}_{tP}\, \mathrm{J}_{\varphi\sigma}\big|_P\, \mathrm{d}\sigma_P \\
& + b_P\, \mathrm{J}_{\varphi\sigma}\big|_P\, \mathrm{d}\sigma_P\, \underline{e}_{CP} - b_P\, \mathrm{J}_{\alpha s}\big|_P\, \mathrm{d}s_P^{wrap}\, \underline{e}_{CP} - b_P\, \mathrm{J}_{\alpha s}\big|_P\, \mathrm{d}s_P^{pull}\, \underline{e}_{CP} \\
& + \mathrm{J}_{bs}\big|_P\, \mathrm{d}s_P^{wrap}\, \underline{e}_{CP}^{\perp} + \mathrm{J}_{bs}\big|_P\, \mathrm{d}s_P^{pull}\, \underline{e}_{CP}^{\perp} \quad .
\end{aligned}
\tag{4.14}
$$

By regrouping this equation with regard to the wrapping and the pulling components, one obtains

$$
\begin{aligned}
\mathrm{d}\underline{r}_P = {} & \left[\rho_P\, \mathrm{J}_{\varphi\sigma}\big|_P\, \mathrm{d}\sigma_P\, \underline{e}_{tP} + \left(b_P\, \mathrm{J}_{\varphi\sigma}\big|_P\, \mathrm{d}\sigma_P - b_P\, \mathrm{J}_{\alpha s}\big|_P\, \mathrm{d}s_P^{\mathrm{wrap}} \right)\, \underline{e}_{CP} + \mathrm{J}_{bs}\big|_P\, \mathrm{d}s_P^{\mathrm{wrap}}\, \underline{e}_{CP}^{\perp} \right] \\
& + \left[-b_P\, \mathrm{J}_{\alpha s}\big|_P\, \mathrm{d}s_P^{\mathrm{pull}}\, \underline{e}_{CP} + \mathrm{J}_{bs}\big|_P\, \mathrm{d}s_P^{\mathrm{pull}}\, \underline{e}_{CP}^{\perp} \right]
\end{aligned}
\tag{4.15}
$$

$$
= \frac{\partial \underline{r}_P}{\partial \sigma}\bigg|_{t=\mathrm{const}} \mathrm{d}\sigma_P + \frac{\partial \underline{r}_P}{\partial t}\bigg|_{\sigma_P=\mathrm{const}} \mathrm{d}t
\tag{4.16}
$$

$$
\hat{=}\ \mathrm{d}\underline{r}_P^{\mathrm{wrap}} + \mathrm{d}\underline{r}_P^{\mathrm{pull}} \quad ,
\tag{4.17}
$$

which also consists of a partial derivative with respect to the surface coordinate where t is held constant and a partial derivative with respect to t where the surface coordinate u (or σ) is held constant.

4.2 Wrapping path from A to B

Analogously to Section **3.2.2**, the wrapping path from A to B for fixed time ($\mathrm{d}t = 0$) is obtained by projecting Eq. (4.15) onto $\underline{e}_{CP}$. Thus, the kinematic condition Eq. (3.19) transferred to the new notation is

$$\left.\frac{\partial \underline{r}_P}{\partial \sigma}\right|_{t=const,P} \mathrm{d}\sigma_P \ \underline{e}_{CP} = \left.\frac{\partial s}{\partial \sigma}\right|_{t=const,P} \mathrm{d}\sigma_P \ \hat{=} \ \mathrm{d}s_P^{wrap} \ . \tag{4.18}$$

Together with Eq. (4.15) for $\mathrm{d}t = 0$ (see appendix A for summary of scalar products),

$$\begin{aligned}\mathrm{d}s_P^{wrap} &= \left[\rho_P \left.\mathrm{J}_{\varphi\sigma}\right|_P \mathrm{d}\sigma_P\right] \ \underline{e}_{tP} \cdot \underline{e}_{CP} \\ &+ \left[b_P \left.\mathrm{J}_{\varphi\sigma}\right|_P \mathrm{d}\sigma_P - b_P \left.\mathrm{J}_{\alpha s}\right|_P \mathrm{d}s_P^{wrap}\right] \ \underline{e}_{CP} \cdot \underline{e}_{CP}\end{aligned} \tag{4.19}$$

yields the differential equation for $\mathrm{d}s_P^{wrap}$

$$\mathrm{d}s_P^{wrap} = \frac{\rho_P \ \cos\alpha_P \left.\mathrm{J}_{\varphi\sigma}\right|_P + b_P \left.\mathrm{J}_{\varphi\sigma}\right|_P}{1 + b_P \left.\mathrm{J}_{\alpha s}\right|_P} \ \mathrm{d}\sigma_P \tag{4.20}$$

$$\hat{=} \ \left.\mathrm{J}_{s\sigma}\right|_P \ \mathrm{d}\sigma_P \tag{4.21}$$

where the Jacobian $\left.\mathrm{J}_{s\sigma}\right|_P$ is used in the following as a shortcut. This conforms to Eq. (3.22) in Chapter **3** except for the extension in the denominator taking into account the variable conicity. Letting $\sigma_P \equiv \sigma$, the wrap length from A to B can be computed by integrating this differential equation for the limits σ_A and σ_B

$$s_{AB} = \int_A^B \mathrm{d}s^{wrap} = \int_{\sigma_A}^{\sigma_B} \left.\frac{\partial s(\sigma,t)}{\partial \sigma}\right|_{t=const} \mathrm{d}\sigma = \int_{\sigma_A}^{\sigma_B} \left.\mathrm{J}_{s\sigma}(\sigma,t)\right|_{t=const} \mathrm{d}\sigma \ . \tag{4.22}$$

4.3 Velocity constraints at A and B

The constraints arise from the boundary conditions at points A and B and the condition of constant total length. At both endpoints, there are two boundary conditions: one in longitudinal and one in orthogonal direction. For simplicity reasons, the constraints are expressed in terms of velocities, which correspond to the infinitesimal expressions derived above divided by $\mathrm{d}t$.

4.3.1 Longitudinal constraint at point A

The length condition that the distance between the points O and A must correspond to the path length s_A results in the kinematic condition

$$(\underline{v}_A - \underline{v}_O) \cdot \underline{e}_{CA} = \dot{s}_A \; \mathrel{\hat{=}} \; \dot{s}_A^{\text{wrap}} + \dot{s}_A^{\text{pull}} \tag{4.23}$$

stating that the difference of velocities of points A and O projected on the cross-section normal must be equal to the total change of the path coordinate at point A. Together with $\underline{v}_A = \dfrac{\mathrm{d}\underline{r}_A}{\mathrm{d}t}$, Eq. (4.15) and Eq. (4.3) with $P \equiv A$, one obtains

$$\begin{aligned}
\frac{\mathrm{d}}{\mathrm{d}t} &\left\{ \rho_A \, \underline{e}_{tA} \, \mathrm{J}_{\varphi\sigma}\big|_A \, \mathrm{d}\sigma_A + \left[b_A \, \mathrm{J}_{\varphi\sigma}\big|_A \, \mathrm{d}\sigma_A - b_A \, \mathrm{J}_{\alpha s}\big|_A \, \mathrm{d}s_A^{\text{wrap}} \right] \underline{e}_{CA} \right. \\
&\left. + \mathrm{J}_{bs}\big|_A \, \mathrm{d}s_A^{\text{wrap}} \, \underline{e}_{CA}^{\perp} - b_A \, \mathrm{J}_{\alpha s}\big|_A \, \mathrm{d}s_A^{\text{pull}} \, \underline{e}_{CA} + \mathrm{J}_{bs}\big|_A \, \mathrm{d}s_A^{\text{pull}} \, \underline{e}_{CA}^{\perp} \right\} \cdot \underline{e}_{CA} \\
&- \underline{v}_O \cdot \underline{e}_{CA} \\
&= \frac{\mathrm{d}s_A^{\text{wrap}}}{\mathrm{d}t} + \frac{\mathrm{d}s_A^{\text{pull}}}{\mathrm{d}t} \quad .
\end{aligned} \tag{4.24}$$

Expanding this equation and eliminating equivalent terms by applying Eq. (4.20) yields

$$-b_A \, \mathrm{J}_{\alpha s}\big|_A \, \mathrm{d}s_A^{\text{pull}} - v_O^{\|} = \frac{\mathrm{d}s_A^{\text{pull}}}{\mathrm{d}t} \quad, \tag{4.25}$$

which leads to

$$\dot{s}_A^{\text{pull}} = \frac{-v_O^{\|}}{1 + b_A \, \mathrm{J}_{\alpha s}\big|_A} \quad . \tag{4.26}$$

4.3.2 Transversal direction at point A

The second condition that must be met at the contact point A between the wrapped and the straight strand segment is the orthogonality of the free centerline to the cross-section of the muscle in A, which is fulfilled if the following equation is true

$$(\underline{r}_A - \underline{r}_O) \cdot \underline{e}_{CA}^{\perp} = 0 \quad . \tag{4.27}$$

On velocity level, this leads to the kinematic condition

$$(\underline{v}_A - \underline{v}_O) \cdot \underline{e}_{CA}^{\perp} + (\underline{r}_A - \underline{r}_O) \cdot \underline{\dot{e}}_{CA}^{\perp} = 0 \tag{4.28}$$

where the inclination of $\underline{e}_{CA}^{\perp}$ changes due to the rotation $\dot{\varphi}_A$ about the center of curvature and the change $\dot{\alpha}_A$ of the cone half-angle as

$$\underline{\dot{e}}_{CA}^{\perp} = (\dot{\varphi}_A - \dot{\alpha}_A) \, \underline{e}_{CA} \quad . \tag{4.29}$$

Together with Eq. (4.2), Eq. (4.6) and Eq. (4.7) this results in

$$\underline{\dot{e}}_{CA}^{\perp} = \left[\mathrm{J}_{\varphi\sigma}\big|_A \, \dot{\sigma}_A - \mathrm{J}_{\alpha s}\big|_A \, \dot{s}_A^{wrap} - \mathrm{J}_{\alpha s}\big|_A \, \dot{s}_A^{pull} \right] \underline{e}_{CA} \quad . \tag{4.30}$$

Inserting Eq. (4.30), Eq. (4.15) and $s_A = \|\underline{r}_A - \underline{r}_O\|$ in Eq. (4.28) and solving for $\dot{\sigma}_A$ yields

$$\dot{\sigma}_A = \frac{v_O^{\perp} - \left(\mathrm{J}_{bs}\big|_A - s_A \mathrm{J}_{\alpha s}\big|_A \right) \dot{s}_A^{pull}}{\mathrm{J}_{bs}\big|_A \mathrm{J}_{s\sigma}\big|_A + s_A \left(\mathrm{J}_{\varphi\sigma}\big|_A - \mathrm{J}_{\alpha s}\big|_A \mathrm{J}_{s\sigma}\big|_A \right) - \rho_A \mathrm{J}_{\varphi\sigma}\big|_A \sin\alpha_A} \quad . \tag{4.31}$$

Using this result in Eq. (4.20) with $P \equiv A$ immediately leads to $\dot{s}_A^{wrap}$.

4.3.3 Longitudinal direction at point B

The constraint defining the longitudinal direction at point B arises from the condition that the overall length of the strand must be constant, which is given by the equation

$$s_A + s_{AB} + s_{BI} = \ell = const \tag{4.32}$$

with the corresponding time derivative

$$\dot{s}_A + \dot{s}_{AB} + \dot{s}_{BI} = 0 \quad . \tag{4.33}$$

The length change at A results from Eq. (4.3) as

$$\dot{s}_A = \dot{s}_A^{wrap} + \dot{s}_A^{pull} \quad . \tag{4.34}$$

For the length change $\dot{s}_{AB}$, the partial derivative of the length s_{AB} that is already derived in Eq. (4.22) as

$$s_{AB} = s_{AB} \left(\sigma_A, \sigma_B, t \right) = \int_{\sigma_A}^{\sigma_B} \left. \frac{\partial s(\sigma, t)}{\partial \sigma} \right|_{t=const} d\sigma \tag{4.35}$$

leads to

$$ds_{AB} = \left. \frac{\partial s_{AB}}{\partial \sigma_A} \right|_{\sigma_B,t=const} d\sigma_A + \left. \frac{\partial s_{AB}}{\partial \sigma_B} \right|_{\sigma_A,t=const} d\sigma_B + \left. \frac{\partial s_{AB}}{\partial t} \right|_{\sigma_A,\sigma_B=const} dt \quad . \tag{4.36}$$

Hence, on velocity level one obtains

$$\dot{s}_{AB} = \left. \frac{\partial s_{AB}}{\partial \sigma_A} \right|_{\sigma_B,t=const} \dot{\sigma}_A + \left. \frac{\partial s_{AB}}{\partial \sigma_B} \right|_{\sigma_A,t=const} \dot{\sigma}_B + \left. \frac{\partial s_{AB}}{\partial t} \right|_{\sigma_A,\sigma_B=const} \tag{4.37}$$

with

$$
\begin{aligned}
\left.\frac{\partial s_{AB}}{\partial \sigma_A}\right|_{\sigma_B, t=const} \dot{\sigma}_A &= \left.\frac{\partial}{\partial \sigma_A}\right|_{\sigma_B, t=const} \left\{ \int_{\sigma_A}^{\sigma_B} \left.\frac{\partial s(\sigma, t)}{\partial \sigma}\right|_{t=const} \mathrm{d}\sigma \right\} \dot{\sigma}_A \\
&= -\left.\frac{\partial s}{\partial \sigma}\right|_{t=const,A} \dot{\sigma}_A \\
&= -\dot{s}_A^{wrap} \quad,
\end{aligned}
\tag{4.38}
$$

$$
\begin{aligned}
\left.\frac{\partial s_{AB}}{\partial \sigma_B}\right|_{\sigma_A, t=const} \dot{\sigma}_B &= \left.\frac{\partial}{\partial \sigma_B}\right|_{\sigma_A, t=const} \left\{ \int_{\sigma_A}^{\sigma_B} \left.\frac{\partial s(\sigma, t)}{\partial \sigma}\right|_{t=const} \mathrm{d}\sigma \right\} \dot{\sigma}_B \\
&= \left.\frac{\partial s}{\partial \sigma}\right|_{t=const,B} \dot{\sigma}_B \\
&= \dot{s}_B^{wrap}
\end{aligned}
\tag{4.39}
$$

and

$$
\begin{aligned}
\left.\frac{\partial s_{AB}}{\partial t}\right|_{\sigma_A, \sigma_B=const} &= \left.\frac{\partial s_B}{\partial t}\right|_{\sigma_A, \sigma_B=const} - \left.\frac{\partial s_A}{\partial t}\right|_{\sigma_A, \sigma_B=const} \\
&= \dot{s}_B^{pull} - \dot{s}_A^{pull} \quad.
\end{aligned}
\tag{4.40}
$$

Inserting $\dot{s}_A$ and $\dot{s}_{AB}$ into Eq. (4.33) yields for the length change $\dot{s}_{BI}$

$$
\begin{aligned}
\dot{s}_{BI} &= -\left(\dot{s}_A^{wrap} + \dot{s}_A^{pull} \right) - \left(\dot{s}_B^{wrap} - \dot{s}_A^{wrap} + \dot{s}_B^{pull} - \dot{s}_A^{pull} \right) \\
\Leftrightarrow \dot{s}_{BI} &= -\dot{s}_B^{wrap} - \dot{s}_B^{pull} \quad.
\end{aligned}
\tag{4.41}
$$

This has to be equivalent to the velocity difference of the points B and I in direction of $\underline{e}_{CB}$, leading to the equation:

$$
(\underline{v}_I - \underline{v}_B) \cdot \underline{e}_{CB} = \dot{s}_{BI} \quad.
\tag{4.42}
$$

Applying Eq. (4.15) for $P \equiv B$ and Eq. (4.41) results in

$$
\begin{aligned}
\underline{v}_I \, \underline{e}_{CB} - &\left\{ \rho_B \, \underline{e}_{tB} \, \mathrm{J}_{\varphi\sigma}\big|_B \, \dot{\sigma}_B + \left[b_B \, \mathrm{J}_{\varphi\sigma}\big|_B \, \dot{\sigma}_B - b_B \, \mathrm{J}_{\alpha s}\big|_B \dot{s}_B^{wrap} \right] \underline{e}_{CB} \right. \\
&\left. + \mathrm{J}_{bs}\big|_B \dot{s}_B^{wrap} \underline{e}_{CB}^{\perp} - b_B \, \mathrm{J}_{\alpha s}\big|_B \dot{s}_B^{pull} + \mathrm{J}_{bs}\big|_B \dot{s}_B^{pull} \underline{e}_{CB}^{\perp} \right\} \cdot \underline{e}_{CB} \\
&= -\dot{s}_B^{wrap} - \dot{s}_B^{pull} \quad.
\end{aligned}
\tag{4.43}
$$

Using Eq. (4.20), equivalent terms can be eliminated and the simplified equation is

$$
\Rightarrow v_I^{\parallel} = -\left[1 + b_B \, \mathrm{J}_{\alpha s}\big|_B \right] \dot{s}_B^{pull} \quad.
\tag{4.44}
$$

On the other hand, $\dot{s}_B^{pull}$ is related to $\dot{s}_A^{pull}$ by the velocity transmission along the wrapped centerline between A and B. Hence, the velocity transmission factor $\hat{\kappa}_{AB}$ is introduced as

$$\hat{\kappa}_{AB} = \frac{\dot{s}_B^{\text{pull}}}{\dot{s}_A^{\text{pull}}} = \frac{(\rho_B \ \cos\alpha_B + b_B)\rho_A}{(\rho_A \ \cos\alpha_A + b_A)\rho_B} \ e^\kappa \tag{4.45}$$

where e^κ is the quotient of output to input velocity on surface level defined by Eq. (3.53) between A and B

$$e^\kappa = \frac{\dot{u}_B}{\dot{u}_A} = \exp\left(\int_{\sigma_A}^{\sigma_B} \frac{r(s(\sigma))}{\rho(\sigma)\,[\,\rho(\sigma) + r(s(\sigma))\,]} \frac{\mathrm{d}\rho}{\mathrm{d}\sigma} \, \mathrm{d}\sigma\right) \quad . \tag{4.46}$$

Thus, it holds for $\dot{s}_B^{pull}$

$$\dot{s}_B^{pull} = \hat{\kappa}_{AB} \ \dot{s}_A^{pull} = -\hat{\kappa}_{AB} \ \frac{v_O^{\|}}{1 + b_A \ \mathrm{J}_{\alpha s}\big|_A} \tag{4.47}$$

and a global longitudinal input-output velocity transmission is obtained as

$$v_I^{\|} = \hat{\kappa}_{AB} \ \frac{1 + b_B \ \mathrm{J}_{\alpha s}\big|_B}{1 + b_A \ \mathrm{J}_{\alpha s}\big|_A} \ v_O^{\|} \quad . \tag{4.48}$$

4.3.4 Transversal direction at point B

Analogously to the transversal direction at point A in Section **4.3.2**, the transversal direction at point B is defined by the orthogonality condition

$$(\underline{r}_I - \underline{r}_B) \cdot \underline{e}_{CB}^{\perp} = 0 \tag{4.49}$$

expressing that the free line-segment at B must be perpendicular to the strand cross-section in B, resulting in the kinematic condition

$$(\underline{v}_I - \underline{v}_B) \cdot \underline{e}_{CB}^{\perp} + (\underline{r}_I - \underline{r}_B) \cdot \underline{\dot{e}}_{CB}^{\perp} = 0 \quad . \tag{4.50}$$

Analogously to Section **4.3.2**, this yields for $\dot{\sigma}_B$ the expression

$$\dot{\sigma}_B = -\frac{v_I^{\perp} - \left(b_B' + \ell_{BI} \ \mathrm{J}_{\alpha s}\big|_B\right) \dot{s}_B^{pull}}{-b_B' \mathrm{J}_{s\sigma}\big|_B + \ell_{BI} \left[\mathrm{J}_{\varphi\sigma}\big|_B - \mathrm{J}_{\alpha s}\big|_B \ \mathrm{J}_{s\sigma}\big|_B\right] + \rho_B \ \mathrm{J}_{\varphi\sigma}\big|_B \ \sin\alpha_B} \quad . \tag{4.51}$$

4.3.5 Geometric interpretation of "pulling" at the muscle's free end

Fig. 4.3 illustrates the geometric interpretation of Eq. (4.26), from where it follows

$$-v_O^{\|}\mathrm{d}t = \left(1 + b_A \ \mathrm{J}_{\alpha s}\big|_A\right) \mathrm{d}s_A^{\text{pull}} \quad . \tag{4.52}$$

The figure shows the surface and the boundary cross-section of the continuous strand at the surface end-contact point A for the two points in time t (upper figure) and $t+\mathrm{d}t$ (lower figure). The surface coordinate σ_A is held constant between them, i.e., the same contact point is regarded in both points of time. At time step t, the boundary cross-section (called "old" face and represented by the dotted line) is inclined by the half-angle $\alpha(s_A)$. Pulling at the strand's right end O by $-v_O^{\|}\mathrm{d}t$ brings the "new" face with the inclination $\alpha(s_A+\mathrm{d}s_A^{\text{pull}})$ to σ_A at the time step $t+\mathrm{d}t$. According to Eq. (4.52), $-v_O^{\|}\mathrm{d}t$ is the sum of the change $\mathrm{d}s_A^{\text{pull}}$ (*ii*) of the midline path coordinate from $A(t)$ to $A(t+\mathrm{d}t)$ and the arc length of the circle with radius b_A and half-angle $\mathrm{J}_{\alpha s}\mathrm{d}s_A^{\text{pull}}$ (*i*). This length is the same as the length of the path from $A(t)$ to $A^*(t)$ at $\sigma_A+\mathrm{d}\sigma_A$ at the same half-angle $\alpha(s_A)$ as it holds

$$-v_O^{\|}\mathrm{d}t = (\rho_A \cos\alpha_A + b_A)\,\mathrm{J}_{\varphi\sigma}\mathrm{d}\sigma_A \quad. \tag{4.53}$$

Figure 4.3: Equation $\left(1 + b_A \, J_{\alpha s}\big|_A\right) ds_A^{\text{pull}} = -v_O^{\parallel} dt = \left(\rho_A \cos\alpha_A + b_A\right) J_{\varphi\sigma} d\sigma_A$ geometrically interpreted
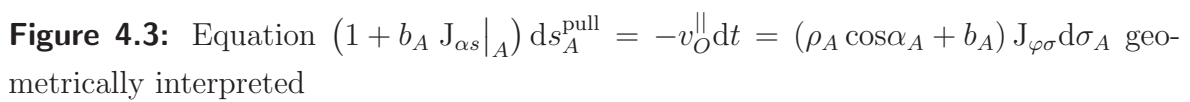
4.4   Discrete bead chain method

For comparison, a discrete bead chain method is implemented where beads are fitted into the muscle's geometry having the constant distance $\Delta\bar{s}$ to each other. As derived in Chapter **3**, the continuous method can be seen as the limit case of the bead method for $\Delta\bar{s}$ becoming infinitesimally small. Analogous to the continuous strand, between the endpoints called O and I, the bead chain is wrapped over an arbitrary surface for which the contact curve is an ellipse in the example presented in Fig. 4.4. Here, too, one can distinguish between a wrapped part of the strand in the middle of the chain where the beads are in contact with the surface and two adjacent straight chain segments on both ends where the beads are lined-up on a straight line from the last bead in contact (LCA or LCB) to the corresponding endpoint (O or I). It is assumed, that the current state of the beads, meaning the number of the first and the last bead in contact, as well as the position of the beads given by the surface coordinate σ is known at the beginning. For a defined movement of the endpoints, first the displacement of the bead chain is computed using the known state of beads in contact. Secondly, the status of the beads in contact must be checked for the new configuration and corrected if necessary.

Here, two cases might occur:

(1) A bead that was in contact before must now lift off, and
(2) a bead that was free before is now getting into contact with the surface.
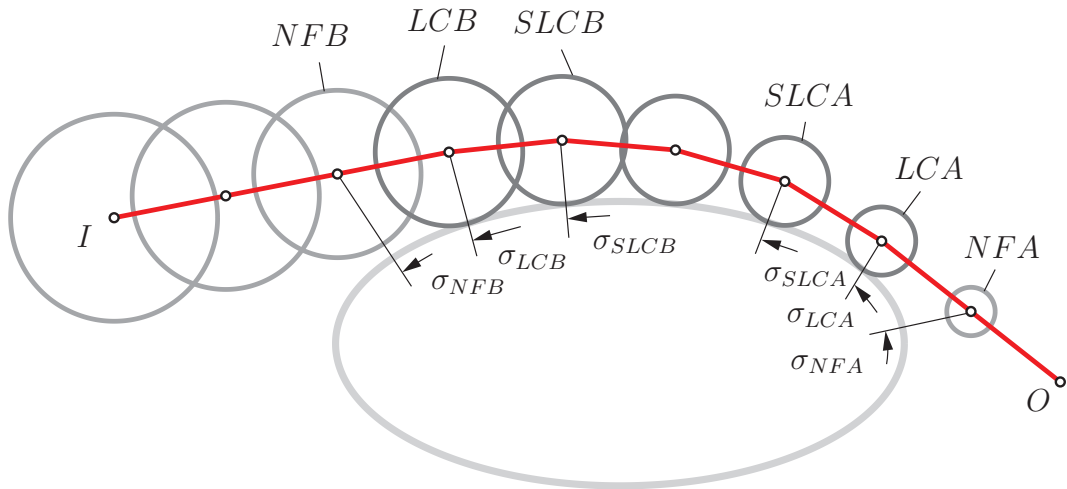
Figure 4.4: Free ends: Thick bead strand wraps over surface between origin and insertion
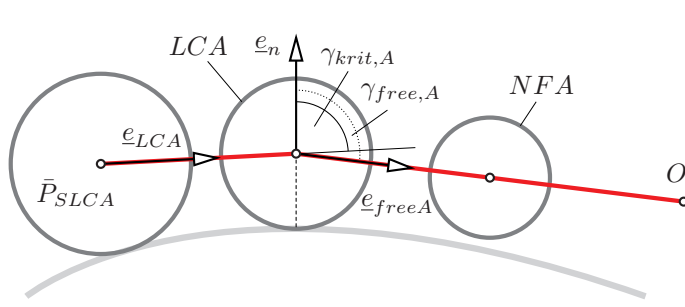
Figure 4.5: Condition for lift-off   **Figure 4.6:** Condition for touchdown
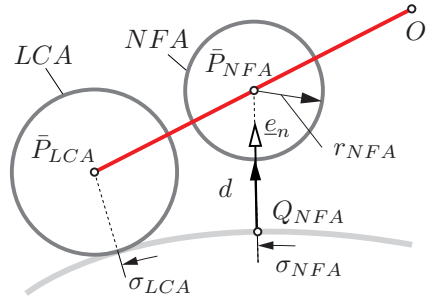
The condition for the lift-off at the right end A is illustrated in Fig. 4.5. The unit vector $\underline{e}_{LCA}$ in direction of the center of the second-last connected bead ($SLCA$) to the center of the last connected bead (LCA) is computed as

$$\underline{e}_{LCA} = \frac{\underline{r}_{\bar{P}_{LCA}} - \underline{r}_{\bar{P}_{SLCA}}}{\left\| \underline{r}_{\bar{P}_{LCA}} - \underline{r}_{\bar{P}_{SLCA}} \right\|} \tag{4.54}$$

while it holds for the unit vector from the center $\bar{P}_{LCA}$ in direction of the free line

$$\underline{e}_{freeA} = \frac{\underline{r}_{\bar{P}_{NFA}} - \underline{r}_{\bar{P}_{LCA}}}{\left\| \underline{r}_{\bar{P}_{NFA}} - \underline{r}_{\bar{P}_{LCA}} \right\|} \quad . \tag{4.55}$$

The angle between the surface normal $\underline{e}_n$ at bead LCA and $\underline{e}_{LCA}$ is called $\gamma_{krit,A}$, while $\gamma_{free,A}$ is the angle between the surface normal and $\underline{e}_{freeA}$. Lift-off of bead LCA takes place if it holds $\gamma_{free,A} - \gamma_{krit,A} < 0$.

For testing the touchdown of the next free bead at A (NFA), see Fig. 4.6, the shadow coordinate σ_{NFA} has to be determined by solving

$$\Delta \underline{r}_{Q_{NFA} \bar{P}_{NFA}}(\sigma_{NFA}) \cdot \underline{e}_t(\sigma_{NFA}) = 0 \quad . \tag{4.56}$$

Then the bead NFA gets in contact for $d = \left\| \Delta \underline{r}_{Q_{NFA} \bar{P}_{NFA}} \right\| - r_{NFA} < 0$ with r_{NFA} being the radius of the free bead.

4.5 Comparison

The continuous solution was obtained by numerical integration of Eq. (4.26), Eq. (4.31), Eq. (4.48), and Eq. (4.51) using the Matlab Runge-Kutta routine ode45 with the relative tolerance reltol$= 10^{-6}$. Alternatively, a Newton solver can be regarded using the corresponding four position constraints as zero functions and the velocity transmission for associated Jacobian evaluation. For each evaluation of the differential equations at a new point, an inner integration over s_{AB} according to Eq. (4.22) as well as that of

the input-output velocity transmission factor e^κ according to Eq. (3.53) is necessary, which were again carried out using ode45 and the precision of the outer integration.

The regarded example is a stretch of thick muscle strand wrapped on an ellipse with semi-major axis $a_1 = 1$ and semi-minor axis $a_2 = 0.5$ with dimensionless coordinates. Two cases of thick strands are regarded: One with a constant half-angle α (termed "constant conicity"), and one with a parabolic change of strand thickness over strand length as illustrated in Fig. 4.7 a) and Fig. 4.8 a). The dotted lines represent the corresponding boundary cross-sections of the continuous strand at the surface end-contact points A and B. The end O is moving on a circle of radius $r = 0.4$ with constant angular velocity $\Omega = 1°/\mathrm{s}$, while the end I can slide in horizontal direction. This resembles a slider-crank mechanism with the thick muscle acting as a "coupler" and the crank angle acting as input, while the slider motion x_I is the dependent variable. For the numerical integration, the relative maximum error in all constraints lay below 10^{-6}, showing good convergence and precision.

a) Configuration

b) Diff. x_I continuous$-$discrete

c) Kinematics of x_I: discrete ($n = 9$, colored) vs. continuous (dashed black)

d) Comparison

n	Δx_I	CPU d/c
9	0.0037	252
18	0.0009	417
36	0.0003	988
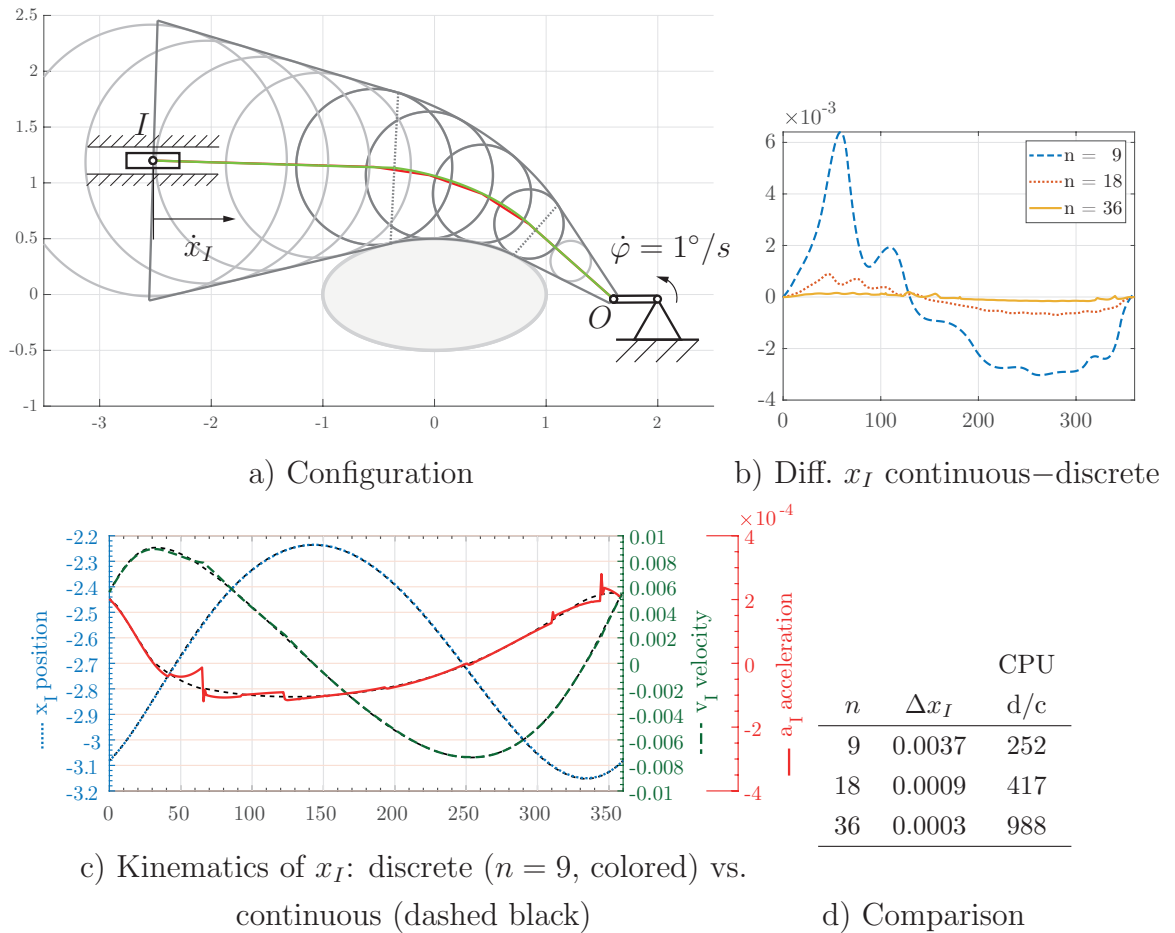
Figure 4.7: Thick muscle with constant half-angle α

For comparison purposes, the continuous muscle was also approximated by a chain of inscribed circles ("beads") with equidistant centers in a way that the continuous muscle becomes their hull. The "fineness" of the discretization is described by the number of beads N within the total stretch of the continuous muscle. The contact between the circles and the ellipse was solved by Newton iterations using the Matlab solver fsolve with constant rotation increments of $1°$ at the crank. If a bead entered or left the contact with the ellipse at a step, the corresponding bead location was corrected, i.e., no interval nesting was performed to determine the exact crank angle value at which touch-down or lift-off occurs.

The initial configuration was chosen so that points O and I exactly match for both methods. Accordingly, the length of the bead method varies depending on the number of beads. Additionally, at the beginning of the motion, the position of the first and the last bead in contact with the surface is exactly the same as the beginning and the end of the continuously wrapped strand. Figs. 4.7 and 4.8 show the corresponding configu-

a) Configuration

b) Diff. x_I continuous$-$discrete

c) Kinematics of x_I: discrete ($n = 9$, colored) vs. continuous (dashed black)

n	Δx_I	CPU d/c
9	0.0040	239
18	0.0007	461
36	0.0001	887

d) Comparison
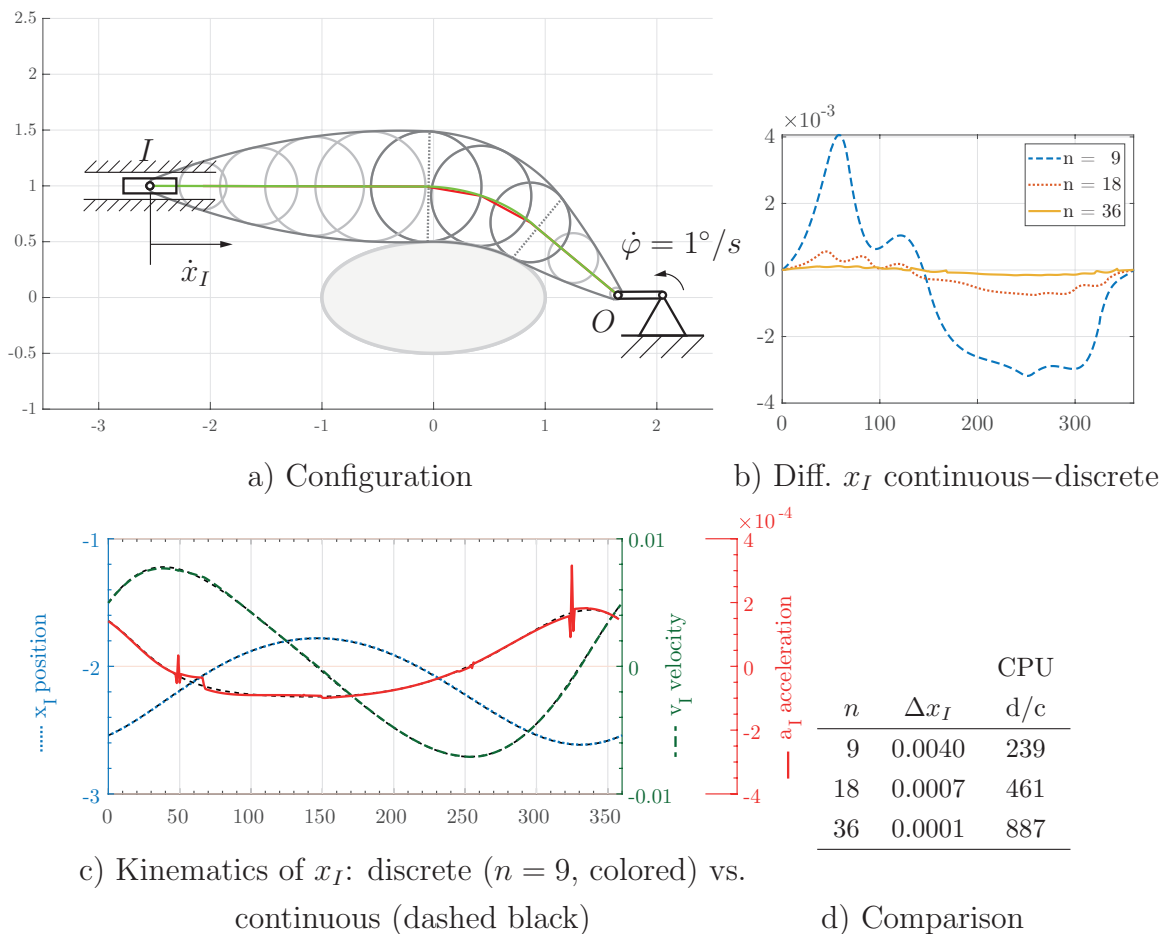
Figure 4.8: Thick muscle with non-constant half-angle α

rations (a) and the results (b) of the difference of the computed value for the dependent slider variable x_I between the continuous method and the bead discretization for three different degrees of resolution. It can be seen that the continuous method approaches the bead case for finer discretizations, proving its consistency. Moreover, it can also be seen that the discretized approach leads to unrealistic "pulsating" motions, with frequency and amplitude inversely proportional to the bead pair distance. In figure (c), position, velocity and acceleration of point I are plotted for the case of $n = 9$ beads (colored curves) and compared to the smooth curves of the continuous method (dashed thin black lines). While the position graph seems smooth, the acceleration graph shows a jerky behavior including "spikes" due to sudden bead contact. This is disadvantageous for applications where the strand force is a function of strand length and strand length rate of change such as e.g. in the Hill muscle model, as then the force will the vary correspondingly discontinuously, slowing down numerical integration schemes. In the table (d), the maximal difference between displacement x_I of the discrete and the continuous method as well as the relative CPU time as factor discrete/continuous ("CPU d/c") are shown for a sample of discretization fineness ("N"). Visibly, the continuous approach leads to a much faster, more precise, and more easily implementable approach.

5 Wrapping with elongation and compressible cross-sections

In this chapter the method is extended to cover elongation with compressible cross-sections instead of the constant length condition. Hereby, the extension is evolved in three successive steps, starting with the simplest case of a conical muscle with a constant change in the cross-section ($\alpha = $ const) along the length coordinate wrapping on a surface with constant curvature radius. In the second step, the circular surface curve is replaced by an ellipse where the curvature radius is non-constant. Last, variable conicity ($\alpha \neq $ const) of the muscle is considered. In all three cases, the point O is held fixed, which is generalized to the moving point O in Chapter **6**.

5.1 Case 1: Stretching cone on circle

The basic idea is illustrated for a cone-shaped muscle in Fig. 5.1 showing the original muscle at the top with the unstretched length ℓ_0. Below, the muscle is stretched by $\Delta\ell$. Accordingly, the longitudinal strain is $\varepsilon = \Delta\ell/\ell_0$. To simplify the derivation, it is assumed here that the thickness b_0 at the end of the muscle remains constant during the elongation process. Thus, the half-angle α of the cone depends on ε, as it holds

$$\tan\alpha_0 = \frac{b_0}{\ell_0} \tag{5.1}$$

for the unstretched cone and

$$\tan\alpha(\varepsilon) = \frac{b_0}{\ell_0\,(1+\varepsilon)} = \frac{\tan\alpha_0}{1+\varepsilon} \tag{5.2}$$

for the stretched cone.

Let the cone-shaped muscle be wrapped over the circular surface curve with constant curvature radius ρ, as illustrated in Fig. 5.2, with free end O fixed and free end I moving like a prismatic joint in direction of $\underline{u}_I$ with the joint variable s_I. Between the contact points Q_A and Q_B, the muscle wraps around the surface with φ_A and φ_B being the corresponding surface variables, whereas A and B are the corresponding points on the centerline of the muscle marking the transition from the straight line segment to the wrapped segment of the centerline and vice versa. The length of the straight line segments of the centerline between O and A as well as B and I are measured by s_{OA} and s_{BI}, respectively. The wrapped part of the centerline between A and B is denoted
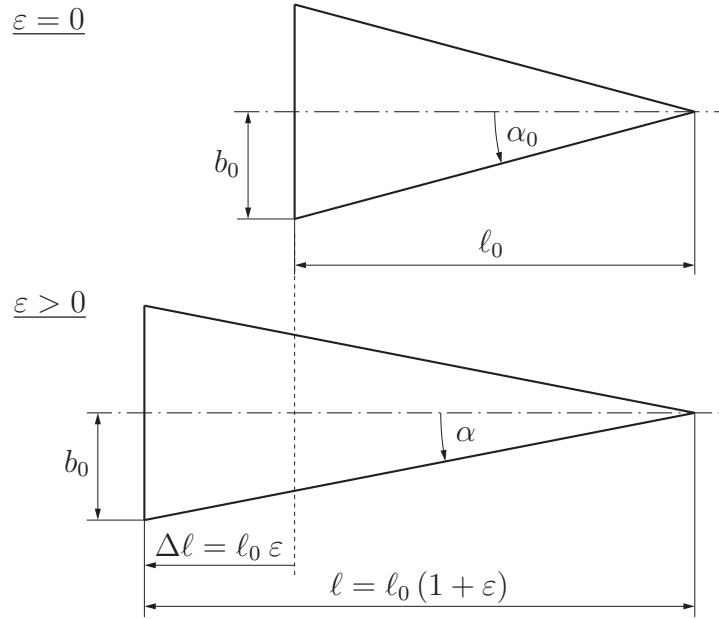
Figure 5.1: Stretched muscle: Basic idea

s_{AB}. Summed up, they correspond to the overall muscle length

$$\ell = s_{OA} + s_{AB} + s_{BI} \quad . \tag{5.3}$$

The muscle half-thickness b_A and b_B at A and B, respectively, depends on the length of the centerline in these points. Thus, for a cone, it holds

$$b_A = \tan\alpha \; s_{OA} \quad \text{and} \tag{5.4}$$

$$b_B = \tan\alpha \; s_{OB} \tag{5.5}$$

with $s_{OB} = s_{OA} + s_{AB}$, where s_{AB} is obtained by integrating Eq. (3.22) over φ

$$s_{AB} = \int_{\varphi_A}^{\varphi_B} \left[\rho \; \cos\alpha + b \right] \; \mathrm{d}\varphi \quad . \tag{5.6}$$

5.1.1 Boundary constraints at A and B

As already presented in Chapter **4**, at points A and B, there are two boundary conditions each, one in the longitudinal and one in the transverse direction. At A, the longitudinal condition says that s_{OA} has to correspond to the distance between the points O and A

$$g_{1A} = s_{OA} - \Delta\underline{r}_{OA} \cdot \underline{e}_{CA} = 0 \tag{5.7}$$
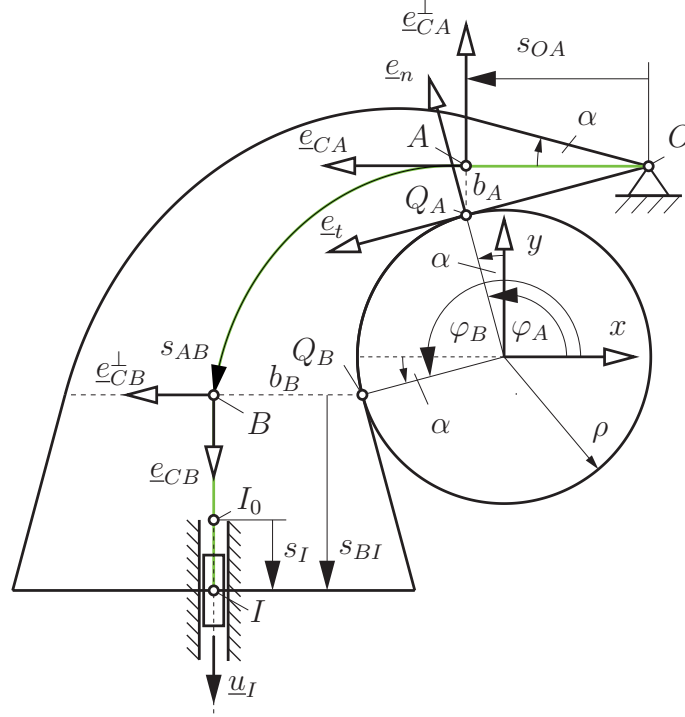
Figure 5.2: Case 1: Cone stretching over circle

with $\Delta \underline{r}_{OA} = \underline{r}_A - \underline{r}_O$ and $\underline{r}_A = \rho \, \underline{e}_n^A + b_A \, \underline{e}_{CA}^\perp$, whereas the orthogonal constraint stipulates that the free end $\Delta \underline{r}_{OA} = \underline{r}_A - \underline{r}_O$ has to be orthogonal to the muscle's cross-section at A (and therefore orthogonal to $\underline{e}_{CA}^\perp$)

$$g_{2A} = \Delta \underline{r}_{OA} \cdot \underline{e}_{CA}^\perp = 0 \quad . \tag{5.8}$$

Expanded, the following constraint equations result

$$g_{1A} = \qquad s_{OA} - \rho \, \sin\alpha(\varepsilon) + \underline{r}_O \cdot \underline{e}_C(\varphi_A, \varepsilon) = 0 \tag{5.9}$$

$$g_{2A} = \tan\alpha(\varepsilon) \, s_{OA} + \rho \, \cos\alpha(\varepsilon) - \underline{r}_O \cdot \underline{e}_C^\perp(\varphi_A, \varepsilon) = 0 \quad . \tag{5.10}$$

At B, the longitudinal constraint corresponds to

$$g_{1B} = s_{OB} + s_{BI} - \ell(\varepsilon) = 0 \tag{5.11}$$

which contains the condition that the overall length ℓ depending on the longitudinal strain ε has to equal the sum of the centerline segments with

$$s_{OB} = s_{OA} + s_{AB} \quad , \tag{5.12}$$

$$s_{BI} = \Delta \underline{r}_{BI} \cdot \underline{e}_{CB} = [\underline{r}_I - \underline{r}_B] \cdot \underline{e}_{CB} \quad , \tag{5.13}$$

$$\underline{r}_I = \underline{r}_{I,0} + \underline{u}_I \, s_I \quad \text{and} \tag{5.14}$$

$$\underline{r}_B = \rho \, \underline{e}_n^B + b_B \, \underline{e}_{CB}^\perp \quad . \tag{5.15}$$

The second condition at B specifies that, again, the free end $\Delta \underline{r}_{BI}$ at I is orthogonal to the cross-sectional area at B, resulting in

$$g_{2B} = \Delta \underline{r}_{BI} \cdot \underline{e}_{CB}^{\perp} = 0 \quad . \tag{5.16}$$

Expanded, this leads to the following constraint equations at B

$$g_{1B} = \underline{r}_I \cdot \underline{e}_C(\varphi_B, \varepsilon) - \rho \, \sin\alpha(\varepsilon) + \qquad s_{OB}(\varepsilon) - \ell(\varepsilon) = 0 \tag{5.17}$$

$$g_{2B} = \underline{r}_I \cdot \underline{e}_C^{\perp}(\varphi_B, \varepsilon) - \rho \, \cos\alpha(\varepsilon) - \tan\alpha(\varepsilon) \, s_{OB}(\varepsilon) \qquad = 0 \quad . \tag{5.18}$$

Defining the state vectors $\underline{z}_A$ at point A and $\underline{z}_B$ at point B as

$$\underline{z}_A = \begin{bmatrix} s_{OA} \\ \varphi_A \end{bmatrix} \quad \text{and} \quad \underline{z}_B = \begin{bmatrix} s_I \\ \varphi_B \end{bmatrix} \tag{5.19}$$

it is straightforward to obtain the Jacobians $\mathrm{J}_A := \partial \underline{g}_A / \partial \underline{z}_A$ and $\mathrm{J}_B := \partial \underline{g}_B / \partial \underline{z}_B$ as

$$\mathrm{J}_A = \frac{\partial \underline{g}_A}{\partial \underline{z}_A} = \begin{bmatrix} 1 & -\underline{r}_O \cdot \underline{e}_{CA}^{\perp} \\ \tan\alpha & -\underline{r}_O \cdot \underline{e}_{CA} \end{bmatrix} \tag{5.20}$$

and

$$\mathrm{J}_B = \frac{\partial \underline{g}_B}{\partial \underline{z}_B} = \begin{bmatrix} \underline{u}_I \cdot \underline{e}_{CB} & -\underline{r}_I \cdot \underline{e}_{CB}^{\perp} + \dfrac{\partial s_{OB}}{\partial \varphi_B} \\[2mm] \underline{u}_I \cdot \underline{e}_{CB}^{\perp} & \underline{r}_I \cdot \underline{e}_{CB} - \tan\alpha \dfrac{\partial s_{OB}}{\partial \varphi_B} \end{bmatrix} \tag{5.21}$$

with

$$\frac{\partial s_{OB}}{\partial \varphi_B} = \rho \, \cos\alpha_B + b_B \tag{5.22}$$

to formulate the implicit constraint at velocity level as

$$\dot{\underline{g}}_A = \mathrm{J}_A \, \dot{\underline{z}}_A + \frac{\partial \underline{g}_A}{\partial \varepsilon} \, \dot{\varepsilon} \overset{!}{=} 0 \qquad \text{and} \tag{5.23}$$

$$\dot{\underline{g}}_B = \mathrm{J}_B \, \dot{\underline{z}}_B + \frac{\partial \underline{g}_B}{\partial \varepsilon} \, \dot{\varepsilon} \overset{!}{=} 0 \quad . \tag{5.24}$$

5.1.2 Derivatives with respect to strain

For the case of a conical muscle geometry stretching on a circle, differentiating the constraints Eq. (5.9) and Eq. (5.10) at A as well as Eq. (5.17) and Eq. (5.18) at B with respect to the longitudinal strain ε leads to

$$\frac{\partial g_{1A}}{\partial \varepsilon} = \qquad\qquad -\rho \, \cos\alpha \, \frac{\partial \alpha}{\partial \varepsilon} + \underline{r}_O \cdot \underline{e}_C^{\perp} \, \frac{\partial \alpha}{\partial \varepsilon} \tag{5.25}$$

$$\frac{\partial g_{2A}}{\partial \varepsilon} = \frac{\partial \tan\alpha}{\partial \varepsilon} \, s_{OA} - \rho \, \sin\alpha \, \frac{\partial \alpha}{\partial \varepsilon} + \underline{r}_O \cdot \underline{e}_C \, \frac{\partial \alpha}{\partial \varepsilon} \tag{5.26}$$

and

$$\frac{\partial g_{1B}}{\partial \varepsilon} = \quad \underline{r}_I \cdot \underline{e}_C^{\perp} \frac{\partial \alpha}{\partial \varepsilon} - \rho \, \cos\alpha \, \frac{\partial \alpha}{\partial \varepsilon} + \qquad \frac{\partial s_{OB}}{\partial \varepsilon} - \ell_0 \tag{5.27}$$

$$\frac{\partial g_{2B}}{\partial \varepsilon} = -\underline{r}_I \cdot \underline{e}_C \frac{\partial \alpha}{\partial \varepsilon} + \rho \, \sin\alpha \, \frac{\partial \alpha}{\partial \varepsilon} - \tan\alpha \frac{\partial s_{OB}}{\partial \varepsilon} - \frac{\partial \tan\alpha}{\partial \varepsilon} s_{OB} \tag{5.28}$$

where the derivatives of the muscle parameter α with respect to ε are straightforward to obtain from Eq. (5.2) as

$$\frac{\partial \tan\alpha}{\partial \varepsilon} = -\frac{\tan\alpha}{1+\varepsilon} \quad \text{and} \tag{5.29}$$

$$\frac{\partial \alpha}{\partial \varepsilon} = -\frac{\sin\alpha \, \cos\alpha}{1+\varepsilon} \quad . \tag{5.30}$$

The key term to be determined here is the derivative $\partial s_{OB}/\partial \varepsilon$ of the total length s_{OB} of the (wrapped) strand on the surface with respect to the strain ε. This derivative is abbreviated in the following by the symbol

$$\kappa_{OB}^{\varepsilon} = \frac{\partial s_{OB}}{\partial \varepsilon} \tag{5.31}$$

describing the linear transmission factor from infinitesimal changes $\mathrm{d}\varepsilon$ of the strain to infinitesimal changes $\mathrm{d}s_{OB}$ for fixed surface end-point σ_B of the wrapped strand after elongation. Clearly, this is a coupled problem as after elongation the strand changes geometry and, thus, both the length of the strand as well as its wrapping behaviour change.

In this setting, since the centerline of a cone wrapped around a circle is shaped as a logarithmic spiral, $\partial s_{OB}/\partial \varepsilon = \kappa_{OB}^{\varepsilon}$ can be found on the one side by direct derivation of s_{OB} with respect to ε as expanded out in the next section. On the other side, the transmission factor $\kappa_{OB}^{\varepsilon}$ can be determined by perturbation theory, which is the general case and which is explained in Section **5.1.4** for the case of a conical muscle and circular surface and compared to the explicit solution of Section **5.1.3** as a preparation of the general case.

5.1.3   Direct derivation of s_{OB} with respect to strain for a logarithmic spiral

For the direct derivation of s_{OB} with respect to the strain ε, the total length of the wrapped muscle centerline s_{OB} has to be calculated first. By quadrature-integration of

$$\mathrm{d}s = (\rho \, \cos\alpha + \tan\alpha \, s) \, \mathrm{d}\varphi \tag{5.32}$$

after separation of variables, this leads to

$$s(\varphi) = \frac{\rho \cos\alpha}{\tan\alpha} \left(e^{\tan\alpha\,\varphi} - 1 \right) + s_{OA}\, e^{\tan\alpha\,\varphi} \tag{5.33}$$

for the initial values $s_0 = s_{OA}$ and $\varphi_0 = 0$ for simplification without loss of generality. The rate with which the length of the centerline s changes if the strain ε is varied while the other variables are held constant can be determined by direct derivation of Eq. (5.33) with respect to ε

$$\begin{aligned}
\frac{\partial s}{\partial \varepsilon}(\varphi) &= \frac{\rho \frac{\partial \cos\alpha}{\partial \varepsilon}}{\tan\alpha} \left(e^{\tan\alpha\,\varphi} - 1 \right) \\
&\quad - \frac{\rho \cos\alpha}{\tan^2\alpha} \frac{\partial \tan\alpha}{\partial \varepsilon} \left(e^{\tan\alpha\,\varphi} - 1 \right) \\
&\quad + \frac{\rho \cos\alpha}{\tan\alpha} \frac{\partial \tan\alpha}{\partial \varepsilon} \varphi\, e^{\tan\alpha\,\varphi} \\
&\quad + s_{OA} \frac{\partial \tan\alpha}{\partial \varepsilon} \varphi\, e^{\tan\alpha\,\varphi} \\
&\quad + \frac{\partial s_{OA}}{\partial \varepsilon} e^{\tan\alpha\,\varphi}
\end{aligned} \tag{5.34}$$

with

$$\frac{\partial \cos\alpha}{\partial \varepsilon} = -\sin\alpha \frac{\partial \alpha}{\partial \varepsilon} \quad . \tag{5.35}$$

Thus, for $\partial s_{OB}/\partial \varepsilon$ it holds after setting $\varphi \equiv \varphi_B$

$$\frac{\partial s_{OB}}{\partial \varepsilon} = \frac{\partial s}{\partial \varepsilon}(\varphi_B) = \kappa_{OB}^\varepsilon \quad . \tag{5.36}$$

5.1.4   Derivative of s_{OB} with respect to strain using perturbation theory

In order to generalize the determination of $\partial s_{OB}/\partial \varepsilon = \kappa_{OB}^\varepsilon$, perturbation theory[6, 43] is applied. Hereby, the differential equation

$$\frac{\mathrm{d}s}{\mathrm{d}\varphi} = f(s, \varphi; \varepsilon) = \rho \cos\alpha(\varepsilon) + \tan\alpha(\varepsilon)\, s \tag{5.37}$$

is solved using first-order perturbation theory where a change in the longitudinal strain is interpreted as a small perturbation $\mathrm{d}\varepsilon$ leading to

$$s(\varphi, \mathrm{d}\varepsilon) = s_1(\varphi) + s_2(\varphi)\, \mathrm{d}\varepsilon \quad . \tag{5.38}$$

Applied to Eq. (5.37), this results in

$$\frac{\mathrm{d}}{\mathrm{d}\varphi} s_1 + \frac{\mathrm{d}}{\mathrm{d}\varphi} s_2\, \mathrm{d}\varepsilon = f_0(s_1, \varphi; \varepsilon) + \left(\left.\frac{\partial f}{\partial s}\right|_{\varepsilon=\mathrm{const}} s_2 + \left.\frac{\partial f}{\partial \varepsilon}\right|_{s=\mathrm{const}} \right) \mathrm{d}\varepsilon \tag{5.39}$$

which with

$$\left.\frac{\partial f}{\partial s}\right|_{\varepsilon=\text{const}} = \tan\alpha(\varepsilon) \quad \text{and} \tag{5.40}$$

$$\left.\frac{\partial f}{\partial \varepsilon}\right|_{s=\text{const}} = \rho\,\frac{\partial \cos\alpha}{\partial \varepsilon} + \frac{\partial \tan\alpha}{\partial \varepsilon}\,s \tag{5.41}$$

leads to

$$\frac{\mathrm{d}}{\mathrm{d}\varphi}s_1 + \frac{\mathrm{d}}{\mathrm{d}\varphi}s_2\,\mathrm{d}\varepsilon = \rho\cos\alpha + \tan\alpha\,s_1$$

$$+ \tan\alpha\,s_2\,\mathrm{d}\varepsilon$$

$$+ \rho\,\frac{\partial \cos\alpha}{\partial \varepsilon}\,\mathrm{d}\varepsilon + \frac{\partial \tan\alpha}{\partial \varepsilon}\,[s_1 + s_2\,\mathrm{d}\varepsilon]\,\mathrm{d}\varepsilon \quad . \tag{5.42}$$

Equating coefficients, this yields the two differential equations

$$\frac{\mathrm{d}}{\mathrm{d}\varphi}s_1 = \rho\cos\alpha + \tan\alpha\,s_1 \tag{5.43}$$

$$\frac{\mathrm{d}}{\mathrm{d}\varphi}s_2 = \tan\alpha\,s_2 + \rho\,\frac{\partial \cos\alpha}{\partial \varepsilon} + \frac{\partial \tan\alpha}{\partial \varepsilon}\,s_1 \tag{5.44}$$

that can be solved successively. The integration of Eq. (5.43) can be done explicitly resulting in

$$s_1(\varphi) = \frac{\rho\cos\alpha}{\tan\alpha}\left(e^{\tan\alpha\,\varphi} - 1\right) + s_{OA}\,e^{\tan\alpha\,\varphi} \tag{5.45}$$

for the initial values $\varphi_0 = 0$ and $s_0 = s_{OA}$. The inhomogeneous differential equation Eq. (5.44)

$$\frac{\mathrm{d}}{\mathrm{d}\varphi}s_2 - \tan\alpha\,s_2 = \rho\,\frac{\partial \cos\alpha}{\partial \varepsilon} + \frac{\partial \tan\alpha}{\partial \varepsilon}\,s_1 \tag{5.46}$$

leads to the solution

$$s_2 = s_{2,H} + s_{2,P} \tag{5.47}$$

where $s_{2,H}$ is the homogeneous solution and $s_{2,P}$ is the particular solution. The homogeneous equation

$$\frac{\mathrm{d}}{\mathrm{d}\varphi}s_{2,H} - \tan\alpha\,s_{2,H} = 0 \tag{5.48}$$

is solved by separation of variables as

$$s_{2,H} = C\,\exp\left(-\int_0^\varphi -\tan\alpha\,\mathrm{d}\bar\varphi\right) = C\,e^{\tan\alpha\,\varphi} \quad . \tag{5.49}$$

The particular solution is found by replacing the coefficient C of integration by the function $K(\varphi)$ and inserting

$$s_{2,P} = K(\varphi) \, e^{\tan\alpha \, \varphi} \tag{5.50}$$

$$\frac{\mathrm{d}}{\mathrm{d}\varphi} s_{2,P} = \frac{\mathrm{d}K(\varphi)}{\mathrm{d}\varphi} e^{\tan\alpha \, \varphi} + K(\varphi) \tan\alpha \, e^{\tan\alpha \, \varphi} \tag{5.51}$$

into Eq. (5.46). This leads to

$$\frac{\mathrm{d}K(\varphi)}{\mathrm{d}\varphi} = e^{-\tan\alpha \, \varphi} \left\{ \rho \frac{\partial \cos\alpha}{\partial \varepsilon} + \frac{\partial \tan\alpha}{\partial \varepsilon} s_1 \right\} \tag{5.52}$$

which together with Eq. (5.45) results in

$$\frac{\mathrm{d}K(\varphi)}{\mathrm{d}\varphi} = e^{-\tan\alpha \, \varphi} \rho \frac{\partial \cos\alpha}{\partial \varepsilon} + \frac{\partial \tan\alpha}{\partial \varepsilon} \frac{\rho \cos\alpha}{\tan\alpha} \left(1 - e^{-\tan\alpha \, \varphi} \right)$$
$$+ s_{OA} \frac{\partial \tan\alpha}{\partial \varepsilon} \quad . \tag{5.53}$$

Integration leads to

$$K(\varphi) = \int_0^\varphi \frac{\mathrm{d}}{\mathrm{d}\varphi} K(\bar\varphi) \mathrm{d}\bar\varphi$$
$$= \frac{1}{-\tan\alpha} \rho \frac{\partial \cos\alpha}{\partial \varepsilon} \left(e^{-\tan\alpha \, \varphi} - 1 \right)$$
$$+ \frac{\partial \tan\alpha}{\partial \varepsilon} \frac{\rho \cos\alpha}{\tan\alpha} \left\{ \varphi + \frac{1}{\tan\alpha} \left(e^{-\tan\alpha \, \varphi} - 1 \right) \right\}$$
$$+ s_{OA} \, \varphi \frac{\partial \tan\alpha}{\partial \varepsilon} \tag{5.54}$$

which together with Eq. (5.50), yields

$$s_{2,P} = \frac{\rho \frac{\partial \cos\alpha}{\partial \varepsilon}}{\tan\alpha} \left(e^{\tan\alpha \, \varphi} - 1 \right)$$
$$- \frac{\rho \cos\alpha}{\tan^2\alpha} \frac{\partial \tan\alpha}{\partial \varepsilon} \left(e^{\tan\alpha \, \varphi} - 1 \right)$$
$$+ \frac{\rho \cos\alpha}{\tan\alpha} \frac{\partial \tan\alpha}{\partial \varepsilon} \varphi \, e^{\tan\alpha \, \varphi}$$
$$+ s_{OA} \frac{\partial \tan\alpha}{\partial \varepsilon} \varphi \, e^{\tan\alpha \, \varphi} \quad . \tag{5.55}$$

By requiring the initial condition

$$s_2(\varphi_0) = \frac{\partial s_{OA}}{\partial \varepsilon} \quad , \tag{5.56}$$

it follows

$$C \equiv s_2(\varphi_0) = \frac{\partial s_{OA}}{\partial \varepsilon} \tag{5.57}$$

and the overall solution becomes

$$
\begin{aligned}
s_2(\varphi) =\ & \frac{\rho\,\frac{\partial\cos\alpha}{\partial\varepsilon}}{\tan\alpha}\left(e^{\tan\alpha\,\varphi}-1\right) \\
& -\frac{\rho\cos\alpha}{\tan^2\alpha}\,\frac{\partial\tan\alpha}{\partial\varepsilon}\left(e^{\tan\alpha\,\varphi}-1\right) \\
& +\frac{\rho\cos\alpha}{\tan\alpha}\,\frac{\partial\tan\alpha}{\partial\varepsilon}\,\varphi\,e^{\tan\alpha\,\varphi} \\
& +s_{OA}\,\frac{\partial\tan\alpha}{\partial\varepsilon}\,\varphi\,e^{\tan\alpha\,\varphi} \\
& +\frac{\partial s_{OA}}{\partial\varepsilon}\,e^{\tan\alpha\,\varphi}\ .
\end{aligned}
\tag{5.58}
$$

Thus, both perturbation theory and the explicit solution render the same results, as expected.

5.2   Case 2: Stretching cone on ellipse

In an intermediate step, the equations are now extended for the case where the radius of curvature of the contact surface is not constant, as is the case for the ellipse exemplarily shown in Fig. 5.3. As already introduced in Chapter **3**, φ is now replaced by σ as surface coordinate, defining the actual position on the surface. Consequently, the only difference from the derivation in the last chapter is that the radius of curvature now depends on σ. Accordingly, the same constraint equations, now formulated in general terms with $\Delta \underline{r}_{OA} = \underline{r}_A - \underline{r}_O = \underline{r}_Q(\sigma_A) + b_A\,\underline{e}^\perp_{CA} - \underline{r}_O$ for an arbitrary surface and $b_A = s_{OA}\tan\alpha$ and $b_B = s_{OB}\tan\alpha$ for a cone shaped muscle, result as

$$
g_{1A} = \qquad s_{OA} - \left[\underline{r}_Q(\sigma_A) - \underline{r}_O\right]\cdot\underline{e}_C(\sigma_A,\varepsilon) = 0
\tag{5.59}
$$

$$
g_{2A} = \tan\alpha(\varepsilon)\,s_{OA} + \left[\underline{r}_Q(\sigma_A) - \underline{r}_O\right]\cdot\underline{e}^\perp_C(\sigma_A,\varepsilon) = 0
\tag{5.60}
$$

for end A and

$$
g_{1B} = \left[\underline{r}_I - \underline{r}_Q(\sigma_B)\right]\cdot\underline{e}_C(\sigma_B,\varepsilon) + \qquad s_{OB}(\varepsilon) - \ell(\varepsilon) = 0
\tag{5.61}
$$

$$
g_{2B} = \left[\underline{r}_I - \underline{r}_Q(\sigma_B)\right]\cdot\underline{e}^\perp_C(\sigma_B,\varepsilon) - \tan\alpha(\varepsilon)\,s_{OB}(\varepsilon) \qquad\ = 0
\tag{5.62}
$$

for end B. For the adjusted state vectors with now general surface coordinate σ, one obtains

$$
\underline{z}_A = \begin{bmatrix} s_{OA} \\ \sigma_A \end{bmatrix} \quad \text{and} \quad \underline{z}_B = \begin{bmatrix} s_I \\ \sigma_B \end{bmatrix}\ ,
\tag{5.63}
$$
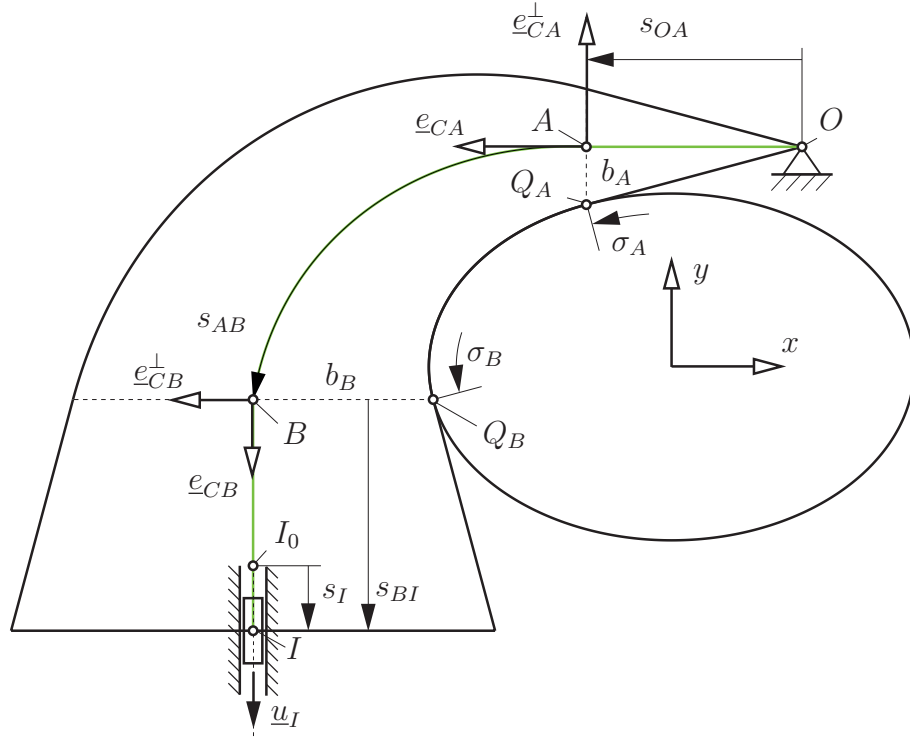
Figure 5.3: Case 2: Cone stretching over ellipse

and the following Jacobian matrices are obtained

$$
\mathrm{J}_A = \frac{\partial g_A}{\partial \underline{z}_A} = \begin{bmatrix} 1 & -\rho_A \cos\alpha + \left[\underline{r}_{Q,A} - \underline{r}_O\right] \cdot \underline{e}_{CA}^{\perp} \\ \tan\alpha & -\rho_A \sin\alpha + \left[\underline{r}_{Q,A} - \underline{r}_O\right] \cdot \underline{e}_{CA} \end{bmatrix} \begin{bmatrix} 1 & 0 \\ 0 & \dfrac{\mathrm{d}\varphi}{\mathrm{d}\sigma} \end{bmatrix} \tag{5.64}
$$

$$
\mathrm{J}_B = \frac{\partial g_B}{\partial \underline{z}_B}
$$

$$
= \begin{bmatrix} \underline{u}_I \cdot \underline{e}_{CB} & -\rho_B \cos\alpha + (\rho_B \cos\alpha + b_B) - \left[\underline{r}_I - \underline{r}_{Q,B}\right] \cdot \underline{e}_{CB}^{\perp} \\ \underline{u}_I \cdot \underline{e}_{CB}^{\perp} & -\rho_B \sin\alpha + \tan\alpha(\rho_B \cos\alpha + b_B) + \left[\underline{r}_I - \underline{r}_{Q,B}\right] \cdot \underline{e}_{CB} \end{bmatrix} \begin{bmatrix} 1 & 0 \\ 0 & \dfrac{\mathrm{d}\varphi}{\mathrm{d}\sigma} \end{bmatrix}
$$

$$
\tag{5.65}
$$

where $\mathrm{d}\varphi/\mathrm{d}\sigma$ depends on the chosen surface curve geometry and are given for the example of an ellipse in Eq. (3.25). The implicit constraints at velocity level are

$$
\dot{g}_A = \mathrm{J}_A \dot{\underline{z}}_A + \frac{\partial g_A}{\partial \varepsilon} \dot{\varepsilon} \overset{!}{=} 0 \tag{5.66}
$$

$$
\dot{g}_B = \mathrm{J}_B \dot{\underline{z}}_B + \frac{\partial g_B}{\partial \varepsilon} \dot{\varepsilon} \overset{!}{=} 0 \quad . \tag{5.67}
$$

Hereby, the constraints at A and B have to be derived with respect to ε. For this, the derivatives of the cross-section vectors $\underline{e}_C$ and $\underline{e}_C^{\perp}$ with respect to ε are needed, which
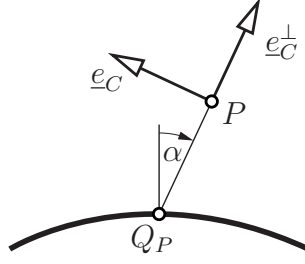
Figure 5.4: Schematic illustration of the relation between the cross-section vectors $\underline{e}_C$ and $\underline{e}_C^\perp$ and the muscle half-angle α

in turn can be obtained with the help of the chain rule by

$$\frac{\partial \underline{e}_C}{\partial \varepsilon} = \frac{\partial \underline{e}_C}{\partial \alpha} \frac{\partial \alpha}{\partial \varepsilon} = \quad \underline{e}_C^\perp \frac{\partial \alpha}{\partial \varepsilon} \tag{5.68}$$

$$\frac{\partial \underline{e}_C^\perp}{\partial \varepsilon} = \frac{\partial \underline{e}_C^\perp}{\partial \alpha} \frac{\partial \alpha}{\partial \varepsilon} = -\underline{e}_C \frac{\partial \alpha}{\partial \varepsilon} \tag{5.69}$$

where $\partial \alpha / \partial \varepsilon$ depends on the muscle's geometry and, for the cone, is already given in Eq. (5.30), whereas the relation between the cross-section vectors $\underline{e}_C$ and $\underline{e}_C^\perp$ and the half-angle α are visualized in Fig. 5.4.

The derivatives of the constraints with respect to ε can be formulated as

$$\frac{\partial g_{1A}}{\partial \varepsilon} = \left(- \left[\underline{r}_{Q,A} - \underline{r}_O \right] \cdot \underline{e}_C^\perp \right) \qquad\qquad \frac{\partial \alpha}{\partial \varepsilon} \tag{5.70}$$

$$\frac{\partial g_{2A}}{\partial \varepsilon} = \left(- \left[\underline{r}_{Q,A} - \underline{r}_O \right] \cdot \underline{e}_C + s_{OA} \left[1 + \tan^2\alpha \right] \right) \frac{\partial \alpha}{\partial \varepsilon} \tag{5.71}$$

for end A and as

$$\frac{\partial g_{1B}}{\partial \varepsilon} = \quad \underline{r}_I \cdot \underline{e}_C^\perp \frac{\partial \alpha}{\partial \varepsilon} - \rho_B \cos\alpha \frac{\partial \alpha}{\partial \varepsilon} + \quad \frac{\partial s_{OB}}{\partial \varepsilon} - \ell_0 \tag{5.72}$$

$$\frac{\partial g_{2B}}{\partial \varepsilon} = -\underline{r}_I \cdot \underline{e}_C \frac{\partial \alpha}{\partial \varepsilon} + \rho_B \sin\alpha \frac{\partial \alpha}{\partial \varepsilon} - \tan\alpha \frac{\partial s_{OB}}{\partial \varepsilon} - \left[1 + \tan^2\alpha \right] \frac{\partial \alpha}{\partial \varepsilon} s_{OB} \tag{5.73}$$

for end B. While the derivatives of the cone half-angle α with respect to ε is the same as in Section **5.1.2**, now when computing $\partial s_{OB}/\partial \varepsilon$, the variable radius of curvature ρ has to be taken into account.

5.2.1 Wrapping path from O to B for stretched conical muscle

In order to find the infinitesimal change in the path length s_{OB} with respect to an infinitesimal change of the strain ε , perturbation theory is used like introduced in Section **5.1.4**.

Thus, the differential equation

$$\frac{\partial s}{\partial \sigma} = \left[\rho(\sigma) \cos\left(\alpha\left(s\left(\varepsilon\right)\right)\right) + b\left(s\left(\varepsilon\right)\right)\right] \frac{\mathrm{d}\varphi}{\mathrm{d}\sigma} \tag{5.74}$$

$$= f(s, \sigma, \varepsilon) \tag{5.75}$$

is solved using first-order perturbation theory where a change in the longitudinal strain is interpreted as a small perturbation $\mathrm{d}\varepsilon$ leading to

$$s(\sigma; \mathrm{d}\varepsilon) = s_1(\sigma) + s_2(\sigma)\,\mathrm{d}\varepsilon \quad. \tag{5.76}$$

Applying that to the differential equation yields

$$\frac{\mathrm{d}s_1}{\mathrm{d}\sigma} + \mathrm{d}\varepsilon\,\frac{\mathrm{d}s_2}{\mathrm{d}\sigma} = f(s_1 + \mathrm{d}\varepsilon\,s_2, \sigma, \varepsilon + \mathrm{d}\varepsilon)$$

$$= f(s_1, \sigma, \varepsilon) + \left.\frac{\mathrm{d}f}{\mathrm{d}s}\right|_{\varepsilon=\mathrm{const}} s_2\,\mathrm{d}\varepsilon + \left.\frac{\mathrm{d}f}{\mathrm{d}\varepsilon}\right|_{s=\mathrm{const}} \mathrm{d}\varepsilon$$

$$= f(s_1, \sigma, \varepsilon) + \left(\left.\frac{\mathrm{d}f}{\mathrm{d}s}\right|_{\varepsilon=\mathrm{const}} s_2 + \left.\frac{\mathrm{d}f}{\mathrm{d}\varepsilon}\right|_{s=\mathrm{const}}\right)\mathrm{d}\varepsilon \tag{5.77}$$

and equating the coefficients with respect to $\mathrm{d}\varepsilon$ is leading to the system of linear differential equations

$$\frac{\mathrm{d}s_1}{\mathrm{d}\sigma} = f(s_1, \sigma, \varepsilon)$$

$$\frac{\mathrm{d}s_2}{\mathrm{d}\sigma} = \left.\frac{\mathrm{d}f}{\mathrm{d}s}\right|_{\varepsilon=\mathrm{const}} s_2 + \left.\frac{\mathrm{d}f}{\mathrm{d}\varepsilon}\right|_{s=\mathrm{const}} \tag{5.78}$$

with

$$s_1 \mathrel{\widehat{=}} s_{OB} \tag{5.79}$$

$$s_2 \mathrel{\widehat{=}} \frac{\partial s_{OB}}{\partial \varepsilon} = \kappa_{OB}^{\varepsilon} \quad. \tag{5.80}$$

This leads to the coupled ODEs

$$\begin{bmatrix} \dfrac{\partial s}{\partial \sigma} \\[2ex] \dfrac{\partial \kappa_{OB}^{\varepsilon}}{\partial \sigma} \end{bmatrix} = \begin{bmatrix} \rho\,\cos\alpha + s\,\tan\alpha \\[2ex] \kappa_{OB}^{\varepsilon}\,\tan\alpha + \rho\,\frac{\partial \cos\alpha}{\partial \varepsilon} + s\,\frac{\partial \tan\alpha}{\partial \varepsilon} \end{bmatrix} \frac{\mathrm{d}\varphi}{\mathrm{d}\sigma} \tag{5.81}$$

that have to be solved for the interval $[\sigma_A, \sigma_B]$ for initial values

$$s(\sigma_A) = s_{OA} \tag{5.82}$$

$$\kappa_{OB}^{\varepsilon} = \frac{\partial s_{OA}}{\partial \varepsilon} \quad. \tag{5.83}$$

5.3   Case 3: Stretching curved muscle on ellipse

5.3.1   Curved muscle geometry

In this section, the algorithm is extended for a curved muscle geometry with variable muscle thickness $\partial\alpha/\partial s \neq 0$. As part of the derivation, a parabolic muscle geometry will be presented here as an example, which can be approximated to the conical muscle geometry by parameter selection for comparison purposes. However, it is generally possible to use any convex muscle geometry.
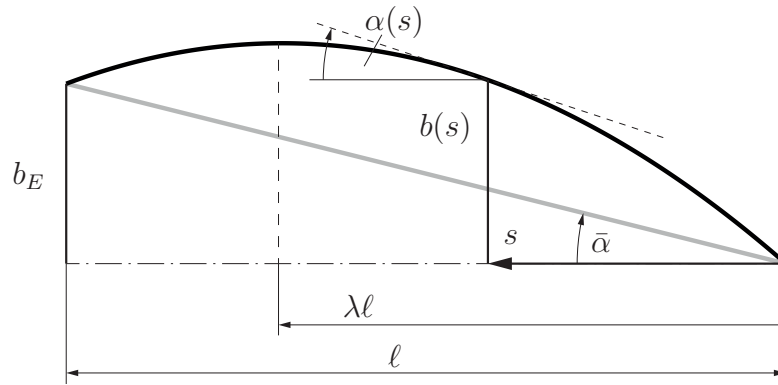
Figure 5.5: Case 3: Parabolic example for a curved muscle geometry

The half-width b of the curved muscle shown in Fig. 5.5 depending on the position s on the centerline is defined by

$$b(s) = \frac{b_E}{\ell\,(2\lambda - 1)}\left(2\lambda\,s - \frac{s^2}{\ell}\right) \tag{5.84}$$

starting at zero for $s = 0$ and with half-width b_E at the end of the muscle for $s = \ell$ with ℓ being the muscle's total length. Thus, the half-angle α between the tangent to the curve and the centerline is now variable and depending on s. The position of the vertex of the parabola is defined by the parameter $\lambda > 0.5$. For $\lambda \to \infty$, the geometry of the parabolic muscle for the range considered $0 \leq s \leq \ell$ approximates that of a cone with half the opening angle $\bar{\alpha} = \arctan\left(b_E/\ell\right)$ as indicated in gray.

5.3.2   Lateral contraction

As a first rough consideration of the deformation of the muscle due to stretching, the lateral contraction is exemplarily introduced using Poisson's ratio[16, 53], which defines

the ratio of the volume change related to the length change

$$\frac{\Delta V}{V} = (1 - 2\nu) \frac{\Delta \ell}{\ell} \tag{5.85}$$

where ν denotes the Poisson's ratio. For simplicity, instead of the volume, the area of the cross-section is used in the present context, leading to

$$\frac{A(\ell) - A(\ell_0)}{A(\ell_0)} = (1 - 2\nu) \frac{\ell - \ell_0}{\ell_0} \tag{5.86}$$

with the actual muscle length ℓ and the length of the unstretched muscle ℓ_0 and

$$A(\ell) = \int_0^\ell b(s) \ \mathrm{d}s = \frac{b_E \ell}{2\lambda - 1} \frac{3\lambda - 1}{3} \quad . \tag{5.87}$$

Let the muscle geometry for the unstretched case be defined by the parameters b_E^0, λ and ℓ_0. Then the actual parameter b_E for the current longitudinal strain ε can be calculated by

$$b_E(\varepsilon) = b_E^0 \left(1 - 2\nu \frac{\varepsilon}{1 + \varepsilon} \right) \tag{5.88}$$

after substituting $\ell = \ell_0(1 + \varepsilon)$ and Eq. (5.87) into Eq. (5.86).

After inserting Eq. (5.88) into Eq. (5.84), the derivatives with respect to s and ε are straightforward to calculate.

5.3.3   Boundary constraints at A and B

As illustrated in Fig. 5.6, the curved muscle is now wrapped in place of the cone over the ellipse, with its end O fixed and its end I vertically slidable as before. Again, an orthogonality and a length condition apply at both connection points A and B, as derived in more detail in Chapter **5.1.1**, leading to the equations

$$g_{1A} = \quad s_{OA} - \left[\underline{r}_Q(\sigma_A) - \underline{r}_O \right] \cdot \underline{e}_C(\sigma_A, s_{OA}, \varepsilon) = 0 \tag{5.89}$$

$$g_{2A} = b(s_{OA}) + \left[\underline{r}_Q(\sigma_A) - \underline{r}_O \right] \cdot \underline{e}_C^\perp(\sigma_A, s_{OA}, \varepsilon) = 0 \tag{5.90}$$

at end A and

$$g_{1B} = \left[\underline{r}_I - \underline{r}_Q(\sigma_B) \right] \cdot \underline{e}_C(\sigma_B, s_{OB}, \varepsilon) + \quad s_{OB}(\varepsilon) - \ell(\varepsilon) = 0 \tag{5.91}$$

$$g_{2B} = \left[\underline{r}_I - \underline{r}_Q(\sigma_B) \right] \cdot \underline{e}_C^\perp(\sigma_B, s_{OB}, \varepsilon) - b(s_{OB}, \varepsilon) \quad = 0 \tag{5.92}$$
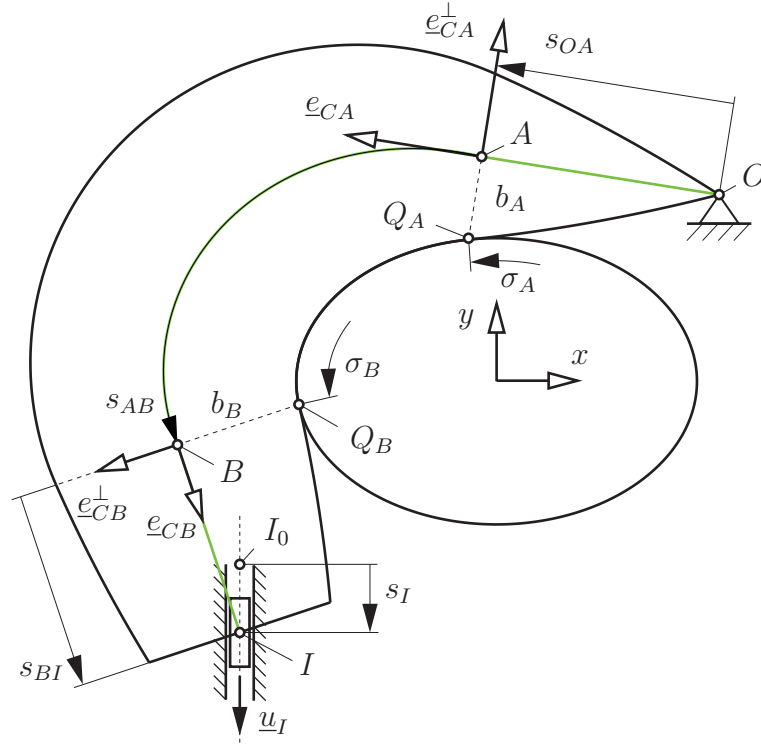
Figure 5.6: Case 3: Curved muscle stretching over ellipse

at end B with the difference to Section **5.2** that the inclination of the cross-section vectors $\underline{e}_C$ and $\underline{e}_C^\perp$ now not only depends on the surface coordinate σ and the longitudinal strain ε, but also on the actual muscle half-angle α, which itself depends on the corresponding centerline coordinate s. Defining again the state vectors at A and B as

$$\underline{z}_A = \begin{bmatrix} s_{OA} \\ \sigma_A \end{bmatrix} \quad \text{and} \quad \underline{z}_B = \begin{bmatrix} s_I \\ \sigma_B \end{bmatrix} , \tag{5.93}$$

the implicit constraints at velocity level apply as

$$\dot{\underline{g}}_A = \mathrm{J}_A\, \dot{\underline{z}}_A + \frac{\partial \underline{g}_A}{\partial \varepsilon}\, \dot{\varepsilon} \stackrel{!}{=} 0 \qquad \text{and} \tag{5.94}$$

$$\dot{\underline{g}}_B = \mathrm{J}_B\, \dot{\underline{z}}_B + \frac{\partial \underline{g}_B}{\partial \varepsilon}\, \dot{\varepsilon} \stackrel{!}{=} 0 \ . \tag{5.95}$$

At end A, the derivatives of $\underline{e}_{CA}$ and $\underline{e}_{CA}^\perp$ with respect to φ are again

$$\frac{\partial \underline{e}_{CA}}{\partial \varphi} = -\underline{e}_{CA}^\perp \tag{5.96}$$

$$\frac{\partial \underline{e}_{CA}^\perp}{\partial \varphi} = \underline{e}_{CA} \ . \tag{5.97}$$

At B, the change in the muscle length in the wrapped segment s_{AB} leads to a change in the total muscle length s_{OB} at B and thus to a change in φ_B as

$$\frac{\partial \underline{e}_{CB}}{\partial \varphi} = \underline{e}_{CB}^{\perp} \left[-1 + \frac{\partial \alpha}{\partial s} \frac{\partial s_{OB}}{\partial \varphi} \right] \tag{5.98}$$

$$\frac{\partial \underline{e}_{CB}^{\perp}}{\partial \varphi} = \underline{e}_{CB} \left[1 - \frac{\partial \alpha}{\partial s} \frac{\partial s_{OB}}{\partial \varphi} \right] \quad . \tag{5.99}$$

As derived in Chapter **4**, the arc length ODE for $\alpha \neq$ const and $\rho \neq$ const to compute the wrapping path between O and B is

$$\frac{\partial s}{\partial \sigma} = \frac{\partial s}{\partial \varphi} \frac{\mathrm{d}\varphi}{\mathrm{d}\sigma} = \frac{\rho(\sigma) \, \cos\left(\alpha\left(s\right)\right) + b\left(s\right)}{1 + b\left(s\right) \frac{\partial \alpha}{\partial s}} \frac{\mathrm{d}\varphi}{\mathrm{d}\sigma} \quad . \tag{5.100}$$

leading to

$$\frac{\partial \underline{e}_{CB}}{\partial \varphi} = -\underline{e}_{CB}^{\perp} \left[1 - \mathcal{X}_B \left. \frac{\partial \alpha}{\partial s} \right|_B \right] \qquad \text{and} \tag{5.101}$$

$$\frac{\partial \underline{e}_{CB}^{\perp}}{\partial \varphi} = \underline{e}_{CB} \left[1 - \mathcal{X}_B \left. \frac{\partial \alpha}{\partial s} \right|_B \right] \tag{5.102}$$

with

$$\mathcal{X}_B = \frac{\partial s_{OB}}{\partial \varphi} = \left. \frac{\rho \, \cos\alpha + b}{1 + b\frac{\partial \alpha}{\partial s}} \right|_B \quad . \tag{5.103}$$

Additionally applying

$$\frac{\partial \underline{r}_{OQA}}{\partial \varphi} = \rho_A \, \underline{e}_t^A \quad , \tag{5.104}$$

$$\frac{\partial \underline{r}_{QBI}}{\partial \varphi} = -\rho_B \, \underline{e}_t^B \quad , \tag{5.105}$$

$$\frac{\partial \ell}{\partial \varphi} = 0 \quad \text{and} \tag{5.106}$$

$$\frac{\partial b}{\partial \varphi} = \frac{\partial b}{\partial s} \frac{\partial s}{\partial \varphi} = \tan\alpha \, \mathcal{X}_B \quad , \tag{5.107}$$

it holds for the Jacobians

$$\mathrm{J}_A = \frac{\partial \underline{g}_A}{\partial \underline{z}_A} = \begin{bmatrix} 1 - \underline{r}_{OQA} \cdot \underline{e}_{CA}^{\perp} \left. \frac{\partial \alpha}{\partial s} \right|_A & -\rho_A \, \cos\alpha_A + \underline{r}_{OQA} \cdot \underline{e}_{CA}^{\perp} \\ \tan\alpha_A - \underline{r}_{OQA} \cdot \underline{e}_{CA} \left. \frac{\partial \alpha}{\partial s} \right|_A & -\rho_A \, \sin\alpha_A + \underline{r}_{OQA} \cdot \underline{e}_{CA} \end{bmatrix} \begin{bmatrix} 1 & 0 \\ 0 & \frac{\mathrm{d}\varphi}{\mathrm{d}\sigma} \end{bmatrix} \tag{5.108}$$

with $\underline{r}_{OQA} = \left[\underline{r}_{Q,A} - \underline{r}_O \right]$ and

$$\mathrm{J}_B = \frac{\partial \underline{g}_B}{\partial \underline{z}_B}$$

$$= \begin{bmatrix} \underline{u}_I \cdot \underline{e}_{CB} & -\rho_B \, \cos\alpha_B - \underline{r}_{QBI} \underline{e}_{CB}^{\perp} \left(1 - \mathcal{X}_B \left. \frac{\partial \alpha}{\partial s} \right|_B \right) + \mathcal{X}_B \\ \underline{u}_I \cdot \underline{e}_{CB}^{\perp} & -\rho_B \, \sin\alpha_B + \underline{r}_{QBI} \, \underline{e}_{CB} \left(1 - \mathcal{X}_B \left. \frac{\partial \alpha}{\partial s} \right|_B \right) - \tan\alpha_B \, \mathcal{X}_B \end{bmatrix} \begin{bmatrix} 1 & 0 \\ 0 & \frac{\mathrm{d}\varphi}{\mathrm{d}\sigma} \end{bmatrix} \tag{5.109}$$

with $\underline{r}_{QBI} = \left[\underline{r}_I - \underline{r}_{Q,B} \right]$.

Differentiating the constraints Eq. (5.89) - Eq. (5.92) with respect to ε leads to

$$\frac{\partial g_{1A}}{\partial \varepsilon} = - \left[\underline{r}_{Q,A} - \underline{r}_O \right] \cdot \underline{e}_C^\perp \left. \frac{\partial \alpha}{\partial \varepsilon} \right|_A \tag{5.110}$$

$$\frac{\partial g_{2A}}{\partial \varepsilon} = - \left[\underline{r}_{Q,A} - \underline{r}_O \right] \cdot \underline{e}_C \left. \frac{\partial \alpha}{\partial \varepsilon} \right|_A + \frac{\partial b_A}{\partial \varepsilon} \tag{5.111}$$

at end A and to

$$\frac{\partial g_{1B}}{\partial \varepsilon} = \left[\underline{r}_I - \underline{r}_{Q,B} \right] \cdot \underline{e}_C^\perp \left. \frac{\partial \alpha}{\partial \varepsilon} \right|_B + \frac{\partial s_{OB}}{\partial \varepsilon} - \ell_0 \tag{5.112}$$

$$\frac{\partial g_{2B}}{\partial \varepsilon} = - \left[\underline{r}_I - \underline{r}_{Q,B} \right] \cdot \underline{e}_C \left. \frac{\partial \alpha}{\partial \varepsilon} \right|_B - \frac{\partial b_B}{\partial \varepsilon} \tag{5.113}$$

at end B. Note that while the derivatives of the cross-section radius b and the muscle half-angle α with respect to ε at A only consist in the formula given by the muscle's geometry differentiated with respect to ε, at B, also the change of the muscle's length at B due to the length change in the wrapped segment s_{OB} caused by the muscle deformation have to be taken into account as

$$\left. \frac{\partial \alpha}{\partial \varepsilon} \right|_B = \left. \frac{\partial \alpha}{\partial \varepsilon} \right|_{s_{OB}=\text{const}} + \frac{\partial \alpha}{\partial s} \frac{\partial s_{OB}}{\partial \varepsilon} \tag{5.114}$$

$$\frac{\partial b_B}{\partial \varepsilon} = \left. \frac{\partial b_B}{\partial \varepsilon} \right|_{s_{OB}=\text{const}} + \frac{\partial b}{\partial s} \frac{\partial s_{OB}}{\partial \varepsilon} \quad . \tag{5.115}$$

This finally leads to

$$\frac{\partial g_{1B}}{\partial \varepsilon} = \underline{r}_{QBI} \cdot \underline{e}_C^\perp \left\{ \left. \frac{\partial \alpha}{\partial \varepsilon} \right|_{s_{OB}=\text{const}} + \frac{\partial \alpha}{\partial s} \frac{\partial s_{OB}}{\partial \varepsilon} \right\} + \frac{\partial s_{OB}}{\partial \varepsilon} - \ell_0 \tag{5.116}$$

$$\frac{\partial g_{2B}}{\partial \varepsilon} = - \underline{r}_{QBI} \cdot \underline{e}_C \left\{ \left. \frac{\partial \alpha}{\partial \varepsilon} \right|_{s_{OB}=\text{const}} + \frac{\partial \alpha}{\partial s} \frac{\partial s_{OB}}{\partial \varepsilon} \right\} - \left. \frac{\partial b_B}{\partial \varepsilon} \right|_{s_{OB}=\text{const}} - \tan\alpha \frac{\partial s_{OB}}{\partial \varepsilon} \quad . \tag{5.117}$$

5.3.4 Wrapping path from O to B for stretched curved muscle

Analogously to Section **5.2.1**, perturbation theory is used to determine $\partial s_{OB}/\partial \varepsilon$. Thus, the differential equation

$$\frac{\partial s}{\partial \sigma} = \frac{\rho(\sigma) \, \cos\left(\alpha \left(s \left(\varepsilon\right)\right)\right) + b \left(s \left(\varepsilon\right)\right)}{1 + b \left(s \left(\varepsilon\right)\right) \frac{\partial \alpha}{\partial s}} \frac{\mathrm{d}\varphi}{\mathrm{d}\sigma} \tag{5.118}$$

$$= f(s, \sigma, \varepsilon) \tag{5.119}$$

is solved using first-order perturbation theory where a change in the longitudinal strain is interpreted as a small perturbation $\mathrm{d}\varepsilon$ leading to

$$s(\sigma; \mathrm{d}\varepsilon) = s_1(\sigma) + s_2(\sigma)\,\mathrm{d}\varepsilon \quad . \tag{5.120}$$

Applying that to the differential equation yields

$$\begin{aligned}
\frac{\mathrm{d}s_1}{\mathrm{d}\sigma} + \mathrm{d}\varepsilon\,\frac{\mathrm{d}s_2}{\mathrm{d}\sigma} &= f(s_1 + \mathrm{d}\varepsilon\,s_2, \sigma, \varepsilon + \mathrm{d}\varepsilon) \\
&= f(s_1, \sigma, \varepsilon) + \left.\frac{\mathrm{d}f}{\mathrm{d}s}\right|_{\varepsilon=\mathrm{const}} s_2\,\mathrm{d}\varepsilon + \left.\frac{\mathrm{d}f}{\mathrm{d}\varepsilon}\right|_{s=\mathrm{const}} \mathrm{d}\varepsilon \\
&= f(s_1, \sigma, \varepsilon) + \left(\left.\frac{\mathrm{d}f}{\mathrm{d}s}\right|_{\varepsilon=\mathrm{const}} s_2 + \left.\frac{\mathrm{d}f}{\mathrm{d}\varepsilon}\right|_{s=\mathrm{const}}\right)\mathrm{d}\varepsilon
\end{aligned} \tag{5.121}$$

and equating the coefficients with respect to $\mathrm{d}\varepsilon$ leads to the system of linear differential equations

$$\begin{aligned}
\frac{\mathrm{d}s_1}{\mathrm{d}\sigma} &= f(s_1, \sigma, \varepsilon) \\
\frac{\mathrm{d}s_2}{\mathrm{d}\sigma} &= \left.\frac{\mathrm{d}f}{\mathrm{d}s}\right|_{\varepsilon=\mathrm{const}} s_2 + \left.\frac{\mathrm{d}f}{\mathrm{d}\varepsilon}\right|_{s=\mathrm{const}}
\end{aligned} \tag{5.122}$$

with

$$\frac{\mathrm{d}f}{\mathrm{d}s} = \frac{\tan\alpha - 2\,\rho\sin\alpha\frac{\partial\alpha}{\partial s} - b\left[\rho\sin\alpha\left(\frac{\partial\alpha}{\partial s}\right)^2 + (\rho\cos\alpha + b)\frac{\partial^2\alpha}{\partial s^2}\right]}{\left(1 + b\frac{\partial\alpha}{\partial s}\right)^2} \tag{5.123}$$

$$\frac{\mathrm{d}f}{\mathrm{d}\varepsilon} = \frac{\left(-\rho\sin\alpha\frac{\partial\alpha}{\partial\varepsilon} + \frac{\partial b}{\partial\varepsilon}\right)\left(1 + b\frac{\partial\alpha}{\partial s}\right) - (\rho\cos\alpha + b)\left(\frac{\partial b}{\partial\varepsilon}\frac{\partial\alpha}{\partial s} + b\frac{\partial^2\alpha}{\partial s\,\partial\varepsilon}\right)}{\left(1 + b\frac{\partial\alpha}{\partial s}\right)^2} \tag{5.124}$$

that have to be solved for the interval $[\sigma_A, \sigma_B]$ to obtain

$$s_1 \,\widehat{=}\, s_{OB} \qquad \text{and} \tag{5.125}$$

$$s_2 \,\widehat{=}\, \frac{\partial s_{OB}}{\partial\varepsilon} = \kappa_{OB}^{\varepsilon} \tag{5.126}$$
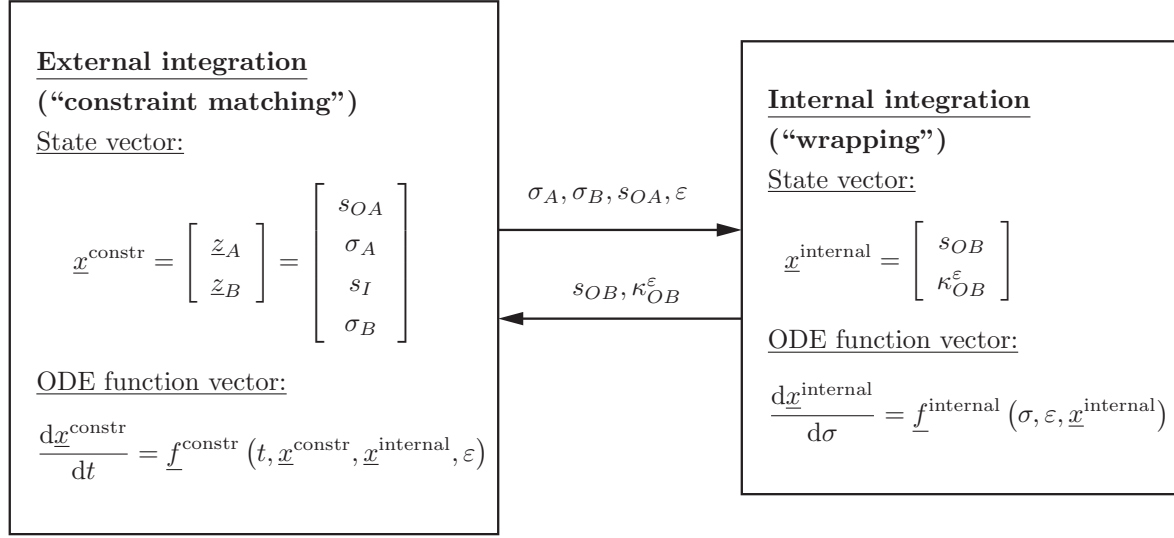
for initial values

$$s(\sigma_A) = s_{OA} \tag{5.127}$$

$$\kappa_{OB}^{\varepsilon} = \frac{\partial s_{OA}}{\partial\varepsilon} \quad . \tag{5.128}$$

5.4 Algorithm

In summary, the presented algorithm consists of two nested integrations, as illustrated in Fig. 5.7. In the external integration, the constraint matching takes place, where the

Figure 5.7: Algorithm consisting of external and internal integration

implicit velocity constraints at A and B are solved for derivatives of the state vectors with respect to time t, $\dot{\underline{z}}_A$ and $\dot{\underline{z}}_B$, as

$$\frac{\mathrm{d}\underline{x}^{\text{constr}}}{\mathrm{d}t} = \begin{bmatrix} \dot{\underline{z}}_A \\ \dot{\underline{z}}_B \end{bmatrix} = \begin{bmatrix} \mathrm{d}s^{\varepsilon}_{OA} \\ \mathrm{d}\sigma^{\varepsilon}_A \\ \mathrm{d}s^{\varepsilon}_I \\ \mathrm{d}\sigma^{\varepsilon}_B \end{bmatrix} = \begin{bmatrix} -\mathrm{J}_A^{-1} \dfrac{\partial \underline{g}_A}{\partial \varepsilon} \\[2mm] -\mathrm{J}_B^{-1} \dfrac{\partial \underline{g}_B}{\partial \varepsilon} \end{bmatrix} \dot{\varepsilon} \quad . \tag{5.129}$$

Additionally, an internal integration is necessary to compute s_{OB} and $\kappa^{\varepsilon}_{OB}$. Therefore, the coupled ODE

$$\frac{\mathrm{d}\underline{x}^{\text{internal}}}{\mathrm{d}\sigma} = \frac{\mathrm{d}}{\mathrm{d}\sigma} \begin{bmatrix} s \\ \kappa^{\varepsilon}_{OB} \end{bmatrix} = \begin{bmatrix} f(s,\sigma,\varepsilon) \\ \left.\dfrac{\partial f}{\partial s}\right|_{\varepsilon=\text{const}} \dfrac{\partial s}{\partial \varepsilon} + \left.\dfrac{\partial f}{\partial \varepsilon}\right|_{s=\text{const}} \end{bmatrix} \tag{5.130}$$

with

$$f(s,\sigma,\varepsilon) = \frac{\partial s}{\partial \sigma} = \frac{\rho(\sigma)\,\cos\left(\alpha\left(s,\varepsilon\right)\right) + b\left(s,\varepsilon\right)}{1 + b\left(s,\varepsilon\right)\frac{\partial \alpha}{\partial s}} \; \frac{\mathrm{d}\varphi}{\mathrm{d}\sigma} \tag{5.131}$$

is solved for the interval $[\sigma_A, \sigma_B]$ with the initial conditions

$$\underline{x}^{\text{internal}}_0 = \begin{bmatrix} s_{OA} \\ \dfrac{\partial s_{OA}}{\partial \varepsilon} - \left.\dfrac{\partial s}{\partial \sigma}\right|_A \dfrac{\partial \sigma_A}{\partial \varepsilon} \end{bmatrix} \quad . \tag{5.132}$$

5.5 Computational results

For a comparison regarding computation time and accuracy, the presented approach
was applied to the example of a curved muscle like presented in Section **5.3.1** for
the dimensionless parameters $\ell_0 = 15.0$, $b_E^0 = 1.058$, $\lambda = 0.65$ and $\nu = 0.5$ of the
unstretched muscle that is wrapping on an ellipsoidal surface curve with its center at
the origin of the coordinate system and the dimensionless semiaxis lengths $a_1 = 4.2$
and $a_2 = 3.0$. Point O is fixed at $(4.66, 3.91)$ while point I starts at $(-4.99, -3.65)$ for
$\varepsilon_0 = 0$ and can slide vertically so that the boundary constraints are fulfilled for any ε.

The presented method was implemented in Matlab using the Runge-Kutta routine
ode45 for integration of the velocity constraints in the range $[\varepsilon_0, \varepsilon_E]$ and compared
with iterations at position level using equidistant Newton steps (Table 5.1). The start
and the end configuration are illustrated in Fig. 5.8. The computations were performed
on a processor Intel(R) Core(TM) i7-10850H CPU @ 2.70GHz. One can recognize that
the integration method is more than twice as fast with respect to the iteration method,
with still excellent accuracy at the end of the integration.

In order to be able to better classify the results, it should be regarded that even the
position-level iterations provide a significant improvement in terms of accuracy and
computation times compared to the bead-chain discretization. Due to the increasing
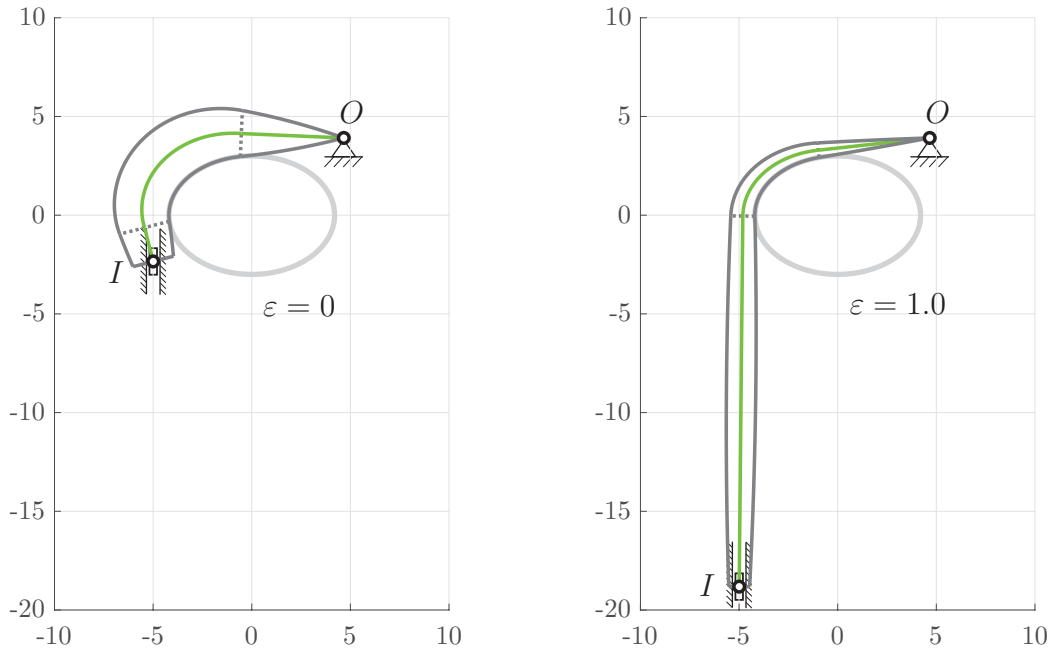
Figure 5.8: Start and end configuration

Table 5.1: Computational results

Model and numeric parameters					
ε_0	ε_E	$\Delta\varepsilon$	tolNewton	tolODErel	tolODEabs
0.0	1.0	0.01	10^{-8}	10^{-8}	10^{-8}

Method	Computation time [s]	Accuracy
Integration	0.5800	1.4e-08
Iteration	1.1378	-4.9e-11

complexity in the implementation of the bead-chain method no comparisons were carried out with respect to this method due to the immense effort to implement beads in contact with the surface and their positions for the general case of stretching.

6 The general planar case: Stretching and sliding

In the final step, the method derived in Chapter **4** for shifting an inextensible thick muscle strand is merged with the method derived in Chapter **5** for stretching a thick muscle with one free end and one fixed end with the goal of enabling stretching and sliding of a thick muscle with two free ends. The crucial point will be to combine displacement and elongation, which requires corresponding splitting of velocities at end A.

The chapter is again structured to start with the simplest case, a cone wrapping around a circle ($\alpha = \text{const}, \rho = \text{const}$), and successively increasing the complexity, first to general surfaces with non-constant curvature ($\rho \neq \text{const}$) and finally to general muscles with variable conicity ($\alpha \neq \text{const}$).

6.1 Case 1: Stretching and sliding of cone on circle

The first example case of a cone wrapping and sliding on a circle is almost identical to the one presented in Section **5.1** with the only difference that now end O is freely movable instead of fixed. As shown in Fig. 6.1, a prismatic joint is exemplarily introduced at O for this purpose, with the free direction of motion specified by the unit vector $\underline{u}_O$ and with the joint variable s_O for the actual motion. Thus, analogously to endpoint I it holds for O

$$\underline{r}_O = \underline{r}_{O,0} + \underline{u}_O\, s_O \quad . \tag{6.1}$$

At point A, this leads to the constraint equations

$$g_{1A} = \qquad s_{OA} - \rho\, \sin\alpha(\varepsilon) + \underline{r}_O(s_O) \cdot \underline{e}_C(\varphi_A, \varepsilon) = 0 \tag{6.2}$$

$$g_{2A} = \tan\alpha(\varepsilon)\, s_{OA} + \rho\, \cos\alpha(\varepsilon) - \underline{r}_O(s_O) \cdot \underline{e}_C^{\perp}(\varphi_A, \varepsilon) = 0 \tag{6.3}$$

now additionally depending on s_O. Neither the Jacobian $J_A = \partial\underline{g}_A/\partial\underline{z}_A$ nor the derivative with respect to the longitudinal strain $\partial\underline{g}_A/\partial\varepsilon$ depend on s_O and, thus, can be calculated as derived in Section **5.1**. On the other hand, the total change of the state variables

$$\underline{z}_A = \begin{bmatrix} s_{OA} \\ \varphi_A \end{bmatrix} \tag{6.4}$$
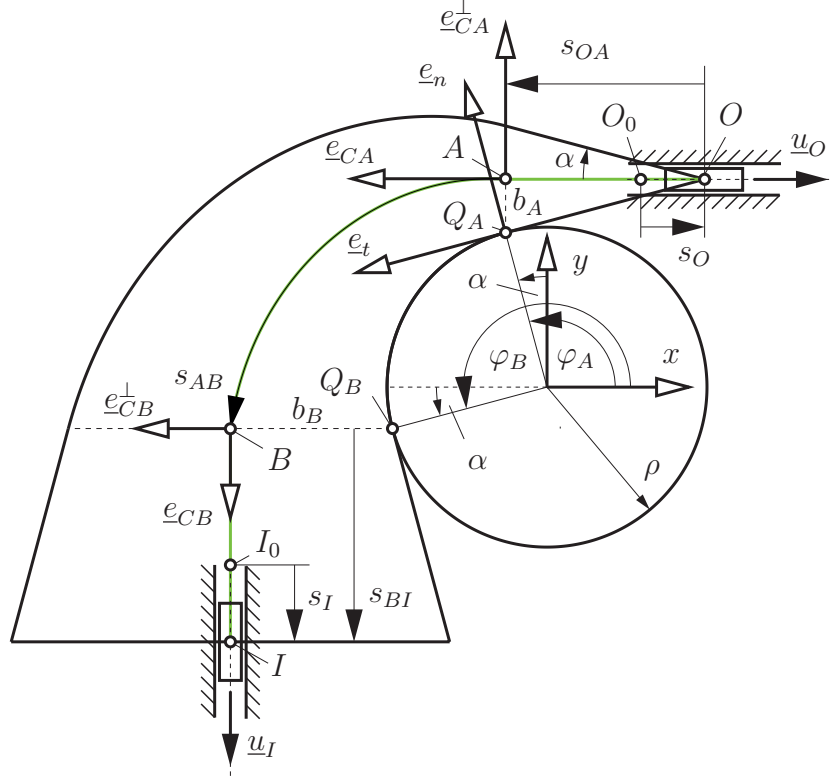
Figure 6.1: Case 1: Cone stretching and sliding over circle

does depend on the motion s_O and results from the superposition of the effects due to strain $(\mathrm{d}\underline{z}_A^\varepsilon)$ and displacement $(\mathrm{d}\underline{z}_A^{\mathrm{v}})$ as

$$\dot{\underline{z}}_A = -\mathrm{J}_A^{-1}\, \frac{\partial \underline{g}_A}{\partial \varepsilon}\, \dot{\varepsilon} - \mathrm{J}_A^{-1}\, \frac{\partial \underline{g}_A}{\partial s_O}\, \dot{s}_O$$

$$= \quad \mathrm{d}\underline{z}_A^\varepsilon \qquad + \quad \mathrm{d}\underline{z}_A^{\mathrm{v}} \tag{6.5}$$

with

$$\frac{\partial \underline{g}_A}{\partial s_O} = \begin{bmatrix} \underline{u}_O \cdot \underline{e}_{CA} \\ -\underline{u}_O \cdot \underline{e}_{CA}^\perp \end{bmatrix} \quad \text{and} \quad \mathrm{d}\underline{z}_A^{\mathrm{v}} = \begin{bmatrix} \mathrm{d}s_{OA}^{\mathrm{v}} \\ \mathrm{d}\varphi_A^{\mathrm{v}} \end{bmatrix} . \tag{6.6}$$

Note that with $\partial \underline{g}_A / \partial s_O$ the velocity of the point O is again split into two components,

$$v_O^\parallel = \underline{u}_O \cdot \underline{e}_{CA}\, \dot{s}_O \qquad \text{and} \qquad v_O^\perp = \underline{u}_O \cdot \underline{e}_{CA}^\perp\, \dot{s}_O \ , \tag{6.7}$$

as in Chapter **4**.

At end B, the constraints are such as in Chapter **5**

$$g_{1B} = \underline{r}_I \cdot \underline{e}_C(\varphi_B, \varepsilon) - \rho\, \sin\alpha(\varepsilon) + \qquad\quad s_{OB}(\varepsilon, s_O) - \ell(\varepsilon) = 0 \tag{6.8}$$

$$g_{2B} = \underline{r}_I \cdot \underline{e}_C^\perp(\varphi_B, \varepsilon) - \rho\, \cos\alpha(\varepsilon) - \tan\alpha(\varepsilon)\, s_{OB}(\varepsilon, s_O) \qquad = 0 \tag{6.9}$$

with the only difference that the length of the centerline s_{OB} from O to B now also depends on the location of the point O.

Hence, the total change in the state variables at the left end B,

$$\underline{z}_B = \begin{bmatrix} s_I \\ \varphi_B \end{bmatrix} , \qquad (6.10)$$

results again from the superposition of the effects due to strain and displacement:

$$\dot{\underline{z}}_B = -\mathrm{J}_B^{-1} \left(\frac{\partial \underline{g}_B}{\partial \varepsilon} \dot{\varepsilon} + \frac{\partial \underline{g}_B}{\partial s_O} \dot{s}_O \right) \qquad (6.11)$$

with

$$\frac{\partial \underline{g}_B}{\partial s_O} = \begin{bmatrix} \dfrac{\partial s_{OB}}{\partial s_O} \\[2mm] -\tan\alpha \, \dfrac{\partial s_{OB}}{\partial s_O} \end{bmatrix} . \qquad (6.12)$$

To determine how s_{OB} changes for a change in s_O, it is necessary to examine the changes at end A more precisely, because pure wrapping at A does not affect the length s_{OB}. Instead, it is the "pull" component that has an effect on s_{OB} and its magnitude must be determined.

For the actual case of a cone-shaped muscle wrapping over a circular surface, Fig. 6.2 illustrates what happens at end A for a displacement of $\mathrm{d}s_O$ of point O, without considering any elongation or compression (see also Section **4.3.5**). Shown in gray is the muscle in its initial position, with Q_A as the contact point with the surface at the surface coordinate φ_A and with the corresponding point A on the centerline at the transition between the wrapped segment and the free end. Pulling the point O by $\mathrm{d}s_O$ in the direction of $\underline{u}_O$ leads to the new position of the muscle marked in black with the new cross-sectional point A'. In this process, two effects superpose:

(a) First, at the original contact point Q_A, the point A'' is pulled to the position A''', where due to the cone shape the inclination of the cross-sectional area remains the same. Thus, the length of the free segment s_{OA} increases by $\mathrm{d}s_{OA}^{\mathrm{pull}}$, which in the initial muscle (gray) corresponds to the wrapping length between A and A'' with corresponding surface coordinate $\mathrm{d}\varphi_A^{\mathrm{pull}}$. This effect is called again the "pull" component.

(b) Secondly, the muscle is wrapped due to the orthogonal movement of the endpoint O by the angle $-\mathrm{d}\varphi_A^{\mathrm{v}}$, leading to the new contact point Q_A' and a decrease of the

Figure 6.2: Case 1: Pulled cone shaped muscle on circle – end A

length of the free segment s_{OA} by $-(\rho \cos\alpha + b_A)\, d\varphi_A^{\mathrm{v}}$. This effect is called again the "wrap" component.

Thus, the change ds_{OA}^{pull} of the centerline due to the pulling results as

$$
ds_{OA}^{\mathrm{pull}} = ds_{OA}^{\mathrm{v}} - (\rho \cos\alpha + b_A)\, d\varphi_A^{\mathrm{v}}
$$

$$
= ds_{OA}^{\mathrm{v}} - \left.\frac{\partial s}{\partial \varphi}\right|_A \cdot d\varphi_A^{\mathrm{v}} \quad . \tag{6.13}
$$

From this, the change $d\varphi_A^{\mathrm{pull}}$ in surface coordinate caused only by the "pulling" can be determined as

$$
d\varphi_A^{\mathrm{pull}} = \frac{ds_{OA}^{\mathrm{pull}}}{\rho \cos\alpha + b_A} = \frac{ds_{OA}^{\mathrm{v}}}{\rho \cos\alpha + b_A} - d\varphi_A^{\mathrm{v}} \quad . \tag{6.14}
$$

Only this component is transferred to end B by means of the velocity transmission derived in Section **3.3**. As derived in Section **3.3.3**, for the case of a surface with a

constant radius of curvature, the velocity is transmitted in a ratio of $1:1$ and it follows that $\mathrm{d}\varphi_B^{\mathrm{pull}} = \mathrm{d}\varphi_A^{\mathrm{pull}}$, which finally leads to

$$\mathrm{d}s_{OB}^{\mathrm{pull}} = \frac{\partial s_{OB}}{\partial s_O}\,\dot{s}_O = (\rho\,\cos\alpha + b_B)\,\mathrm{d}\varphi_B^{\mathrm{pull}} \quad . \tag{6.15}$$

With this, simultaneous stretching and sliding results in

$$\dot{\underline{z}}_B = -\mathrm{J}_B^{-1}\left(\frac{\partial \underline{g}_B}{\partial \varepsilon}\,\dot{\varepsilon} + \begin{bmatrix} \mathrm{d}s_{OB}^{\mathrm{pull}} \\ -\tan\alpha\,\mathrm{d}s_{OB}^{\mathrm{pull}} \end{bmatrix}\right) \tag{6.16}$$

for the state variables at end B.

6.2   Case 2: Stretching and sliding of cone on ellipse

Taking into account a variable radius of curvature for the surface, as shown in Fig. 6.3 for a cone wrapping over an ellipse, one can proceed analogously to Section **6.1**. Only the determination of $\mathrm{d}s_{OB}^{\mathrm{pull}}$ must now take into account the complete velocity transmission of Section **3.3.2**.

Compared to Section **5.2**, the constraint equations are now also dependent on the position s_O of the point O, leading to

$$g_{1A} = \qquad s_{OA} - \left[\underline{r}_Q(\sigma_A) - \underline{r}_O(s_O)\right] \cdot \underline{e}_C(\sigma_A, \varepsilon) = 0 \tag{6.17}$$

$$g_{2A} = \tan\alpha(\varepsilon)\,s_{OA} + \left[\underline{r}_Q(\sigma_A) - \underline{r}_O(s_O)\right] \cdot \underline{e}_C^{\perp}(\sigma_A, \varepsilon) = 0 \tag{6.18}$$

at end A and

$$g_{1B} = \left[\underline{r}_I - \underline{r}_Q(\sigma_B)\right] \cdot \underline{e}_C(\sigma_B, \varepsilon) + \qquad s_{OB}(\varepsilon, s_O) - \ell(\varepsilon) = 0 \tag{6.19}$$

$$g_{2B} = \left[\underline{r}_I - \underline{r}_Q(\sigma_B)\right] \cdot \underline{e}_C^{\perp}(\sigma_B, \varepsilon) - \tan\alpha(\varepsilon)\,s_{OB}(\varepsilon, s_O) \qquad = 0 \tag{6.20}$$
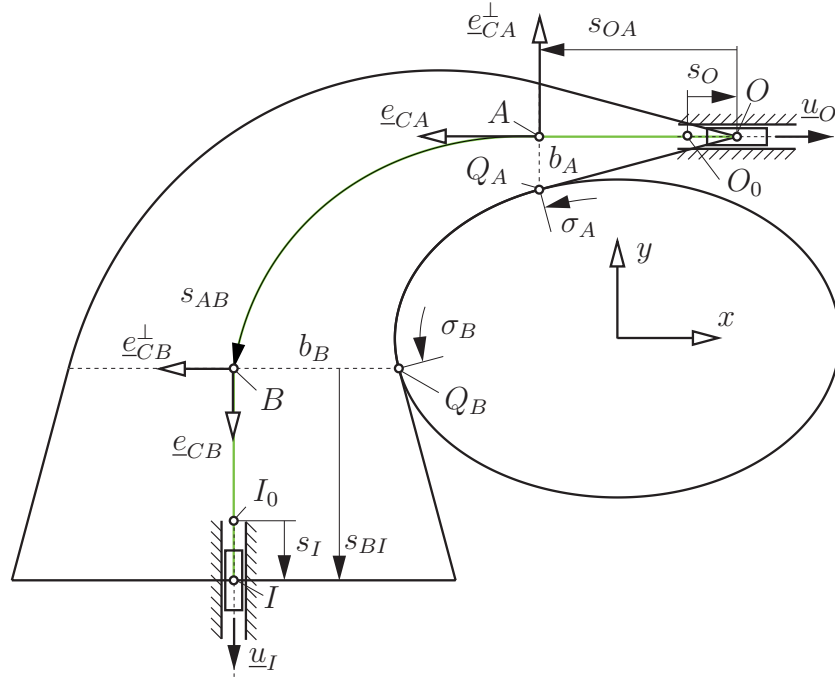
at end B. Analogously to the derivation in Section **6.1**, the changes in the state variables

$$\underline{z}_A = \begin{bmatrix} s_{OA} \\ \sigma_A \end{bmatrix} \quad \text{and} \quad \underline{z}_B = \begin{bmatrix} s_I \\ \sigma_B \end{bmatrix} \quad , \tag{6.21}$$

can now be calculated by means of superposition as

$$\dot{\underline{z}}_A = -\mathrm{J}_A^{-1}\left(\frac{\partial \underline{g}_A}{\partial \varepsilon}\,\dot{\varepsilon} + \begin{bmatrix} v_O^{\|} \\ -v_O^{\perp} \end{bmatrix}\right) \tag{6.22}$$

$$\dot{\underline{z}}_B = -\mathrm{J}_B^{-1}\left(\frac{\partial \underline{g}_B}{\partial \varepsilon}\,\dot{\varepsilon} + \begin{bmatrix} \mathrm{d}s_{OB}^{\mathrm{pull}} \\ -\tan\alpha\,\mathrm{d}s_{OB}^{\mathrm{pull}} \end{bmatrix}\right) \tag{6.23}$$

Figure 6.3: Case 2: Cone stretching and sliding over ellipse

with

$$v_O^{\parallel} = \underline{u}_O \cdot \underline{e}_{CA}\, \dot{s}_O \qquad \text{and} \qquad v_O^{\perp} = \underline{u}_O \cdot \underline{e}_{CA}^{\perp}\, \dot{s}_O \qquad (6.24)$$

and the Jacobians $J_A = \partial \underline{g}_A / \partial \underline{z}_A$ and $J_B = \partial \underline{g}_B / \partial \underline{z}_B$ as well as the derivatives with respect to ε, $\partial \underline{g}_A / \partial \varepsilon$ and $\partial \underline{g}_B / \partial \varepsilon$, calculated as in Section **5.2**.

For the determination of $\mathrm{d}s_{OB}^{\mathrm{pull}}$, again the "pull" component of the velocity transmission needs to be computed. At end A, this can be calculated identically to the previous section by first considering the displacement of the endpoint O separately
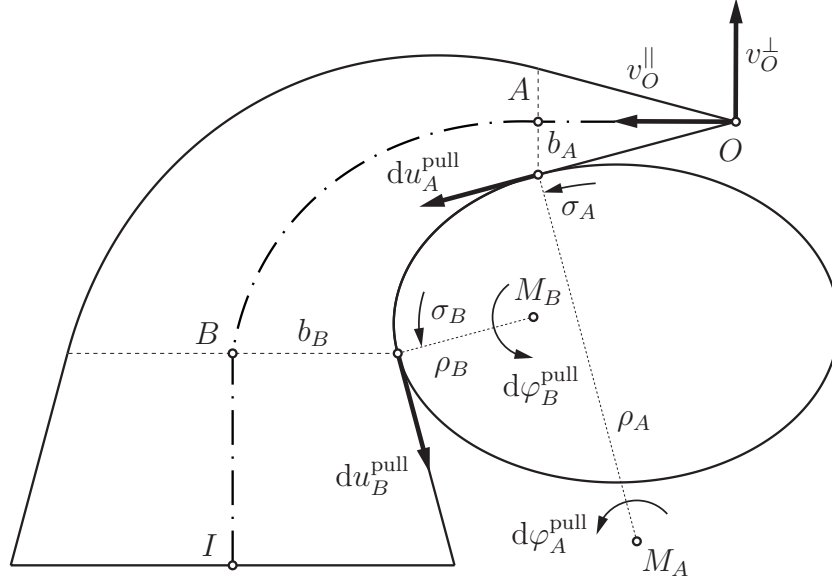
$$\mathrm{d}\underline{z}_A^{\mathrm{v}} = \begin{bmatrix} \mathrm{d}s_{OA}^{\mathrm{v}} \\ \mathrm{d}\sigma_A^{\mathrm{v}} \end{bmatrix} = -J_A^{-1} \left(\begin{bmatrix} v_O^{\parallel} \\ -v_O^{\perp} \end{bmatrix} \right) \quad . \qquad (6.25)$$

and then subtracting from it the part that leads to the wrapping or unwrapping of the muscle

$$\mathrm{d}s_{OA}^{\mathrm{pull}} = \mathrm{d}s_{OA}^{\mathrm{v}} - (\rho\, \cos\alpha + b_A)\, \mathrm{d}\varphi_A^{\mathrm{v}} \qquad (6.26)$$

with

$$\mathrm{d}\varphi_A^{\mathrm{v}} = \mathrm{d}\sigma_A^{\mathrm{v}} \left.\frac{\mathrm{d}\varphi}{\mathrm{d}\sigma}\right|_A \quad . \qquad (6.27)$$

Figure 6.4: Case 2: Velocity transmission from A to B

From ds_{OA}^{pull}, again, the infinitesimal rotation caused by the pulling $d\varphi_A^{\mathrm{pull}}$ around the center of curvature M can be calculated as

$$d\varphi_A^{\mathrm{pull}} = \frac{ds_{OA}^{\mathrm{pull}}}{\rho \, \cos\alpha + b_A} = \frac{ds_{OA}^{\mathrm{v}}}{\rho \, \cos\alpha + b_A} - d\varphi_A^{\mathrm{v}} \quad . \tag{6.28}$$

For the velocity transmission to B, one has according to Section **3.3**, Eq. (3.53),

$$\frac{\dot{u}_B}{\dot{u}_A} = e^{\kappa_{AB}^{\mathrm{v}}} = \exp\left(\int_{\sigma_A}^{\sigma_B} \frac{b}{\rho \, [\, \rho \, \cos\alpha + b \,]} \, \frac{d\rho}{d\sigma} \, d\sigma \right) \tag{6.29}$$

with the relationship $b = r \, \cos\alpha$ between the half-thickness b and the bead radius r already inserted. It follows

$$du_B^{\mathrm{pull}} = e^{\kappa_{AB}^{\mathrm{v}}} \, du_A^{\mathrm{pull}} \tag{6.30}$$

or in terms of infinitesimal rotations $d\varphi$ around the center of curvature M (see Fig. 6.4)

$$\rho_B \, d\varphi_B^{\mathrm{pull}} = e^{\kappa_{AB}^{\mathrm{v}}} \, \rho_A \, d\varphi_A^{\mathrm{pull}}$$
$$\Leftrightarrow d\varphi_B^{\mathrm{pull}} = e^{\kappa_{AB}^{\mathrm{v}}} \, \frac{\rho_A}{\rho_B} \, d\varphi_A^{\mathrm{pull}} \quad , \tag{6.31}$$

from which ds_{OB}^{pull} can be calculated as

$$ds_{OB}^{\mathrm{pull}} = (\rho_B \, \cos\alpha + b_B) \, d\varphi_B^{\mathrm{pull}} \quad . \tag{6.32}$$

6.3 Case 3: Stretching and sliding of curved muscle on ellipse

For the general case of muscles with variable half opening angle (i.e. $\alpha \neq$ const) like illustrated in Fig. 6.5, the explicit function for calculating the muscle's half-thickness (in Section **6.3** described as $b = s \tan\alpha$) has now to be replaced by the more general formulation $b = b(s)$. At end A, this leads to

$$g_{1A} = \quad s_{OA} - \left[\underline{r}_Q(\sigma_A) - \underline{r}_O(s_O)\right] \cdot \underline{e}_C(\sigma_A, s_{OA}, \varepsilon) = 0 \tag{6.33}$$

$$g_{2A} = b(s_{OA}) + \left[\underline{r}_Q(\sigma_A) - \underline{r}_O(s_O)\right] \cdot \underline{e}_C^{\perp}(\sigma_A, s_{OA}, \varepsilon) = 0 \quad . \tag{6.34}$$

At end B, however, since α varies along the length s of the muscle, the inclination of the cross-sectional area at B also depends on s_O. This must be taken into account when differentiating the constraint equations

$$g_{1B} = \left[\underline{r}_I - \underline{r}_Q(\sigma_B)\right] \cdot \underline{e}_C(\sigma_B, s_{OB}, \varepsilon, s_O) + \quad s_{OB}(\varepsilon, s_O) - \ell(\varepsilon) = 0 \tag{6.35}$$

$$g_{2B} = \left[\underline{r}_I - \underline{r}_Q(\sigma_B)\right] \cdot \underline{e}_C^{\perp}(\sigma_B, s_{OB}, \varepsilon, s_O) - b(s_{OB}, \varepsilon, s_O) \quad\quad = 0 \tag{6.36}$$

with respect to s_O. Thus, for the calculation of the changes of the state variables

$$\underline{z}_A = \begin{bmatrix} s_{OA} \\ \sigma_A \end{bmatrix} \quad \text{and} \quad \underline{z}_B = \begin{bmatrix} s_I \\ \sigma_B \end{bmatrix} \quad , \tag{6.37}$$
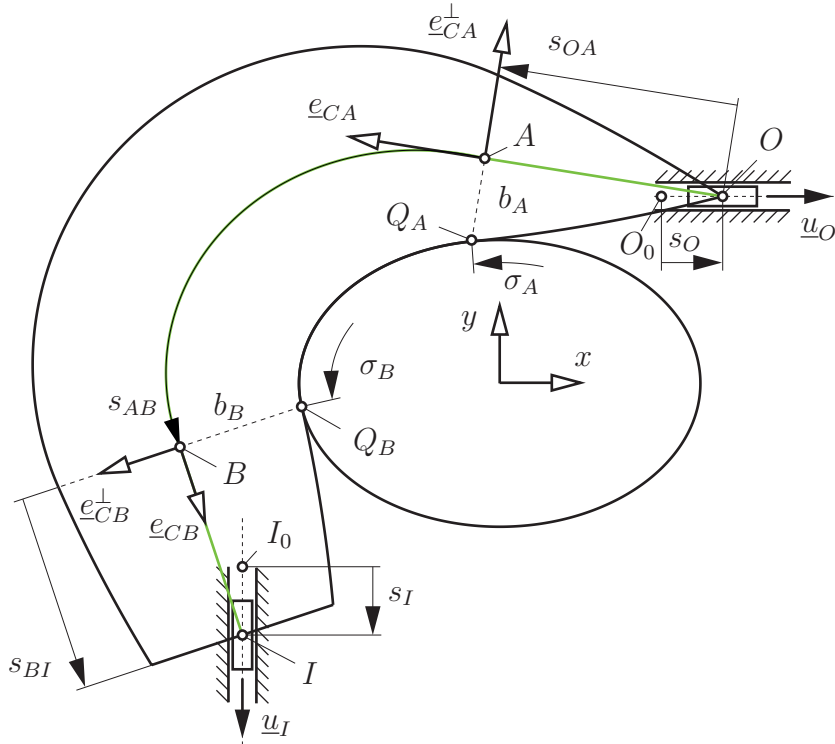
Figure 6.5: Case 3: Curved muscle stretching and sliding over ellipse

the following equations result from superposition

$$\dot{\underline{z}}_A = -\mathrm{J}_A^{-1} \left(\frac{\partial \underline{g}_A}{\partial \varepsilon} \dot{\varepsilon} + \begin{bmatrix} v_O^{\parallel} \\ -v_O^{\perp} \end{bmatrix} \right) \tag{6.38}$$

$$\dot{\underline{z}}_B = -\mathrm{J}_B^{-1} \left(\frac{\partial \underline{g}_B}{\partial \varepsilon} \dot{\varepsilon} + \begin{bmatrix} \mathrm{d}s_{OB}^{\mathrm{pull}} & + (\underline{r}_{QBI} \cdot \underline{e}_{CB}^{\perp}) \left. \frac{\partial \alpha}{\partial s} \right|_B \mathrm{d}s_{OB}^{\mathrm{pull}} \\ -\tan\alpha \, \mathrm{d}s_{OB}^{\mathrm{pull}} & - (\underline{r}_{QBI} \cdot \underline{e}_{CB}) \left. \frac{\partial \alpha}{\partial s} \right|_B \mathrm{d}s_{OB}^{\mathrm{pull}} \end{bmatrix} \right) . \tag{6.39}$$

While the Jacobians $\mathrm{J}_A = \partial \underline{g}_A / \partial \underline{z}_A$ and $\mathrm{J}_B = \partial \underline{g}_B / \partial \underline{z}_B$, as well as the derivatives with respect to ε, $\partial \underline{g}_A / \partial \varepsilon$ and $\partial \underline{g}_B / \partial \varepsilon$, can be calculated like derived in Section **5.3**, $\mathrm{d}s_{OB}^{\mathrm{pull}}$ results analogous to Section **6.2** by separately considering the pure pull components from

$$\mathrm{d}\underline{z}_A^{\mathrm{v}} = \begin{bmatrix} \mathrm{d}s_{OA}^{\mathrm{v}} \\ \mathrm{d}\sigma_A^{\mathrm{v}} \end{bmatrix} = -\mathrm{J}_A^{-1} \left(\begin{bmatrix} v_O^{\parallel} \\ -v_O^{\perp} \end{bmatrix} \right) . \tag{6.40}$$

For the pull component $\mathrm{d}s_{OA}^{\mathrm{pull}}$ at A, it holds again

$$\mathrm{d}s_{OA}^{\mathrm{pull}} = \mathrm{d}s_{OA}^{\mathrm{v}} - \left. \frac{\partial s}{\partial \varphi} \right|_A \mathrm{d}\varphi_A^{\mathrm{v}} \tag{6.41}$$

with

$$\mathrm{d}\varphi_A^{\mathrm{v}} = \mathrm{d}\sigma_A^{\mathrm{v}} \left. \frac{\mathrm{d}\varphi}{\mathrm{d}\sigma} \right|_A , \tag{6.42}$$

and

$$\frac{\partial s}{\partial \varphi} = \frac{\rho(\sigma) \, \cos\alpha(s) + b(s)}{1 + b(s) \dfrac{\partial \alpha}{\partial s}} . \tag{6.43}$$

From this, the velocity transmission from A to B, can be determined analogously to Section **6.2** as

$$\mathrm{d}s_{OB}^{\mathrm{pull}} = e^{\kappa_{AB}^{\mathrm{v}}} \frac{\rho_A}{\rho_B} \frac{\left. \frac{\partial s}{\partial \varphi} \right|_B}{\left. \frac{\partial s}{\partial \varphi} \right|_A} \mathrm{d}s_{OA}^{\mathrm{pull}} . \tag{6.44}$$

6.4   Algorithm

In summary, the presented algorithm consists again as in Chapter **5** of two nested integrations (Fig. 6.6). The external integration concerns the satisfaction of the constraint equations at the segment transitions between wrapped segment and undeformed free
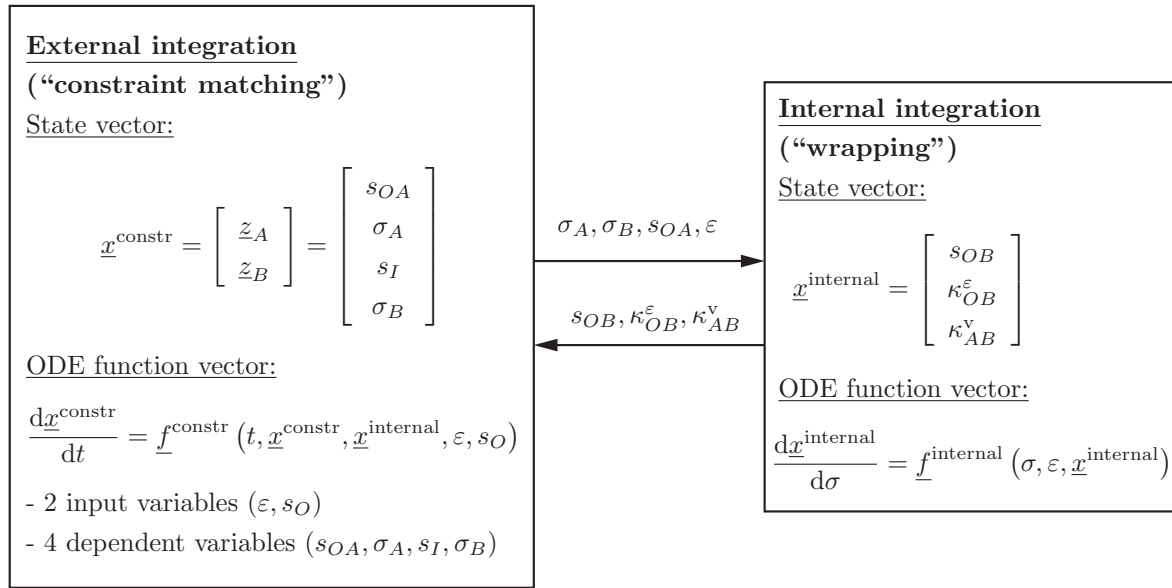
Figure 6.6: Algorithm consisting of external and internal integration

end straight line segments, where the implicit velocity constraints at A and B are solved for derivatives of the state vectors with respect to time t, $\dot{\underline{z}}_A$ and $\dot{\underline{z}}_B$, as

$$\frac{\mathrm{d}\underline{x}^{\mathrm{constr}}}{\mathrm{d}t} = \begin{bmatrix} \dot{\underline{z}}_A \\ \dot{\underline{z}}_B \end{bmatrix} = \begin{bmatrix} \mathrm{d}s^{\varepsilon}_{OA} & + & \mathrm{d}s^{\mathrm{v}}_{OA} \\ \mathrm{d}\sigma^{\varepsilon}_A & + & \mathrm{d}\sigma^{\mathrm{v}}_A \\ \mathrm{d}s^{\varepsilon}_I & + & \mathrm{d}s^{\mathrm{v}}_I \\ \mathrm{d}\sigma^{\varepsilon}_B & + & \mathrm{d}\sigma^{\mathrm{v}}_B \end{bmatrix} = \begin{bmatrix} -\mathrm{J}_A^{-1}\left(\dfrac{\partial \underline{g}_A}{\partial \varepsilon}\dot{\varepsilon} + \dfrac{\partial \underline{g}_A}{\partial s_O}\dot{s}_O\right) \\ -\mathrm{J}_B^{-1}\left(\dfrac{\partial \underline{g}_B}{\partial \varepsilon}\dot{\varepsilon} + \dfrac{\partial \underline{g}_B}{\partial s_O}\dot{s}_O\right) \end{bmatrix} .$$

$$(6.45)$$

Note that the selected state variables $(s_{OA}, \sigma_A, s_I, \sigma_B)$ can be exchanged by another choice involving the two input variables (ε, s_O). For instance, it is possible to define the movement of the endpoints O and I (by choosing s_O and s_I as input variables) and then to determine the resulting strain ε (together with $s_{OA}, \sigma_A, \sigma_B$) as a state variable via constraint matching.

The internal integration provides the required quantities transmitted along the wrapped segment that are necessary to formulate the constraint equations at B. As shown previously, they depend on the length of the wrapped centerline s_{OB}, on the length change with respect to ε introduced as $\kappa^{\varepsilon}_{OB} = \partial s_{OB}/\partial \varepsilon$ as well as on the length change of $\mathrm{d}s^{\mathrm{pull}}_{OB}$ due to sliding of the muscle with

$$\mathrm{d}s^{\mathrm{pull}}_{OB} = e^{\kappa^{\mathrm{v}}_{AB}}\,\frac{\rho_A}{\rho_B}\,\frac{\left.\frac{\partial s}{\partial \varphi}\right|_B}{\left.\frac{\partial s}{\partial \varphi}\right|_A}\left(\mathrm{d}s^{\mathrm{v}}_{OA} - \left.\frac{\partial s}{\partial \varphi}\right|_A \mathrm{d}\sigma^{\mathrm{v}}_A\,\left.\frac{\mathrm{d}\varphi}{\mathrm{d}\sigma}\right|_A\right) \quad . \qquad (6.46)$$

To determine these three quantities (s_{OB}, $\kappa^{\varepsilon}_{OB}$ and κ^{v}_{AB}), the coupled ODE

$$\frac{\mathrm{d}\underline{x}^{\mathrm{internal}}}{\mathrm{d}\sigma} = \frac{\mathrm{d}}{\mathrm{d}\sigma} \begin{bmatrix} s \\ \kappa^{\varepsilon}_{OB} \\ \kappa^{\mathrm{v}}_{AB} \end{bmatrix} = \begin{bmatrix} f(s,\sigma,\varepsilon) \\ \left.\frac{\partial f}{\partial s}\right|_{\varepsilon=\mathrm{const}} \frac{\partial s}{\partial\varepsilon} + \left.\frac{\partial f}{\partial\varepsilon}\right|_{s=\mathrm{const}} \\ h(s,\sigma,\varepsilon) \end{bmatrix} \tag{6.47}$$

with

$$f(s,\sigma,\varepsilon) = \frac{\partial s}{\partial\sigma} = \frac{\rho(\sigma)\,\cos\left(\alpha\left(s,\varepsilon\right)\right) + b\left(s,\varepsilon\right)}{1 + b\left(s,\varepsilon\right)\frac{\partial\alpha}{\partial s}}\,\frac{\mathrm{d}\varphi}{\mathrm{d}\sigma} \qquad \text{and} \tag{6.48}$$

$$h(s,\sigma,\varepsilon) = \frac{\partial\kappa^{\mathrm{v}}_{AB}}{\partial\sigma} = \frac{b(s,\varepsilon)}{\rho(\sigma)\left[\,\rho(\sigma)\,\cos\alpha(s,\varepsilon) + b(s,\varepsilon)\,\right]}\,\frac{\mathrm{d}\rho}{\mathrm{d}\sigma} \tag{6.49}$$

must be solved for the interval $[\sigma_A,\sigma_B]$ with the initial conditions

$$\underline{x}^{\mathrm{internal}}_0 = \begin{bmatrix} s_{OA} \\ \frac{\partial s_{OA}}{\partial\varepsilon} - \left.\frac{\partial s}{\partial\sigma}\right|_A \frac{\partial\sigma_A}{\partial\varepsilon} \\ 0 \end{bmatrix} \tag{6.50}$$

for each "external" step.

6.5   Computational results for the test case of Section 6.3

Analogously to Section **5.5**, the integration based, continuous approach presented here was applied to a curved muscle modeled like described in Section **5.3.1** for the dimensionless parameters $\ell_0 = 20.0$, $b^0_E = 3.5265$, $\lambda = 0.65$ and $\nu = 0.5$ of the unstretched muscle that is wrapping on an ellipsoidal surface curve with its center at the origin of the coordinate system and the dimensionless semiaxis lengths $a_1 = 4.2$ and $a_2 = 3.0$.

The velocity constraints were formulated with respect to ε as

$$\frac{\mathrm{d}\underline{x}^{\mathrm{constr}}}{\mathrm{d}\varepsilon} = \begin{bmatrix} \frac{\mathrm{d}\underline{z}_A}{\mathrm{d}\varepsilon} \\ \frac{\mathrm{d}\underline{z}_B}{\mathrm{d}\varepsilon} \end{bmatrix} = \begin{bmatrix} -\mathrm{J}^{-1}_A \left(\frac{\partial\underline{g}_A}{\partial\varepsilon} + \frac{\partial\underline{g}_A}{\partial s_O}\frac{\mathrm{d}s_O}{\mathrm{d}\varepsilon} \right)\mathrm{d}\varepsilon \\ -\mathrm{J}^{-1}_B \left(\frac{\partial\underline{g}_B}{\partial\varepsilon} + \frac{\partial\underline{g}_B}{\partial s_O}\frac{\mathrm{d}s_O}{\mathrm{d}\varepsilon} \right)\mathrm{d}\varepsilon \end{bmatrix} \tag{6.51}$$

and implemented in Matlab using the Runge-Kutta routine ode45 for integration in the range $[\varepsilon_0,\varepsilon_E]$, given in Table 6.1. Endpoint O, starting at $(4.66, 3.91)$, is supposed to move along a horizontal prismatic joint with the velocity $ds_O/d\varepsilon = 1.0$, while endpoint I, starting at $(-4.99, -6.71)$, is sliding along a vertical prismatic joint to fulfill the constraint equations. The initial and final configurations are shown in Fig. 6.7.
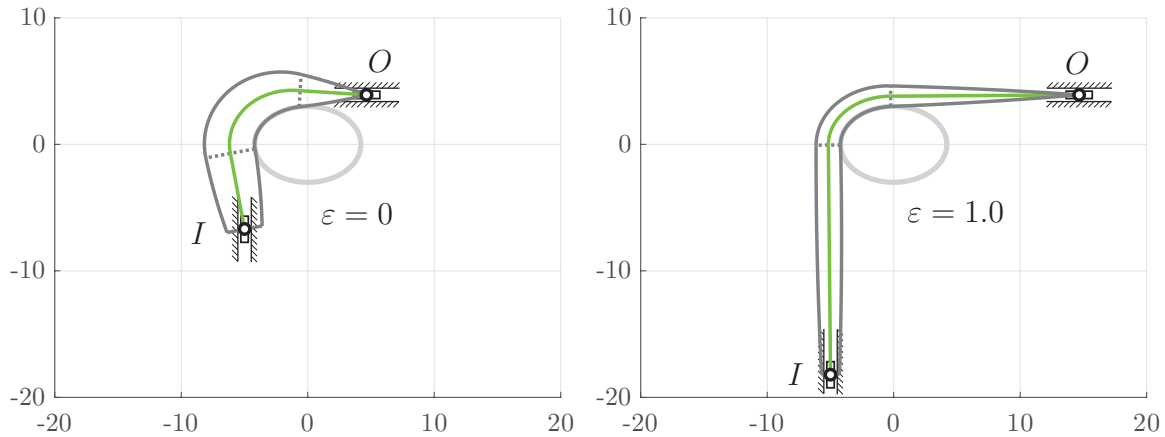
Figure 6.7: Start and end configuration

Table 6.1: Computational results

Model and numeric parameters						
ε_0	ε_E	$\Delta\varepsilon$	$\mathrm{d}s_O/\mathrm{d}\varepsilon$	tolNewton	tolODErel	tolODEabs
0.0	1.0	0.01	5.0	10^{-8}	10^{-8}	10^{-8}

Method	Computation time [s]	Accuracy
Integration	0.5655	4.9e-09
Iteration	1.1281	2.4e-10

The continuous method is compared to iterations on position level. For the iterations, equidistant Newton steps were used as given in Table 6.1. The computations were performed on a processor Intel(R) Core(TM) i7-10850H CPU @ 2.70GHz. The results are very similar to those in the last chapter; here, too, the integration method is more than twice as fast, with still excellent accuracy at the end of the integration.

As in the previous chapter, again it should be noted here that the comparison with the iterations of the method at the position level is already a high-level comparison. In terms of computation time and accuracy, an even clearer superiority is to be expected compared to the discrete bead method, which has already been shown in Chapter **3** and Chapter **4** for the case without stretching, where high computational saving in the order of factors of 200–800 could be substantiated. However, due to the complex implementation of the bead chain, this comparison has been omitted at this point.

6.6   Computational results for the planar deltoid muscle

Finally, the presented method is applied to the shoulder-example mentioned at the beginning (see Fig. 1.1) of the musculus deltoideus projected onto the coronal plane. The muscle is attached to clavicula (origin) and humerus (insertion) and the prime mover for the lifting of the upper arm during abduction along the coronal plane.

To map the shape of the muscle in a rough approximation, a parabolic thick muscle is first defined as shown in Fig. 6.8 with the overall length ℓ_0, the vertex in the middle for the maximal thickness b_{max} and the thickness b_0 at the endpoints. With this, the muscle thickness related to the centerline can be generally calculated as:

$$b(s) = \frac{4}{\ell_0^2} \cdot \left(s - \frac{\ell_0}{2} \right)^2 \cdot (b_0 - b_{\mathrm{max}}) + b_{\mathrm{max}} \quad . \tag{6.52}$$

Longitudinal elongation and transverse contraction are implemented by using the model illustrated in Fig. 6.9 showing the unstretched muscle at the top with the initial length ℓ_0. Below, the muscle is stretched by $\Delta\ell$. Accordingly, the longitudinal strain is $\varepsilon = \frac{\Delta\ell}{\ell_0}$. The notation $\hat{x}$ is introduced where the hat signifies that x is a stretched variable. The variable $\hat{s}$ denotes the stretched coordinate of the centerline
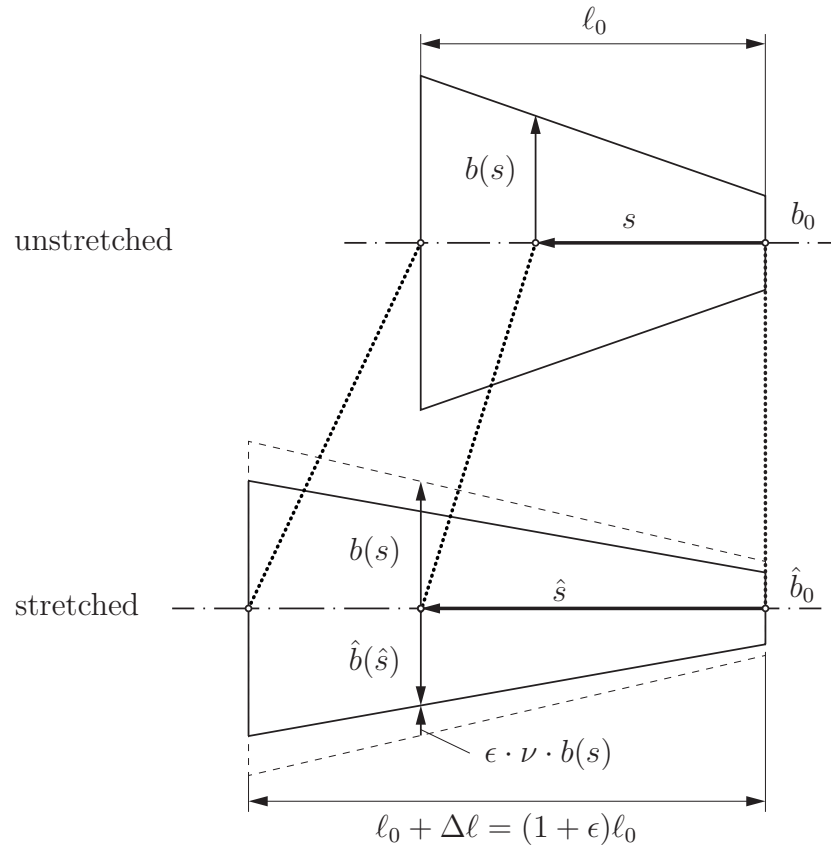
$$\hat{s} = (1 + \epsilon)\, s \quad . \tag{6.53}$$

Assuming that the muscle is made of a compressible material, the lateral contraction is assumed to fulfill the relationship

$$\frac{\Delta b}{b} = -\nu\, \frac{\Delta\ell}{\ell} = -\nu\, \varepsilon \tag{6.54}$$
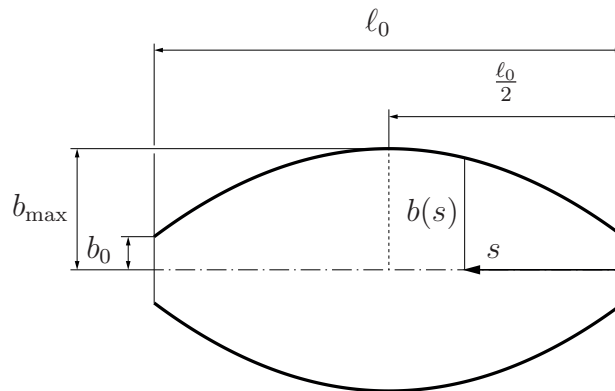
Figure 6.8: Parametrization of parabolic muscle

Figure 6.9: Stretched muscle: basic idea

where ν is the Poisson's ratio. This leads to the new profile distribution

$$\hat{b}(\hat{s}) = (1 - \nu\epsilon) \cdot b(s(\hat{s})) \quad . \tag{6.55}$$

Based on this, the necessary derivatives with respect to s and ε are straightforward to derive.

An ellipse was fitted into the shoulder joint as the wrapping surface, with its center at the origin of the coordinate system and the semiaxis lengths $a_1 = 4.2$ and $a_2 = 3.0$. The unstretched (contracted) muscle is approximately defined by the parameters $\ell_0 = 16.0$, $b_0 = 0.0$, $b_{\max} = 3.0$ and $\nu = 0.5$. Its origin O is fixed to the clavicula with the coordinates $(1.22, 3.04)$. Its insertion I is fixed to the humerus, which rotates around the shoulder joint for which the center of rotation J is assumed to lie at the coordinates $(-2.0, 0.0)$. The distance between the center of rotation J and the insertion I is approximated as 11.25.

Again, the velocity constraints formulated with respect to ε as given in Eq. (6.51) are used and implemented in Matlab using the Runge-Kutta routine ode45 for integration
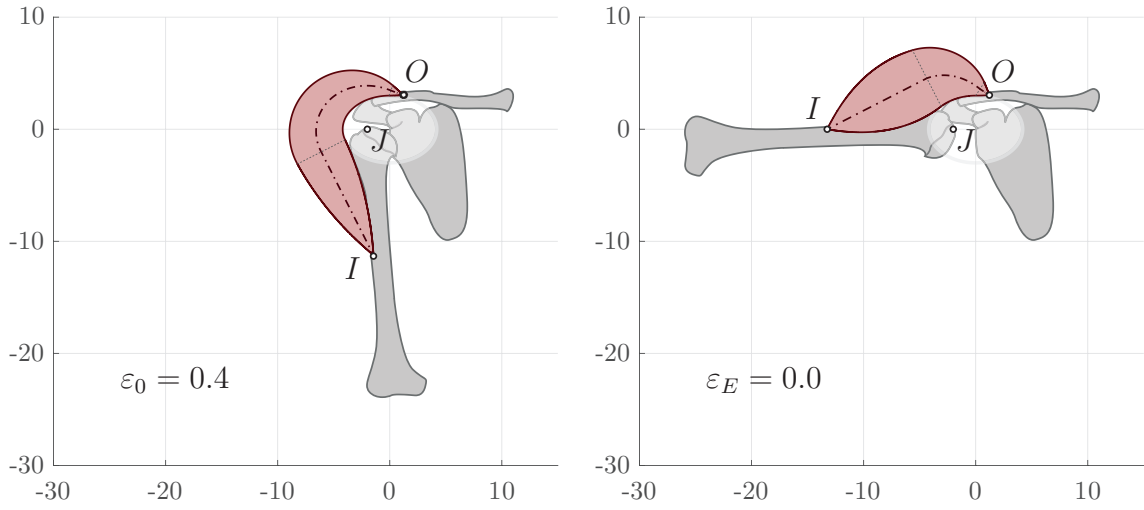
Figure 6.10: Application of the presented method for modeling the musculus deltoideus for the abduction of the upper arm with schematic visualization of the bone geometries

in the range $[0.4, 0.0]$. The computations were performed on a processor Intel(R) Core(TM) i7-10850H CPU @ 2.70GHz and the integration took an average time of $1.02s$. Fig. 6.10 shows the initial and the final pose.

7 Conclusions and Outlook

In conclusion, this contribution presents a novel, continuous and fast approach for the planar wrapping of thick muscle strands over frictionless, convex surfaces with non-constant curvature taking into account longitudinal elongation and lateral strain of the strand.

For this purpose, starting from a discretization of the thick muscle as a string of beads with a finite number of beads, a continuous description of the wrapped muscle was derived as the limit of a bead chain in contact with the surface for an infinite number of beads. After beginning with regarding only the wrapped segment, the complexity is increased step by step and the method is, thus, generalized. First is considering free muscle ends and displacement along the contact area. Second is taking into account and analyzing the influences of longitudinal strain and cross-contraction of the wrapped muscle, where one muscle end is held fixed at first. Finally, these two approaches are combined to allow free movement of the free endpoints as well as longitudinal stretching and cross-contraction of the muscle at the same time.

Summarized, the presented algorithm consists of two nested integrations: An external integration where the matching of the constraints takes place so that the length constraints and the orthogonality constraints are satisfied at both winding ends. The internal integration is required to determine the three transmissions along the wrapped segment:

(a) The length of the wrapped centerline segment,
(b) the velocity transmission along the wrapped segment due to displacement, and
(c) the influence of elongation and lateral contraction on the wrapping length.

The analytical method was verified by comparison with a discretization of the muscle as a string of beads and by iteratively solving the constraint equations at position level. For the case of a constant length of the centerline, a computation time benchmark using an implementation of the bead method resulted in computational savings by a factor of 200-800. Even taking into account that the implementation of the bead method still offers optimization potential in terms of computation time, the superiority of the analytical method clearly emerges, since it is additionally smooth, as well as significantly faster and simpler to implement once it has been derived, while still providing highly accurate results.

This lays the foundation for wrapping muscles of non-negligible thickness over friction-

less surfaces on a planar arc, as it was exemplarily demonstrated for the introductory example of the shoulder joint by applying the approach to the deltoid muscle, which is responsible for the lifting of the upper arm during abduction along the frontal plane. An ellipse was fitted into the shoulder joint as the wrapping surface. By shortening of the muscle, the upper arm is lifted and the thickening of the muscle, according to the assumption of lateral strain that the volume remains constant, is automatically taken into consideration in the calculation of the resulting muscle path.

Although the presented method was developed starting from the biomechanical problem of muscle wrapping, it can also be applied to tendons and ligaments as well as other non-biomechanical problems where strands of non-negligible thickness are wrapped over surfaces.

To give an outline for possible subsequent, future directions, the extension to spatial wrapping curves provides a first reasonable extension, since the approach is limited in this work to the planar case due to the complex differential geometric relations. The consideration of multiple or concave wrapping surfaces may also prove useful. Given that the approach presented here requires as surface information only the tangent, the normal and the radius of curvature at the contact point, one way to achieve this is to combine the thick muscle approach introduced here with the geodesic-based muscle wrapping algorithm presented in [69, 70] by taking the geodesic as the contact curve and placing the thick muscle on top.

Bibliography

[1] K. N. An, F. C. Hui, B. F. Morrey, R. L. Linscheid, and E. Y. Chao. Muscles across the elbow joint: A biomechanical analysis. *Journal of Biomechanics*, 14(10):659–669, 1981.

[2] F. C. Anderson and M. G. Pandy. Dynamic optimization of human walking. *Journal of Biomechanical Engineering*, 123(5):381–390, 2001.

[3] S. S. Antman. *Nonlinear problems of elasticity: With 105 illustrations*, volume 107 of *Applied mathematical sciences*. Springer, New York, 1995.

[4] A. Audenaert and E. Audenaert. Global optimization method for combined spherical-cylindrical wrapping in musculoskeletal upper limb modelling. *Computer Methods and Programs in Biomedicine*, 92(1):8–19, 2008.

[5] C. Bär. *Elementare Differentialgeometrie*. De Gruyter Studium. de Gruyter, Berlin u.a., 2010.

[6] R. Bellmann. *Methoden der Störungsrechnung in Mathematik, Physik und Technik*. Oldenbourg Verlag, München, 1967.

[7] S. S. Blemker and S. L. Delp. Three-dimensional representation of complex muscle architectures and geometries. *Annals of Biomedical Engineering*, 33(5):661–673, 2005.

[8] P. W. Brand, R. B. Beach, and D. E. Thompson. Relative tension and potential excursion of muscles in the forearm and hand. *The Journal of Hand Surgery*, 6(3):209–219, 1981.

[9] B. Calvo, A. Ramírez, A. Alonso, J. Grasa, F. Soteras, R. Osta, and M. J. Muñoz. Passive nonlinear elastic behaviour of skeletal muscle: Experimental results and model formulation. *Journal of Biomechanics*, 43(2):318–325, 2010.

[10] M. P. d. Carmo. *Differential geometry of curves and surfaces*. Prentice-Hall, Englewood Cliffs, N.J., 1976.

[11] I. W. Charlton and G. R. Johnson. Application of spherical and cylindrical wrapping algorithms in a musculoskeletal model of the upper limb. *Journal of Biomechanics*, 34(9):1209–1216, 2001.

[12] M. Damsgaard, J. Rasmussen, S. T. Christensen, E. Surma, and M. de Zee. Analysis of musculoskeletal systems in the AnyBody modeling system. *Simulation Modelling Practice and Theory*, 14(8):1100–1111, 2006.

[13] S. L. Delp, F. C. Anderson, A. S. Arnold, P. Loan, A. Habib, C. T. John, E. Guendelman, and D. G. Thelen. OpenSim: Open-source software to create and analyze dynamic simulations of movement. *IEEE Transactions on Biomedical Engineering*, 54(11):1940–1950, 2007.

[14] S. L. Delp and J. P. Loan. A graphics-based software system to develop and analyze models of musculoskeletal structures. *Computers in Biology and Medicine*, 25(1):21–34, 1995.

[15] S. L. Delp, J. P. Loan, M. G. Hoy, F. E. Zajac, E. L. Topp, and J. M. Rosen. An interactive graphics-based model of the lower extremity to study orthopaedic surgical procedures. *IEEE Transactions on Biomedical Engineering*, 37(8):757–767, 1990.

[16] W. Demtröder. *Experimentalphysik 1*. Springer Berlin Heidelberg, Berlin, Heidelberg, 2018.

[17] J. Dul, M. A. Townsend, R. Shiavi, and G. E. Johnson. Muscular synergism—I. On criteria for load sharing between synergistic muscles. *Journal of Biomechanics*, 17(9):663–673, 1984.

[18] P. Favre, C. Gerber, and J. G. Snedeker. Automated muscle wrapping using finite element contact detection. *Journal of Biomechanics*, 43(10):1931–1940, 2010.

[19] C. Fleischer and A. Zimmermann. Auswertung von elektromyographischen Signalen zur Steuerung von Exoskeletten. *Informatik - Forschung und Entwicklung*, 22(3):173–183, 2008.

[20] R. Franci and V. Parenti-Castelli. A new tool to investigate the interactions between elastic fibers and rigid bodies. In *IFToMM 2007: Proceedings of Twelfth World Congress in Mechanism and Machine Science*, Besançon, France, 2007.

[21] F. Gao, M. Damsgaard, J. Rasmussen, and S. T. Christensen. Computational method for muscle-path representation in musculoskeletal models. *Biological Cybernetics*, 87(3):199–210, 2002.

[22] B. A. Garner and M. G. Pandy. The obstacle-set method for representing muscle paths in musculoskeletal models. *Computer Methods in Biomechanics and Biomedical Engineering*, 3(1):1–30, 2000.

[23] H. S. Gasser and A. V. Hill. The dynamics of muscular contraction. *Proceedings of the Royal Society of London. Series B, Containing Papers of a Biological Character*, 96(678):398–437, 1924.

[24] S. A. Glantz. A constitutive equation for the passive properties of muscle. *Journal of Biomechanics*, 7(2):137–145, 1974.

[25] D. F. B. Haeufle, M. Günther, A. Bayer, and S. Schmitt. Hill-type muscle model with serial damping and eccentric force-velocity relation. *Journal of Biomechanics*, 47(6):1531–1536, 2014.

[26] H. Hatze. The meaning of the term 'biomechanics'. *Journal of Biomechanics*, 7(2):189–190, 1974.

[27] H. Hatze. A myocybernetic control model of skeletal muscle. *Biological Cybernetics*, 25(2):103–119, 1977.

[28] H. Hatze. A general myocybernetic control model of skeletal muscle. *Biological Cybernetics*, 28(3):143–157, 1978.

[29] F. Heinen, S. N. Sørensen, M. King, M. Lewis, M. E. Lund, J. Rasmussen, and M. de Zee. Muscle-tendon unit parameter estimation of a Hill-type musculoskeletal model based on experimentally obtained subject-specific torque profiles. *Journal of biomechanical engineering*, 2019.

[30] A. V. Hill. The absolute mechanical efficiency of the contraction of an isolated muscle. *The Journal of Physiology*, 46(6):435–469, 1913.

[31] A. V. Hill. The maximum work and mechanical efficiency of human muscles, and their most economical speed. *The Journal of Physiology*, 56(1-2):19–41, 1922.

[32] A. V. Hill. The heat of shortening and the dynamic constants of muscle. *Proceedings of the Royal Society of London. Series B, Biological Sciences*, 126(843):136–195, 1938.

[33] A. V. Hill. The dynamic constants of human muscle. *Proceedings of the Royal Society of London. Series B, Biological Sciences*, 128(852):263–274, 1940.

[34] A. V. Hill. The mechanics of active muscle. *Proceedings of the Royal Society of London. Series B, Biological Sciences*, 141(902):104–117, 1953.

[35] T. L. Hill. Theoretical formalism for the sliding filament model of contraction of striated muscle Part I. *Progress in Biophysics and Molecular Biology*, 28:267–340, 1974.

[36] T. L. Hill, E. Eisenberg, Y. D. Chen, and R. J. Podolsky. Some self-consistent two-state sliding filament models of muscle contraction. *Biophysical Journal*, 15(4):335–372, 1975.

[37] K. R. S. Holzbaur, W. M. Murray, G. E. Gold, and S. L. Delp. Upper limb muscle volumes in adult subjects. *Journal of Biomechanics*, 40(4):742–749, 2007.

[38] A. F. Huxley. Muscle structure and theories of contraction. *Progress in Biophysics and Biophysical Chemistry*, 7:255–318, 1957.

[39] A. F. Huxley and R. Niedergerke. Structural changes in muscle during contraction: Interference microscopy of living muscle fibres. *Nature*, 173(4412):971–973, 1954.

[40] H. Huxley and J. Hanson. Changes in the cross-striations of muscle during contraction and stretch and their structural interpretation. *Nature*, 173(4412):973–976, 1954.

[41] T. Johansson, P. Meier, and R. Blickhan. A finite-element model for the mechanical analysis of skeletal muscles. *Journal of Theoretical Biology*, 206(1):131–149, 2000.

[42] K. Jovanovic, J. Vranic, and N. Miljkovic. Hill's and Huxley's muscle models - tools for simulations in biomechanics. *Serbian Journal of Electrical Engineering*, 12(1):53–67, 2015.

[43] T. Kato. *Perturbation theory for linear operators*. Classics in mathematics. Springer, Berlin, 1995.

[44] W. Klingenberg. *Eine Vorlesung über Differentialgeometrie*, volume 107 of *Heidelberger Taschenbücher*. Springer, Berlin and Heidelberg, 1973.

[45] W. Klingenberg. *A Course in differential geometry*, volume 51 of *Graduate Texts in Mathematics*. Springer, New York, 1983.

[46] M. Kojic, S. Mijailovic, and N. Zdravkovic. Modelling of muscle behaviour by the finite element method using Hill's three-element model. *International Journal for Numerical Methods in Engineering*, 43(5):941–953, 1998.

[47] T. K. K. Koo and A. F. T. Mak. Feasibility of using EMG driven neuromusculoskeletal model for prediction of dynamic movement of the elbow. *Journal of Electromyography and Kinesiology*, 15(1):12–26, 2005.

[48] D. G. Lloyd and T. F. Besier. An EMG-driven musculoskeletal model to estimate muscle forces and knee joint moments in vivo. *Journal of Biomechanics*, 36(6):765–776, 2003.

[49] J. E. Lloyd, F. Roewer-Despres, and I. Stavness. Muscle path wrapping on arbitrary surfaces. *IEEE Transactions on Biomedical Engineering*, 68(2):628–638, 2021.

[50] K. Manal, R. V. Gonzalez, D. G. Lloyd, and T. S. Buchanan. A real-time EMG-driven virtual arm. *Computers in Biology and Medicine*, 32(1):25–36, 2002.

[51] S. P. Marsden, D. C. Swailes, and G. R. Johnson. Algorithms for exact multi-object muscle wrapping and application to the deltoid muscle wrapping around the humerus. *Proceedings of the Institution of Mechanical Engineers, Part H: Journal of Engineering in Medicine*, 222(7):1081–1095, 2008.

[52] J. A. C. Martins, M. P. M. Pato, and E. B. Pires. A finite element model of skeletal muscles. *Virtual and Physical Prototyping*, 1(3):159–170, 2006.

[53] D. Meschede. *Gerthsen Physik*. Springer Berlin Heidelberg, Berlin, Heidelberg, 2010.

[54] A. Murai, K. Takeichi, T. Miyatake, and Y. Nakamura. Musculoskeletal modeling and physiological validation. *2014 IEEE International Workshop on Advanced Robotics and its Social Impacts*, pages 108–113, 2014.

[55] A. Murai, Q. Youn Hong, K. Yamane, and J. K. Hodgins. Dynamic skin deformation simulation using musculoskeletal model and soft tissue dynamics. *Computational Visual Media*, 3(1):49–60, 2017.

[56] W. M. Murray, A. S. Arnold, S. Salinas, M. M. Durbhakula, T. S. Buchanan, and S. L. Delp. Building biomechanical models based on medical image data:

An assessment of model accuracy. In *Medical Image Computing and Computer-Assisted Intervention - MICCAI'98*, volume 1496 of *Lecture Notes in Computer Science*. Springer, Berlin and Heidelberg, 1998.

[57] W. M. Murray, S. L. Delp, and T. S. Buchanan. Variation of muscle moment arms with elbow and forearm position. *Journal of Biomechanics*, 28(5):513–525, 1995.

[58] A. A. Nikooyan, H. E. J. Veeger, P. Westerhoff, B. Bolsterlee, F. Graichen, G. Bergmann, and F. C. T. van der Helm. An EMG-driven musculoskeletal model of the shoulder. *Human Movement Science*, 31(2):429–447, 2012.

[59] M. A. Nussbaum, D. B. Chaffin, and C. J. Rechtien. Muscle lines-of-action affect predicted forces in optimization-based spine muscle modeling. *Journal of Biomechanics*, 28(4):401–409, 1995.

[60] D. K. Pai. STRANDS: Interactive simulation of thin solids using cosserat models. *Computer Graphics Forum*, 21(3):347–352, 2002.

[61] D. K. Pai, S. Sueda, and Q. Wei. Simulation of 3D neuro-musculo-skeletal systems with contact. In *Advances in Computational Motor Control III. Symposium at the Society for Neuroscience Meeting*, 2004.

[62] D. K. Pai, S. Sueda, and Q. Wei. Fast physically based musculoskeletal simulation. In *ACM SIGGRAPH 2005 Sketches*, New York, New York, USA, 2005.

[63] A. N. Pressley. *Elementary Differential Geometry*. Springer Undergraduate Mathematics Series. Springer-Verlag London, London, 2010.

[64] R. T. Raikova and B. I. Prilutsky. Sensitivity of predicted muscle forces to parameters of the optimization-based human leg model revealed by analytical and numerical analyses. *Journal of Biomechanics*, 34(10):1243–1255, 2001.

[65] H. A. Richard, G. Kullmer, and D. Nöcker. *Biomechanik: Grundlagen und Anwendungen auf den menschlichen Bewegungsapparat; mit 15 Tabellen*. Springer Vieweg, Wiesbaden, 2013.

[66] O. Röhrle, J. B. Davidson, and A. J. Pullan. Bridging scales: A three-dimensional electromechanical finite element model of skeletal muscle. *SIAM Journal on Scientific Computing*, 30(6):2882–2904, 2008.

[67] M. B. Rubin. *Cosserat theories: Shells, rods and points*, volume 79 of *Solid mechanics and its applications*. Kluwer Academic Publ, Dordrecht, 2000.

[68] F. Scheepers, R. E. Parent, W. E. Carlson, and S. F. May. Anatomy-based modeling of the human musculature. In *Proceedings of the 24th annual conference on Computer graphics and interactive techniques - SIGGRAPH '97*, New York, New York, USA, 1997.

[69] A. Scholz. *Fast Differential-Geometric Methods for Continuous Muscle Wrapping Over Multiple General Surfaces*. Dissertation, Universität Duisburg-Essen, Duisburg, 2016.

[70] A. Scholz, M. Sherman, I. Stavness, S. Delp, and A. Kecskeméthy. A fast multi-obstacle muscle wrapping method using natural geodesic variations. *Multibody System Dynamics*, 36(2):195–219, 2016.

[71] M. Schünke, E. Schulte, U. Schumacher, M. Voll, and K. Wesker. *Prometheus - LernAtlas der Anatomie. Allgemeine Anatomie und Bewegungssystem: 182 Tabellen*. Thieme, Stuttgart, 2011.

[72] C. Y. Scovil and J. L. Ronsky. Sensitivity of a Hill-based muscle model to perturbations in model parameters. *Journal of Biomechanics*, 39(11):2055–2063, 2006.

[73] K. B. Shelburne and M. G. Pandy. A musculoskeletal model of the knee for evaluating ligament forces during isometric contractions. *Journal of Biomechanics*, 30(2):163–176, 1997.

[74] K. B. Shelburne, M. G. Pandy, and M. R. Torry. Comparison of shear forces and ligament loading in the healthy and ACL-deficient knee during gait. *Journal of Biomechanics*, 37(3):313–319, 2004.

[75] K. B. Shelburne, M. R. Torry, and M. G. Pandy. Muscle, ligament, and joint-contact forces at the knee during walking. *Medicine & Science in Sports & Exercise*, 37(11):1948–1956, 2005.

[76] L. A. Spyrou and N. Aravas. Muscle-driven finite element simulation of human foot movements. *Computer Methods in Biomechanics and Biomedical Engineering*, 15(9):925–934, 2012.

[77] K. Strubecker. *Differentialgeometrie. 1. Kurventheorie der Ebene und des Raumes*. 1113/1113a. de Gruyter, Berlin, 1964.

[78] K. Strubecker. *Differentialgeometrie. 2. Theorie der Flächenmetrik*. 1179/1179a. de Gruyter, Berlin, 1969.

[79] D. J. Struik. *Lectures on classical differential geometry*. Addison-Wesley Series in Mathematics. Addison-Wesley, London, 1961.

[80] S. Sueda, A. Kaufman, and D. K. Pai. Musculotendon simulation for hand animation. *ACM Transactions on Graphics*, 27(3):1, 2008.

[81] S. Sueda and D. K. Pai. Hand simulation models in computer graphics. *Journal of the Society of Biomechanisms*, 38(1):19–24, 2014.

[82] J. Teran, S. Blemker, V. N. T. Hing, and R. Fedkiw. Finite volume methods for the simulation of skeletal muscle. In *Proceedings of the 2003 ACM SIG-GRAPH/Eurographics Symposium on Computer Animation*, SCA '03, Aire-la-Ville, Switzerland, 2003.

[83] D. G. Thelen, K. Won Choi, and A. M. Schmitz. Co-simulation of neuromuscular dynamics and knee mechanics during human walking. *Journal of Biomechanical Engineering*, 136(2):21033, 2014.

[84] Y. H. Tsuang, G. J. Novak, O. D. Schipplein, A. Hafezi, J. H. Trafimow, and G. B. Andersson. Trunk muscle geometry and centroid location when twisting. *Journal of Biomechanics*, 26(4-5):537–546, 1993.

[85] F. van der Helm. A finite element musculoskeletal model of the shoulder mechanism. *Journal of Biomechanics*, 27(5):551–569, 1994.

[86] A. N. Vardy, E. de Vlugt, and F. C. T. van der Helm. Parameter estimation of the Huxley cross-bridge muscle model in humans. *2012 Annual International Conference of the IEEE Engineering in Medicine and Biology Society*, pages 4827–4830, 2012.

[87] J. Wilhelms and A. van Gelder. Anatomically based modeling. In *Proceedings of the 24th annual conference on Computer graphics and interactive techniques - SIGGRAPH '97*, New York, New York, USA, 1997.

[88] J. M. Winters and L. Stark. Muscle models: What is gained and what is lost by varying model complexity. *Biological Cybernetics*, 55(6):403–420, 1987.

[89] J. E. Wood and R. W. Mann. A sliding-filament cross-bridge ensemble model of muscle contraction for mechanical transients. *Mathematical Biosciences*, 57(3-4):211–263, 1981.

[90] G. I. Zahalak. A distribution-moment approximation for kinetic theories of muscular contraction. *Mathematical Biosciences*, 55(1-2):89–114, 1981.

[91] F. E. Zajac. Muscle and tendon: Properties, models, scaling, and application to biomechanics and motor control. *Critical Reviews in Biomedical Engineering*, 17(4):359–411, 1989.

[92] O. Zarifi and I. Stavness. Muscle wrapping on arbitrary meshes with the heat method. *Computer Methods in Biomechanics and Biomedical Engineering*, 20(2):119–129, 2017.

A Scalar products of unit vectors
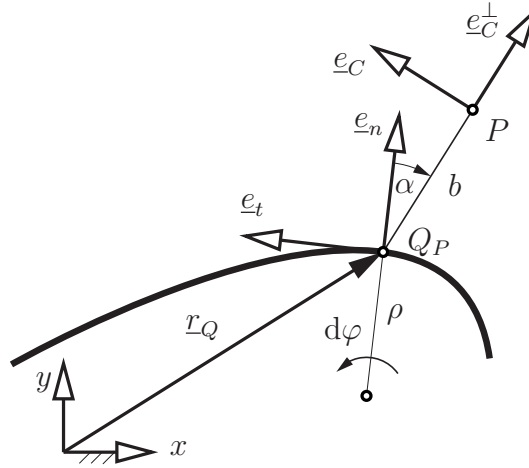
Figure A.1: Illustration for scalar products of unit vectors

The scalar products of the surface curve unit vectors, i.e., the surface tangent $\underline{e}_t$ and the surface normal $\underline{e}_n$, with the muscle's unit vectors ($\underline{e}_C$ normal to the muscle's cross-section and $\underline{e}_C^\perp$ tangential to it), as given in Fig. A.1, yield

$$\underline{e}_t \cdot \underline{e}_C = \quad \cos\alpha \quad , \tag{A.1}$$

$$\underline{e}_t \cdot \underline{e}_C^\perp = -\sin\alpha \quad , \tag{A.2}$$

$$\underline{e}_n \cdot \underline{e}_C = \quad \sin\alpha \quad \text{and} \tag{A.3}$$

$$\underline{e}_n \cdot \underline{e}_C^\perp = \quad \cos\alpha \tag{A.4}$$

with α being the actual conicity of the muscle (which may vary over the muscle's length).

B Proof of the Taylor series approximation in Section 3.3.2

By concatenating the pairwise velocity transmission for all $N-1$ beads $i = 2, \ldots, N$ after given bead "1" it follows

$$\frac{\dot{u}_N}{\dot{u}_1} = [1 + \eta_1\, \Delta\rho_1]\, [1 + \eta_2\, \Delta\rho_2] \ldots [1 + \eta_{N-1}\, \Delta\rho_{N-1}] \tag{B.1}$$

for the velocity transmission between the first and the last beat with

$$\eta_i = \frac{r_i}{\rho_i\, (\rho_i + r_i)} \quad . \tag{B.2}$$

Multiplicated, the summands can be grouped together by the following summations

$$\frac{\dot{u}_N}{\dot{u}_1} = \underbrace{1}_{= T_0} + \underbrace{\sum_{i=1}^{N-1} \eta_i\, \Delta\rho_i}_{= T_1} + \underbrace{\sum_{i_1=1}^{N-1} \sum_{i_2=i_1+1}^{N-1} \eta_{i_1}\eta_{i_2}\, \Delta\rho_{i_1}\Delta\rho_{i_2}}_{= T_2}$$

$$+ \underbrace{\sum_{i_1=1}^{N-1} \sum_{i_2=i_1+1}^{N-1} \sum_{i_3=i_2+1}^{N-1} \eta_{i_1}\eta_{i_2}\eta_{i_3}\, \Delta\rho_{i_1}\Delta\rho_{i_2}\Delta\rho_{i_3}}_{= T_3}$$

$$+ \ldots \quad . \tag{B.3}$$

For small $\Delta\rho_i$ the velocity transmission can be approximated by the Taylor series for the exponential function $\exp\left(\sum_{i=1}^{N-1} \eta_i\, \Delta\rho_i\right)$ centered at zero. The first two summands T_0 and T_1 can also be expressed by

$$T_0 = \left[\sum_{i=1}^{N-1} \eta_i\, \Delta\rho_i\right]^0 \tag{B.4}$$

$$T_1 = \left[\sum_{i=1}^{N-1} \eta_i\, \Delta\rho_i\right]^1 \quad . \tag{B.5}$$

The third sum T_2 can be approximated by

$$T_0 + T_1 + T_2 \approx T_0 + T_1 + \frac{1}{2}\left[\sum_{i=1}^{N-1} \eta_i\, \Delta\rho_i\right]^2 \quad , \tag{B.6}$$

because it holds

$$\frac{1}{2}\left[\sum_{i=1}^{N-1}\eta_i\,\Delta\rho_i\right]^2 = \underbrace{\frac{1}{2}\sum_{i_1=1}^{N-1}\sum_{\substack{i_2=1\\i_2\neq i_1}}^{N-1}\eta_{i_1}\eta_{i_2}\,\Delta\rho_{i_1}\Delta\rho_{i_2}}_{=\,T_2} + \underbrace{\frac{1}{2}\sum_{i=1}^{N-1}\eta_i^2\,\Delta\rho_i^2}_{\ll\,T_1} \tag{B.7}$$

where the second term can be neglected due to being of higher order and, thereby, negligibly smaller than T_1.

Analogous to this, the fourth sum T_3 can be approximated as follows

$$T_0 + T_1 + T_2 + T_3 \approx T_0 + T_1 + T_2 + \frac{1}{3!}\left[\sum_{i=1}^{N-1}\eta_i\,\Delta\rho_i\right]^3 \tag{B.8}$$

because it analogously applies

$$\frac{1}{3!}\left[\sum_{i=1}^{N-1}\eta_i\,\Delta\rho_i\right]^3 = \underbrace{\frac{1}{3!}\sum_{i_1=1}^{N-1}\sum_{\substack{i_2=1\\i_2\neq i_1}}^{N-1}\sum_{\substack{i_3=1\\i_3\neq i_1\\i_3\neq i_2}}^{N-1}\eta_{i_1}\eta_{i_2}\eta_{i_3}\,\Delta\rho_{i_1}\Delta\rho_{i_2}\Delta\rho_{i_3}}_{=\,T_3}$$

$$+ \underbrace{\frac{1}{3!}\cdot 3\sum_{i_1=1}^{N-1}\sum_{\substack{i_2=1\\i_2\neq i_1}}^{N-1}\eta_{i_1}^2\eta_{i_2}\,\Delta\rho_{i_1}^2\Delta\rho_{i_2}}_{\ll\,T_2} + \underbrace{\frac{1}{3!}\sum_{i=1}^{N-1}\eta_i^3\,\Delta\rho_i^3}_{\ll\,T_1} \tag{B.9}$$

where the last two terms are again negligibly smaller than T_2 and T_1, respectively, and can therefore be neglected.

So for any specific number k the following statement can be formulated

$$\frac{1}{k!}\left[\sum_{i=1}^{N-1}\eta_i\,\Delta\rho_i\right]^k=\underbrace{\frac{1}{k!}\sum_{i_1=1}^{N-1}\sum_{\substack{i_2=1\\i_2\neq i_1}}^{N-1}\cdots\sum_{\substack{i_k=1\\i_k\neq i_1\\i_k\neq i_2\\\vdots\\i_k\neq i_{k-1}}}^{N-1}\eta_{i_1}\eta_{i_2}\ldots\eta_{i_k}\,\Delta\rho_{i_1}\Delta\rho_{i_2}\ldots\Delta\rho_{i_k}}_{=\,T_k}$$

$$+\underbrace{\frac{1}{k!}\sum_{i=1}^{N-1}\eta_i^k\,\Delta\rho_i^k}_{\ll\,T_1}$$

$$+\underbrace{\frac{k}{k!}\cdot 3\sum_{i_1=1}^{N-1}\sum_{\substack{i_2=1\\i_2\neq i_1}}^{N-1}\eta_{i_1}^{k-1}\eta_{i_2}\,\Delta\rho_{i_1}^{k-1}\Delta\rho_{i_2}}_{\ll\,T_2}$$

$$+\ldots\tag{B.10}$$

with all other terms (except for the first one that equals T_K) being negligibly smaller than the previous sums T_i with $i=1,\ldots,k-1$ which leads to

$$T_k\approx\frac{1}{k!}\left[\sum_{i=1}^{N-1}\eta_i\,\Delta\rho_i\right]^k\,.\tag{B.11}$$

By mathematical induction, it can be proven that this statement holds for all $k\in\mathbb{N}$. Having shown that this statement is true for the first four sums and assuming that it

is true for k, it has to be shown that it is true for its successor $k + 1$:

$$\frac{1}{(k+1)!} \left[\sum_{i=1}^{N-1} \eta_i \, \Delta\rho_i \right]^{k+1}$$

$$= \underbrace{\frac{1}{k!} \left[\sum_{i=1}^{N-1} \eta_i \, \Delta\rho_i \right]^{k}}_{\approx T_k} \cdot \frac{1}{k+1} \left[\sum_{i=1}^{N-1} \eta_i \, \Delta\rho_i \right]$$

$$\approx \frac{1}{k+1} \underbrace{\left[\sum_{i_1=1}^{N-1} \sum_{i_2=i_1+1}^{N-1} \cdots \sum_{i_k=i_{k-1}+1}^{N-1} \eta_{i_1}\eta_{i_2}\ldots\eta_{i_k} \, \Delta\rho_{i_1}\Delta\rho_{i_2}\ldots\Delta\rho_{i_k} \right]}_{= T_k} \left[\sum_{i=1}^{N-1} \eta_i \, \Delta\rho_i \right]$$

$$= \underbrace{\sum_{i_1=1}^{N-1} \sum_{i_2=i_1+1}^{N-1} \cdots \sum_{i_{k+1}=i_k+1}^{N-1} \eta_{i_1}\eta_{i_2}\ldots\eta_{i_{k+1}} \, \Delta\rho_{i_1}\Delta\rho_{i_2}\ldots\Delta\rho_{i_{k+1}}}_{= T_{k+1}}$$

$$+ \underbrace{\frac{1}{(k+1)!} \sum_{i_1=1}^{N-1} \sum_{\substack{i_2=1 \\ i_2 \neq i_1}}^{N-1} \cdots \sum_{\substack{i_k=1 \\ i_k \neq i_1 \\ i_k \neq i_2 \\ \vdots \\ i_k \neq i_{k-1}}}^{N-1} \eta_{i_1}^2\eta_{i_2}\ldots\eta_{i_k} \, \Delta\rho_{i_1}^2\Delta\rho_{i_2}\ldots\Delta\rho_{i_k}}_{\ll T_k} \qquad (\text{B.12})$$

$$\square$$

DuEPublico

Duisburg-Essen Publications online